# Curling dynamics of naturally curved surfaces : axisymmetric bio-membranes and elastic ribbons

Octavio Eduardo Albarrán Arriagada

## To cite this version:

Octavio Eduardo Albarrán Arriagada. Curling dynamics of naturally curved surfaces : axisymmetric bio-membranes and elastic ribbons. Other [cond-mat.other]. Université Montpellier II - Sciences et Techniques du Languedoc, 2013. English. NNT : 2013MON20055 . tel-00997537

**HAL Id: tel-00997537**

**https://theses.hal.science/tel-00997537v1**

Submitted on 28 May 2014

Collège Doctoral
du Languedoc-Roussillon

# THÈSE
Pour obtenir le grade de
Docteur

Délivré par l'**Université Montpellier II**

Préparée au sein de l'école doctorale **I2S***
Et de l'unité de recherche **UMR 5221**
- Laboratoire **Charles Coulomb**

Spécialité: **Physique**

Présentée par **Octavio Eduardo Albarran Arriagada**

# Curling dynamics of naturally curved surfaces: axisymmetric bio-membranes and elastic ribbons

Soutenance prévue le 20/12/2013 devant le jury composé de :

| | | | |
|---|---|---|---|
| M. Vladimir LORMAN | Professeur | Univ. Montpellier II | Examinateur† |
| M. Pierre NASSOY | DR | Univ. Bordeaux I | Rapporteur |
| M. Benoît ROMAN | CR | ESPCI | Rapporteur |
| M. Emmanuel VILLERMAUX | Professeur | Univ. Aix Marseille | Examinateur |
| Mme. Gladys MASSIERA | MdC | Univ. Montpellier II | Co-Directrice |
| M. Manouk ABKARIAN | CR | Univ. Montpellier II | Directeur |

UNIVERSITÉ MONTPELLIER 2
SCIENCES ET TECHNIQUES

*[Il suivait son idée, c'était une idée fixe.*
*Et il était surpris de ne pas avancer !]*

* **I2S:** ECOLE DOCTORALE INFORMATION STRUCTURES SYSTÈMES; † PRESIDENT DU JURY

# Contents

# Chapter 1

# Curling in nature and technology

This work is dedicated to the curling dynamics of surfaces having a spontaneous curvature. It was initially inspired by the axisymmetric curling of a biomembrane on a spherical geometry observed at a microscopic scale on two different systems that will be described further: Malaria infected red blood cell membrane and assymmetric polymersomes membrane. Curling is a way to store elastic energy and is used in nature and in engineering for numerous purpose. This phenomenon occurs for thin objects, for which bending deformations are low cost and when their spontaneous radius of curvature is finite and smaller than their characteristic dimensions. In the process of curling, several dissipation mechanisms are at play and will define the various regime of curling. In this first chapter, we wish to describe in which conditions and for what systems curling occurs and what theoretical approaches have been proposed so far to understand curling dynamics of some specific systems.

## 1.1 From bending to curling of thin objects

When one dimension of a continuous solid body is small compared with the other geometrical scales, the free energy cost is small for some specific large deformation: bending. For instance, a metal cylinder with diameter $a$ and height $b$ can resist quite well an axial compression. However, under the same compressive stress (that is, the same force per cross-section surface area), when the aspect ratio $a/b$ is low, a sudden little failure of a structural member can induce a dramatic flexion. Indeed, the critical buckling stress for a cylindrical column, well known in mechanical engineering, writes $\sigma_c \backsim (a/b)^2$ and is much smaller than the critical stress of rupture. Of course, when $a/b \lll 1$, the cylinder becomes a filament and it loses virtually all resistance to axial compression. In the field of mechanics, these kind materials are described by the elasticity theories of thin plates and rods.

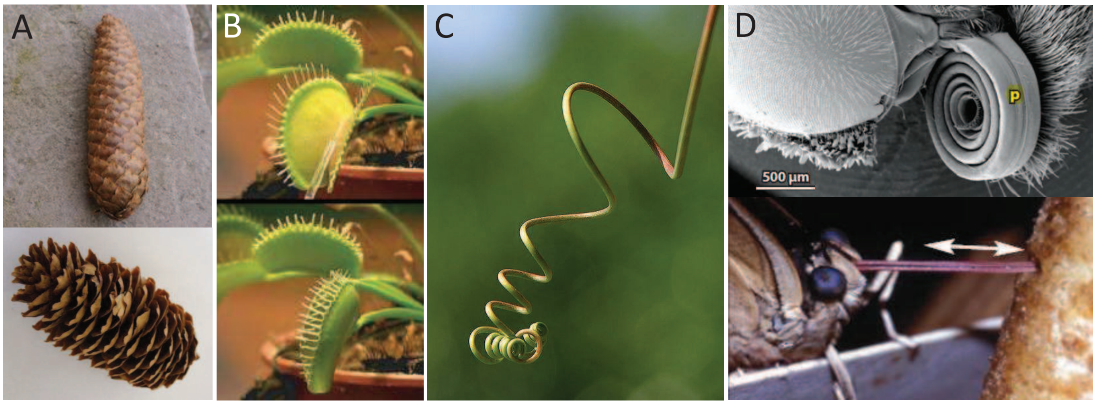

Figure 1.1: A.- Pine cones, closed and open, depending of the humidity in the environment. B.- The Venus flytrap (*Dionaea muscipula*) in its open and closed states (images from [25]). C.- Helical coiling of plant tendrils. D.- Proboscis (p) coiled in the resting position and a fruit-piercing butterfly, *Archaeoprepona demophoon*, pushes its proboscis tip into fruit (images from [37]).

In general, thin objects, because of their low resistance to specific deformation, can be understood as soft systems. Whatever the molecular organization, their tendency to be bent easily, allow large displacements at low energetic cost. This specific property has been exploited by nature in many ways as illustrated in Fig.1.1 and in some cases have been investigated from a mechanical point of view. For instance, the reversible closure and opening of mature pine cones [62], the rapid closure of the Venus flytrap based on a snap-buckling instability [25], the helical coiling of plant tendrils that work as springs with tunable mechanical responses [26] and the contracting butterfly proboscis governed by curvature elasticity [37] and analog to the recoiling of the paper tube in a party horn. In this last example, the natural state of the proboscis (or the paper in the case of the party horn) corresponds to a coil of defined curvature, and the uncoiling state is reached thanks to hydraulic forces. When these interactions are suddenly turned off, the system tries to come back to the resting curled state. Therefore, a curvature wave propagates down along the material, allowing a systematic bending of the material on itself, the so-called curling. Curling occurs to release the elastic energy stored in a system which bends on itself towards a natural radius smaller or much smaller than the material length.

Numerous structures and geometries exhibit curling once they acquire a natural curvature. Examples span disciplines (see Fig.1.2) and scales from the catastrophic disassembly of microtubules [51] and the rolling up of nanotubes [71] to the observed rolling of tracing paper placed on a water surface [63] (partially wet paper curls!). Since the materials are essentially soft, the curling dynamics depends strongly on the dissipation mechanisms.

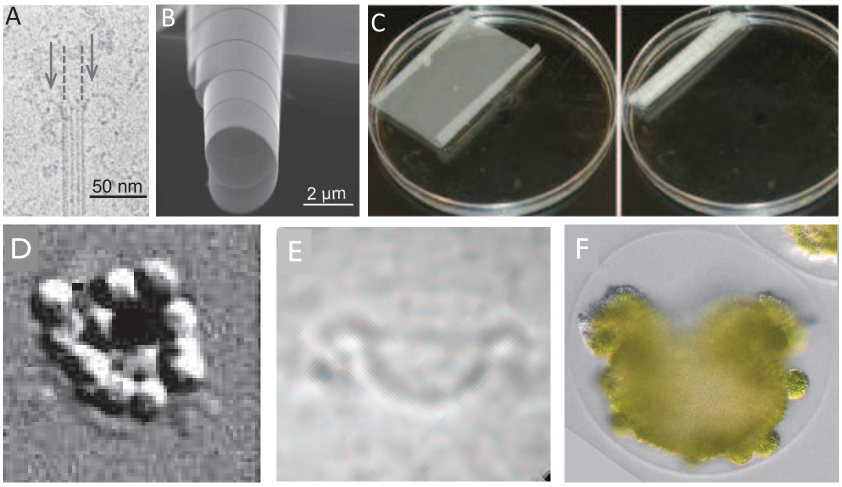

Figure 1.2: Curling observed on: A.- microtubule during shrinkage (Cryo-electron microscopy of unstained, frozen-hydrated from [51]); B.- SEM image of a rolled-up Si tube (image from [71]); C.- Tracing paper (45 $\mu$m thick) on a water bath (from [63]); D.- Malaria infected red blood cells [1]; and E.- Artificial polymersomes [48]. F.- Volvox algae colonies [81].

Indeed, viscous dissipations associated with the relative movement of the fluid environment become more and more important when smaller-scale objects are considered and can lead to situations where the characteristic lengths of the bending wave front differ considerably from those natural radii.

## 1.2 Microscopic systems that motivated our work

The theoretical description of curling dynamics is especially relevant for micro or nanoscale systems for which the elastic characteristics and specifically the value of the natural radii, can not be measured. In such a case, the observables of the curling dynamics are good candidates to indirectly measure mechanical properties of the material.

In the work of Mabrouk and collaborators [49] (see Fig.1.2D), the axisymmetric curling of polymersomes membranes allow to achieve a rapid exchange of the internal content of polymersomes with the outside solvent. In this system of asymmetric polymer vesicles, one of the two leaflets is composed of UV-responsive polymers so that, under remote UV illumination, an important difference of surface area between the two leaflets is induced. Therefore, because the natural curvature and density of the leaflets are geometrically coupled, once a pore is open, the membrane will bend continuously on itself in order to reach its new resting elastic configuration.

Another example with spherical geometry and similar difficulties in the interpretation of the bending modes, is the curling of lipidic membrane observed during the egress of malarial parasites from red blood cells [1]. The culminating step of the intraerythrocytic development of Plasmodium falciparum, the causative agent of malaria, is the spectacular release of multiple invasive merozoites on rupture of the infected erythrocyte membrane. It has been observed [1] that this release occurs in 3 main steps after osmotic swelling of the infected erythrocyte: a pore opens in around 100 milliseconds, ejecting 1-2 merozoites, an outward curling of the erythrocyte membrane, ending with a fast eversion of the infected erythrocyte membrane, pushing the parasites forward (see Fig.1.2E). In this case, although it may be realized that during the parasite development the infected erythrocyte membrane acquires a spontaneous curvature, the origin of the curling is poorly understood.

In both systems, the geometry is axisymmetric and the only observable are the aperture dynamics parameters (the pore radius). In both studies, a minimal model is proposed to extract the spontaneous curvature of the nanoscaled membrane and the dissipation. Both interpretation are in need of a more refine description of the curling dynamics and more exhaustive account of the various dissipation mechanisms that can be involved at this scale.

## 1.3 Macroscopic approaches to curling: the paradigm of the wet tracing paper

In the preceding examples, a direct measurement of the induced difference of area or natural curvature (spontaneous curvature) is extremely difficult. In addition, the low resolution on the membrane during the curling process precludes an adequate experimental characterization of the bending modes. Several physical models have been proposed to describe curling at the macro-scale. Among them, the curling of tracing paper [63] consists in placing the tracing paper at a water surface. The natural curvature is induced by the partial wetting of the paper: the face in contact with water is swelled creating a difference in area with the face in contact with air. A curling consequently occurs. Later, when the whole paper sink and both faces are swollen, the natural curvature goes down to zero and unwinding is observed. This simple system is of particular interest to study hygroscopic deformation of plants. Nevertheless, the coupling between water permeation and mechanical properties is difficult to describe, as well as the specific mode of dissipation in the contact line.

## 1.4 Theoretical approaches with the Elastica paradigm

Two recent works have been developed on curling for elastic lines (Elastica approach). Firstly Kabaso et al. [39], propose a molecular model of curling in RBCs were the average spontaneous curvature of the membrane is induced by the diffusion field of anchored polymers (representing the detached cytoskeleton elements in RBCs) coupled to the curvature of a straight stripe representing the membrane. The dynamics take into consideration viscous drag around the strip. The membrane profiles are obtained as a function of time using a thin strip of membrane that is curved only along its length. They indeed report a curling deformation of the stripe (Figure 1.3A), but the characteristic time associated with the resultant motion is much larger than the one observed in the axisymmetric curling of polymersomes and during the egress of malarial parasites.

On the other hand, a recent numerical work based on the Kirchhoff equations describes the dynamics of a naturally curved Elastica without gravity or friction [9]. The authors report finds a self-similar growing spiral regime of propagation which reaches a constant curling velocity at an infinite time (Figure 1.3B) but whose experimental evidence is lacking.

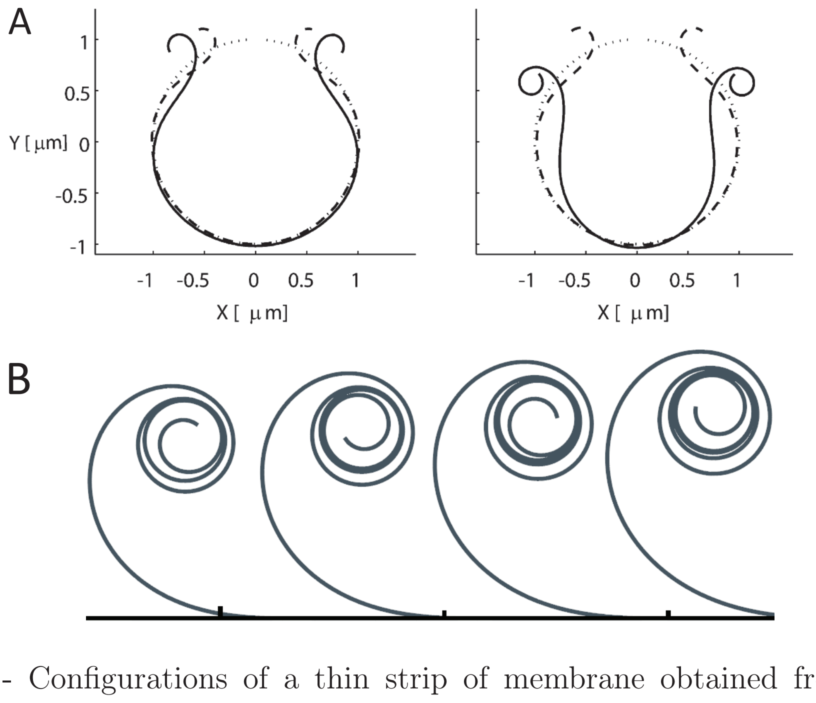

Figure 1.3: A.- Configurations of a thin strip of membrane obtained from numerical calculations (from [39]) B.- Direct numerical solutions for the shape of the self-similar curling of a naturally curved elastica (from [9]).

## 1.5 Motivations

As already mentioned, curling deformation is based on the ability of the system to store energy in the creation (or destruction) of curvature. From this point of view, the driven potential energy of the process can be expressed with linear expansions of the accessible bending modes (the relevant “degrees of freedom") which depend strongly on the physical nature of the material. For example, fluid membranes can be bent while allowing, at the same time, a redistribution of matter, while internal stresses in a solid shell are controlled by strong resistances to intrinsic modifications in the arrangement of molecules (Fig. 1.4).

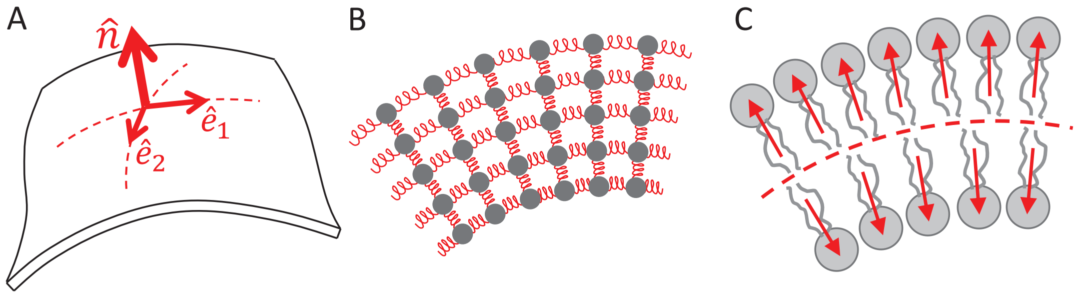

Figure 1.4: Sketches for bending models. A.- Representation of the principal local axes in a thin material. B.- Standard solid material represented by a configuration of springs. C.- Fluid membrane modeled as a nematic liquid crystal where the director of the individual molecules coincides with the normal unitary vector $\hat{n}$ of the surface.

In this work, I have analyzed theoretically the limits of the phenomenological models of axisymmetric curling of fluid membranes motivated by the recent microscopic observations of curling in membranes of Malaria infected red blood cells (MIRBC) and artificial polymersomes. Subsequently, due to the lack of clear experimental images of microscopic curling, and the complexity of the spherical topology, I studied in a second part, both theoretically and experimentally, the curling of macroscopic naturally curved elastic ribbons. In order to separate the respective roles of flow, elasticity and geometry, the experiments are performed in different viscous media and elastic conditions to obtain crucial information of the inherent elasto-viscous coupling during curling.

# Chapter 2

# Curling of axisymmetric membranes: polymersomes and malaria-infected red blood cells membranes

---

## 2.1 Curling in artificial and bio- membranes

### 2.1.1 Curling in polymersomes: artificially induced spontaneous curvature

Polymersomes are tough vesicles compared to their lipid analog because of their high lysis tension three to four times higher [21, 18]. This resistance to tension comes from their composition made of diblock copolymer amphiphiles and make them good candidates as drug carriers. However, while previous approaches to design responsive polymersomes whose degradation upon environmental changes has been used for slow release of active species, Mabrouk et al. [48] designed new types of sensitive polymersomes capable of fast release of their internal medium.

The strategy used by the authors has been able to build asymmetric polymersomes where one leaflet can immediately change its surface area compared to the other under UV-illumination, due to the presence of modified liquid crystalline diblock copolymers (Fig. 2.1A,B). The conformational change of the copolymers in one leaflet changes its surface area and induces a strong local spontaneous curvature in the membrane that can lead to poration [48]. Mabrouk et al. found that bursting of their structure happens with a subsequent catastrophic curling in a fraction of a second (see Fig. 2.1C).

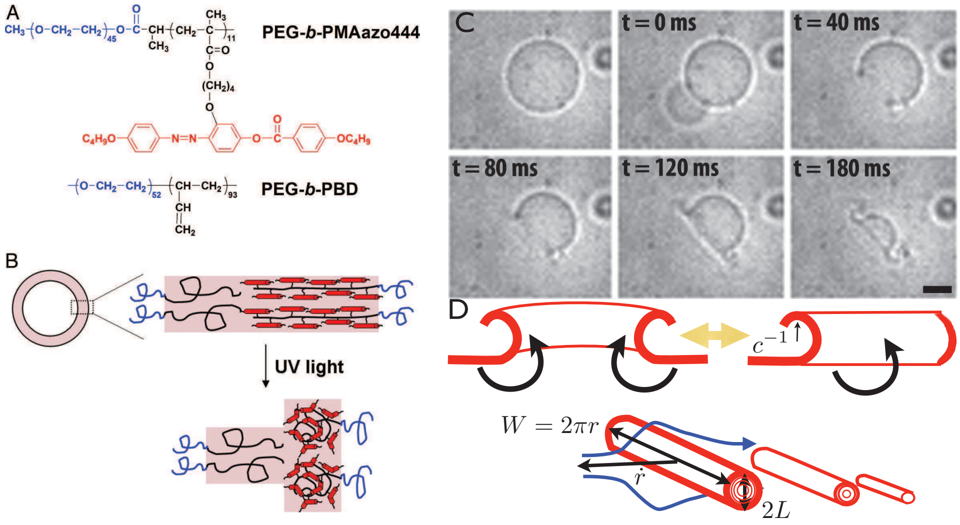

Figure 2.1: (A) Chemical structures of the 2 selected copolymers, PEG-b-PBD and PEG-b-PMAzo444. (B) Cartoon of a polymersome and cartoon depicting the conformation of both copolymers within the bilayer for an ePAzo-iPBD vesicle (from [48]). C. Snapshots of an ePBD-iPAzo polymersome bursting under UV illumination. Scale bar= 5 $\mu$m. D. Cartoon of the assumptions made in the model developed by Mabrouk at al. [48]

### 2.1.2 Curling in Malaria-infected Red Blood Cells

Malaria is an infectious human disease responsible for a million deaths each year. Its clinical symptoms occur at the blood stage of a cellular parasite, called a merozoite in this stage, looking like a tiny and complex ovoid about a micrometer across. In this invasive form one merozoite actively penetrates a red blood cell (RBC), where it multiplies during 48 hours. The culminating step of the development is then the spectacular release of the newly formed merozoites in a split second, ready to infect new RBCs passing by in the microcirculation (Figure 2.2).

Thirty five years after the seminal video microscopy work of Dvorak et al. [22], this fast process remained only described phenomenologically as an “explosive” event [29, 28, 27]. However, what happened to the membrane during this “explosion” and, in particular, how parasite displacements could reach several times their body size in such short time, without any swimming appendices or inertia were questions that had not yet received convincing answers because of the lack of direct fast observations. Hypothetical mechanisms have been proposed but not proven, such as the shredding of the membrane because of the osmotic pressure or a breaching of the infected red blood cell (iRBC) membrane by the parasite [28]. Using high-speed video-microscopy, recent studies have shown that the release is indeed the result of an elastic instability of the iRBC membrane [1].

After osmotic swelling over several minutes, the release occurs in 3 main steps [1]. First, a pore opens in around 100 milliseconds, ejecting 1-2 merozoites. Second, the edge

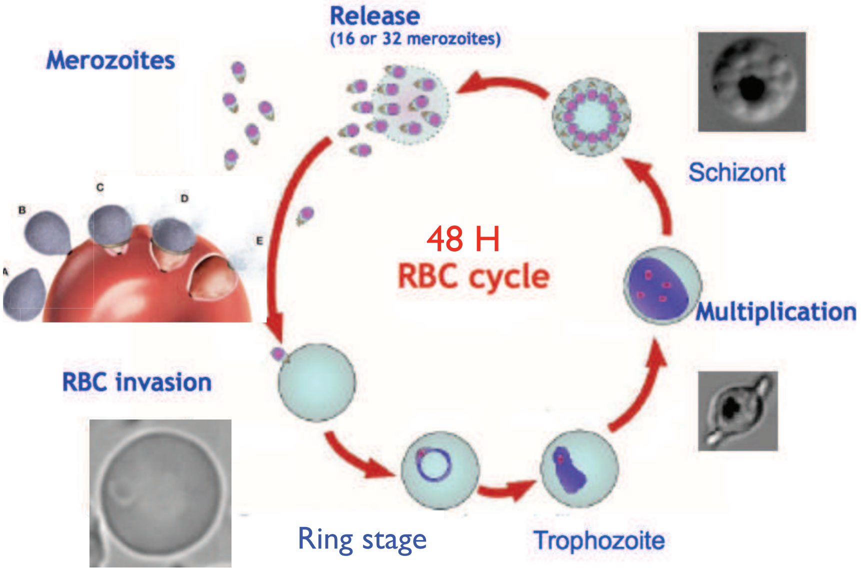

Figure 2.2: 48 hours life cycle of the *P. falciparum* in RBCs.

of the pore curls out and wraps into a toroidal rim whose major radius $r$ grows in time (Fig. 2.3B and 2.4A,B). This curling process is confirmed by direct observation of the first turn as presented in Fig. 2.4B., an outward curling of the iRBC membrane is then observed. In the last step, when $r$ reaches a critical value close to the radius $R$ of the iRBC, the membrane changes the sign of its curvature (*i.e.*, from concave to convex) and buckles, liberating and dispersing the remaining merozoites as shown in Fig. 2.3B. These data strongly suggest that buckling is necessary for efficient release and dispersal of the merozoites [1].

The striking similarities observed between the destabilization of the iRBC membrane and the bursting of artificial-sensitive copolymer-based vesicles (Fig. 2.1C), reported by Mabrouk et al. [48], suggest that a common elastic mechanism is involved in both systems. Since, healthy RBCs do not present such instability under osmotic stress alone, Malaria parasites modify and exploit the elasticity of the cell membrane like Mabrouk et al. with their polymersomes, to enable their egress. However unlike polymersomes, the actors responsible for such high natural curvature are still unknown for iRBCs and their determination are under current investigation.

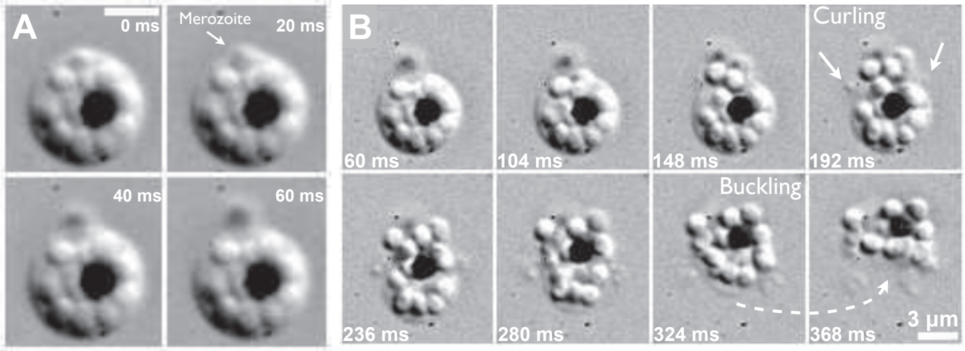

Figure 2.3: A. Snapshots of the osmotically triggered ejection of the first merozoite using DIC microscopy. Scale bar, 3 $\mu$m. B. Snapshots of the whole release process: pressure driven ejection of the first parasite (up to 148 ms); curling of the RBC membrane (192-324 ms) and final buckling of the membrane (324-368 ms) pushing the remaining merozoites forwards, far from their initial position (from [1]).

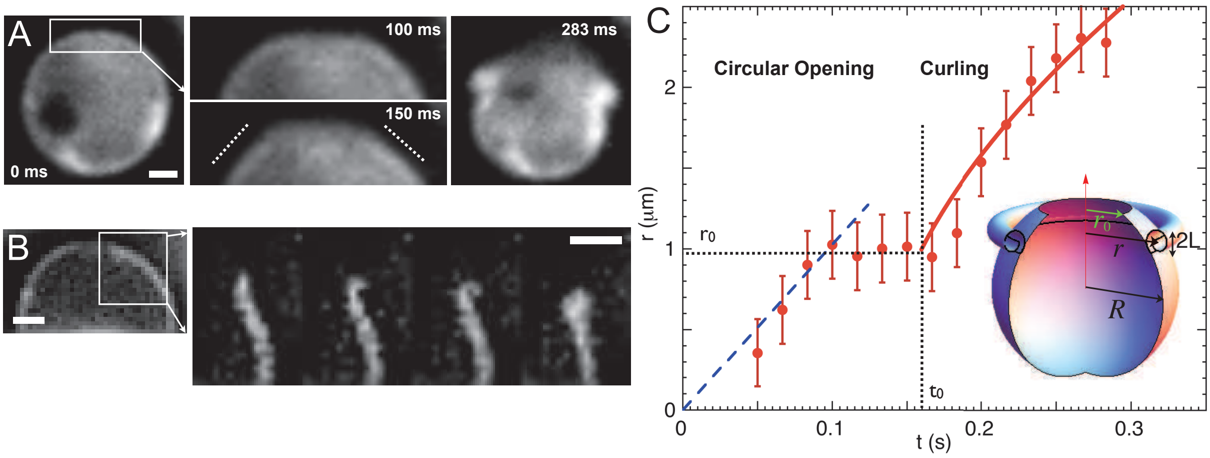

Figure 2.4: (A) Sequence of images of PKH26-labeled iRBC using fluorescence microscopy and showing: the initial iRBCs (0 milliseconds), the circular pore opening (100 ms), the shoulder type deformation of the RBC membrane (150 ms) followed by the membrane curling (283 ms). Scale bar, 1 $\mu$m. (B) Sequence of images of the first curl after the shoulder-type deformation (time lapse: 14.3 ms). Scale bar, 1 $\mu$m. (C) Kinetics of the pore opening with the radius $r$ of the pore as a function of time. Two regimes are identified: the circular opening and the curling taking place at $t_0$. The parameters used for the data analysis are represented both in the inset and on the curve: the pore radius when curling starts $r_0$ and the cell radius $R$. At any given time $t$, the opening is described by a pore radius $r$ and a rim radius $L$. The red solid line is a fit with eqn. 2.2. Error bars represent the error in the determination of the diameter of the pore. (from [1]).

### 2.1.3 Phenomenological approaches used in these two studies and their limitations

The curling of polymersomes membrane is driven by a molecularly imposed curvature $\kappa_0$ of the membrane opposite to and much higher than the initial curvature $\kappa = 1/R$ of the polymersome of radius $R$. According to the model by Mabrouk et al, once a pore nucleates, it grows because of the outer curling of the membrane releasing bending energy at a rate $Pe$. The dynamics of the rim is then controlled solely by the balance between $Pe$, and the viscous dissipation $Pv$ because of the movement of the growing rim in the outer medium.

Abkarian et al. proposed to describe the iRBC bursting with the same approach considering that at one point during the parasite development the iRBC membrane acquires a spontaneous curvature $\kappa_0$ different from a normal RBC and whose origin is yet to be determined [1]. The time variation of the rim bending energy is related to the variation in curvature of the spherical membrane elements from a curvature of $1/R$ to an opposite higher curvature of $1/L$ when wrapping on the rim (Fig. 2.1D): $P_e \approx \frac{1}{2}\kappa\frac{1}{L^2}2\pi r\dot{r}$, where $L \ll R$ is the radius of the rim. For the viscous dissipation, Mabrouk *et al.* estimated $P_v$ using the Stokes friction of a cylinder of radius $L$ and length $2\pi r$ (perimeter of the rim), moving at a speed $\dot{r}$ in a fluid of viscosity $\eta$: $P_v = \frac{4\pi\eta}{1/2+ln(2\pi r/L)}2\pi r\dot{r}$. The balance of these two terms leads to the following differential equation for r assuming that the slowly varying logarithmic term at the denominator is a constant $l_n$:

$$\dot{r} = \frac{\kappa l_n}{2\eta}\frac{1}{4\pi}\frac{1}{L^2} \tag{2.1}$$

Assuming a compact curling with a membrane thickness $e$, mass conservation leads to $L = \kappa_0^{-1}\sqrt{1 + r/r_c}$, hence a polynomial solution of Eq.2.1 reported in Mabrouk *et al.* [48]: $r^2 + 2rr_c = Dt$, where $D = \frac{\kappa l_n}{2e\eta}$ and $r_c = \frac{2\pi}{e\kappa_0^2}$. For iRBCs however, the pore nucleation is immediately followed by the circular opening up to a radius $r_0$, reached at a time $t_0$ (Fig. 2.4C). This brings a correction to the mass balance $\pi e(r^2 - r_0^2) = 2\pi r(\pi L^2 - \pi\kappa_0^{-2})$ proposed in [48] and to $L = \kappa_0^{-1}\sqrt{1 + (r - r_0^2/r)/r_c}$. The solution of Eq.2.1 becomes:

$$D(t - t_0) = (r - r_0)(r + r_0 + 2r_c) - 2r_0^2 ln(\frac{r}{r_0}) \tag{2.2}$$

As presented in Fig. 2.4C, Abkarian et collaborators measured the variations of $r$ as a function of time for individual events of iRBC opening and fitted their data using Eq. 2.2 to determine the values of the parameters $r_c$ and $D$ (reported in [1], solid curve in Fig. 2.4C). Knowing the thickness $e \approx 50$ nm measured by ultrasensitive force probe techniques on healthy RBCs [31] and using the fitted value of $r_c$, the authors deduced first the spontaneous curvature $\kappa_0 \approx 21.0 \pm 2.4\ \mu m^{-1}$ of the membrane for non labelled RBCs and $\kappa_0 \approx 11.5 \pm 2.4\ \mu m^{-1}$ for PKH26-labelled RBCs[1], corresponding to radii of curvature of the order of the membrane thickness. They have also measured the maximum pore radius $r_{max}$ as well as the rim size $L_{max}$ before buckling. Using the values of $\kappa_0$ and $r_c$ and the expression of $L$, one can compute $L(r_{max}) \approx 0.2\mu$m which is close to the measured values of the order of $0.4\mu$m and comforts again the fact that curling is due to a spontaneous curvature $\kappa_0$ acquired by the iRBC membrane. Subsequently, $\kappa_0$ should be sensitive to the modification of the iRBC lipid membrane. Indeed, the authors observed a decrease of $\kappa_0$ measured for PKH26-labelled cells whose outer leaflet has been enriched by these extra lipids.

Even though the modified model seem to fit the data and gives a reasonable value for the spontaneous curvature, it fails to predict the value obtained experimentally for $D$. Indeed, using the typical value for the RBC membrane bending modulus $\kappa \approx 50\ k_BT$ [59], the thickness $e \approx 50$ nm and the viscosity of the outer medium which is mainly water $\eta \approx 10^{-3}\ Pa.s$, setting $l_n \approx 4$, Abkarian et al. find a value $D \approx 8000\ \mu\text{m}^2/\text{s}$ two orders of magnitude larger than what reported in [1]. Since $D$ depends mainly on $e$ and $\eta$, several assumptions of the model have to be reconsidered to understand such a discrepancy, which are basically related to the geometry of the winding and the sources of dissipation in the problem.

For instance both models of Mabrouk et al. and Abkarian et al. are simply based on the assumption that curling is compact. This hypothesis can be easily challenged based on steric and dynamical arguments in the case of iRBCs. Indeed, the compact curling might be hampered by structures remaining attached to the iRBC membrane after egress such as the sub-membrane skeleton and the Maurer's clefts which are structures exported by the parasite, previously shown to remain attached to the RBC membrane after egress [3, 16, 46]. What is then the effect of such non compact winding on the dynamics of the pore ?

In addition other dissipative processes described by an effective viscosity $\eta_{eff}$ 2 orders of magnitude larger than $\eta$ would account for such a discrepancy. For example, another possible source of extra-viscous dissipation could come from the 2-dimensional (2D) membrane flow produced by the curling deformation. However it is not clear how to correctly calculate such a complex flow with a simple term in the energy balance described earlier. One crude approach to estimate such a 2D dissipation has been suggested in the supplementary files of Mabrouk et al. [48]. The authors considered that the viscous dissipation around the curling membrane edge could be represented by the same term as for a circular pore opening [65]: $\pi r^2 \eta_S (\frac{\dot{r}}{r})^2$. It is easy to show that $D$ is simply renormalized

---

[1] PKH-26 is a commercially available fluorescent lipid

as $D_{new} = \frac{D}{1+\frac{ln}{8\pi}\eta_S/\eta r_0}$ (supplementary files of [1]), where $\eta_S$ is the surface viscosity of the membrane. Viscosity measurements have been done on lipid membranes using many different techniques such as labeled molecular probe diffusion in bilayers [57], falling ball viscosimetry [19], phase-separated lipid domain diffusion [15], and pore-opening measurement techniques [7], establishing that $\eta_S$ is ranging from $10^{-9}$ N.s/m to $3.10^{-7}$ N.s/m. Consequently, $D$ can vary by a factor 100, depending on the type of membrane flow. Better estimate of the surface flow are necessary in such geometry.

Moreover, other aspects of the problem have been neglected. First, the role played by the eventual presence of the cytoskeleton in the case of iRBC membrane both on pore nucleation but also on its dynamics. Finally, both models in both systems have neglected the role of line-tension and of the spherical geometry.

Recently, we published a preliminary work on the role of spherical geometry [10]. But in this chapter, we present a more general and extended phenomenological model based on the sequence of pore opening we described in the earlier paragraph both for iRBCs and polymersomes, where basically we consider that the only difference between these two structures is the presence of a shear modulus in the membrane of iRBCs. In the first part, we study theoretically pore opening and curling destabilization due to the presence of a uniform spontaneous curvature in an 3D axisymmetric bio-membrane. We model axisymmetric curling with the revolution of a decentered Archimedean spiral leading to prescribed toroidal-like wrapping of the membrane. In this configuration, we look at the stability of an open pore depending both on line-tension and shear elasticity. Moreover, we explore in a second part the role surface dissipation resulting from the surface redistribution and discuss what role it plays on the dynamics over the outer fluid viscous dissipation.

## 2.2 General mechanical properties of lipid and diblock copolymer membranes

### 2.2.1 Bending in Fluid Membranes

Fluid membranes as chiefly studied in this manuscript consist of a bilayer of amphiphile molecules that are are lipids or diblock copolymers. When introduced into an aqueous environment, these amphiphilic molecules aggregate spontaneously into two mono-molecular layers held together by hydrophobic forces [18, 67]. This bilayer system can be modeled as a nematic liquid crystal where the director of the individual molecules coincides with the normal unitary vector $\hat{n}$ of the surface (see Fig.1.4). In this context, the classical concept of strain has no sense. What is relevant is not the infinitesimal separation of matter but the infinitesimal variation of the directors of the molecules (indeed, the model assumes that always the densities in each monolayer adjust optimally to the local shape). Then, in analogy with the strain $\frac{dr_i'-dr_i}{dr_i}$ along the direction $\hat{e}_i$ for solids, the deformation, along the same direction, in the liquid cristal system is quatified by the parameter $\Psi_i = \frac{dn_i'-dn_i}{dr_i}$, where $dn_i'$ and $dn_i$ are the infinitesimal variations (after an before bending) of the normal vector $\hat{n}$ in the direction $\hat{e}_i$. Considering naturally flat membranes and $\hat{e}_3$ parallel to the local normal vector, we get $\Psi_3 = 0$ and, $\Psi_1$ and $\Psi_2$ become exactly the local curvatures along $\hat{e}_1$ and $\hat{e}_2$. Therefore, two arbitrary perpendicular curvatures, should completely define the local modes of deformation in the membrane. In addition, the state of curvatures around any point of a surface, is given by the two fundamental invariants $\frac{1}{2}(\kappa_1+\kappa_2)$ and $\kappa_1\kappa_2$, which are the Mean and Gaussian curvature respectively ($\kappa_1$ and $\kappa_2$ are the principal curvatures [74]). In the classical curvature model for symmetric membranes, the local elastic energy $\mathcal{F}_{LC}$ (energy per unit surface) is written as an expansion of the invariants. Then, similar to Eq.3.2, to lowest order one obtains [67]

$$\mathcal{F}_B(\mathbf{r}) = \frac{1}{2}K_B\left(\kappa_1+\kappa_2\right)^2 + K_G\left(\kappa_1\kappa_2\right) \tag{2.3}$$

, where the two elastic constant $K_B$ and $K_G$ both have the dimension of an energy. They are called bending rigidity and Gaussian rigidity. The Eq.2.3 is usually known as Helfrich energy in reference to who popularized the expression in 1973 and has been specially successful for the theoretical modeling of the configurations and shape transformations of vesicles and red blood cells [5].

## 2.2.2 Mechanical Properties of infected Red Blood Cells

### Structure of a healthy RBC membrane

The red blood cell membrane (RBC) is one of the most thoroughly researched structures in biology. The membrane material is a composite design based on a fluid lipid bilayer supported by a scaffolding of interconnected proteins and studded by a superficial forest of peptidoglycans [31] (Figure 2.5). Beyond the 4 nm thick lipid bilayer, the exterior glycocalyx extends the bilayer foundation of the membrane to the order of 10 nm as deduced from electron microscopy and studies of electrophoretic mobility [31]. Representing the foundation for nodes of the spectrin network, the junctional complexes separate the network from the lipid interface by 10 nm. Finally, with values of contour length and network topology known to characterize the spectrin cytoskeleton, simulations of spectrin networks with different numbers of segments per chain [5] have indicated that the chains extend 20–30 nm from the junctional complexes into the cytoplasm. Hence, from these estimates of compact molecular dimensions and simulations of polymer networks, a red cell membrane is expected to span 40–50 nm in thickness and, if squeezed, to exhibit a structural hardness of 20–25 nm.

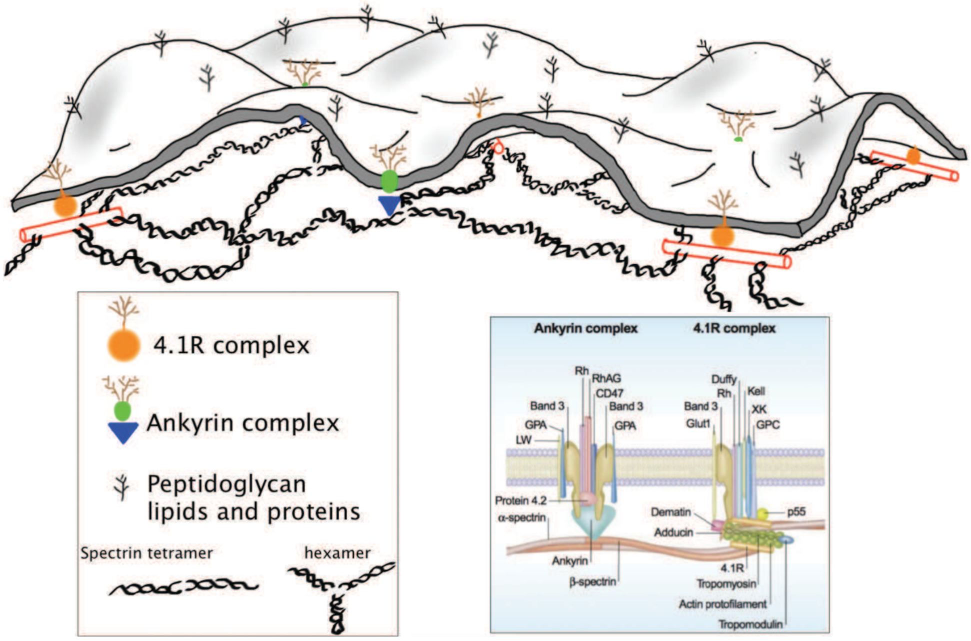

Figure 2.5: Schematic drawing of the membrane-cytoskeleton interactions and coupling.

Mature human RBCs lack nuclei and transcellular filaments, so the deformability of a RBC is a result of three factors: the ratio of membrane surface area to cell volume, the viscosity of the cytoplasm, and the deformability of the membrane. Membrane deformability may be characterized by three elastic parameters: the area expansion (bulk) modulus, $K$; the shear modulus $G$; and the bending stiffness $B$ [56]. The lipid bilayer strongly resists changes in area and therefore dominates the behavior of the membrane in both isotropic expansion and bending [56]. The resistance of the red cell membrane to shear deformations is primarily attributable to the elasticity of the underlying skeleton. Both the shear modulus of the skeleton, and the area expansion modulus of the skeleton, $K$, affect the over all shear modulus of the membrane, $G$ as measured by micropipette aspiration [56].

### Bending energy of fluid membranes with a spontaneous curvature

Typically, the density of bending energy for a membrane bearing a spontaneous curvature can be simply expressed by means of the Helfrich bending energy of the Eq.2.3 in the following manner

$$\mathcal{F}_B(\mathbf{r}) = \frac{1}{2}K_B\left(\kappa_1 + \kappa_2 - \kappa_0\right)^2 + K_G\left(\kappa_1\kappa_2\right) \tag{2.4}$$

Where $\kappa_0$ is the so-called spontaneous curvature and is supposed to reflect a possible asymmetry between the membrane leaflets or a difference of area. This parameter is crucial to explain curling: the energy in Eq.2.4 decreases when the membrane bend on itself so that, the mean curvature would tend to the spontaneous one. The physical origin of the spontaneous curvature could be either a different chemical environment on both sides of the membrane, or a different chemical composition of the two monolayers. The accepted bending rigidity of the membrane has been established around $K_B = 2.0 \times 10^{-19}$ N.m [38]. Although this value of $K_B$ is fairly reliable, sparse experimental measurements are available for $K_G$ [70, 68, 69, 35], but all seem to give values $-K_G/K_B$ ranging from $-0.31$ to $-0.84$ for bilayers of lipid mixtures for instance (e.g. DOPC:SM:Chol). According to the Gauss-Bonnet theorem of differential geometry, the total surface integral of the right-hand side of Eq.2.4 depends only on the topological genus of the membrane and of the presence of a boundary (e.g. a pore) and therefore should play a role in our case. However, we will demonstrate later that for large enough pore this term can be neglected.

### Shear elasticity of the membrane

The shear resistance of RBCs membrane is only related to the underlying spectrin network. It is clear from observations of large extensions of intact RBCs and large expansions of detergent-extracted cytoskeletons that the spectrin network is hyperelastic [56]. Energetically, a hyperelastic membrane network can be represented by an elastic density energy (energy per unit area) given by the relation [24]:

$$F_G = \frac{G}{2}\left(\lambda_1^2 + \lambda_2^2 - 2\right) \tag{2.5}$$

, where $\lambda_1$ and $\lambda_2$ are the principal stretch ratios for surface deformation of a material element.(Starting with a square element $L_0 \times L_0$, $\lambda_1 = L_1/L_0$ and $\lambda_2 = L_2/L_0$ when the element is stretched into a rectangle $L_1 \times L_2$.) The elastic coefficient $G$ is analogous to the shear modulus in a solid shell and the experimental value obtained for healthy RBCs is approximately $2.5 - 5 \times 10^{-6}$ N/m [33].

### Structure and shear elasticity of the iRBCs membrane

During the intra-erythrocytic development, the malaria parasite *Plasmodium falciparum* causes structural, biochemical, and mechanical changes to their host. Major structural changes include the formation of parasitophorous vacuoles that surround the growing parasite in their host RBCs, loss of cell volume, the appearance of small nanoscale electron-dense protrusions named knobs on the membrane surface and consisting of parasite proteins exported to the red cell membrane and sub-membrane skeleton [50] (see Figure

2.6B). More recent studies have revealed that the parasite might export several hundreds of proteins, as well as membrane compartments, to the red cell and divert enzymatic and structural host proteins to make the erythrocyte a suitable environment for its growth. Other membrane structures transposed by the parasite in the cytoplasm of its host cell, referred to as Maurer's clefts (see Figure 2.6B), and proposed to generate from the parasitophorous vacuole membrane, are central to the transport of parasite proteins to the RBC membrane. They tightly interact with the membrane even upon merozoite release. From the biochemical standpoint, a considerable amount of hemoglobin is digested by the parasites during development and converted into insoluble polymerized forms of heme, known as hemozoin. Hemozoin appears as brown crystals in the vacuole of parasite in later maturation stages (see Figure 2.6A).

Several studies indicate that malaria parasites induce modifications to the plasma membrane and its underlying spectrin cortex before egress. First, work on another malaria-causing parasite, P. knowlesi, revealed that merozoites alter the phospholipid asymmetry of the membrane bilayer of infected RBCs, inducing a relative enrichment of cone-shaped lipids, such as phosphatidylethanolamine, in the outer leaflet [30]. Second, recent studies have shown that parasite-secreted proteases modify and degrade the spectrin cytoskeleton before egress [4, 64, 17, 45] and that treatment with protease inhibitors prevents egress [12]. Also, hijacking of the host protease calpain-1 by P. falciparum merozoites is essential to their egress from infected RBCs [11].

Two major mechanical modifications that are induced by this remodeling are an increased cytoadherence of the invaded RBC membrane to vascular endothelium and other RBCs, important for its sequestration in microvasculature, and a loss of RBC deformability. The associated shear modulus increases of more than 100% for the later developmental stages [55] (see Figure 2.6C).

Taken together, these studies and the observed membrane curling during parasite egress [1] suggest the following exit strategy: parasites induce a spontaneous curvature in the RBC membrane, opposite in sign to its mean curvature before their egress; to minimize the mismatch between the spontaneous curvature and the membrane curvature, a pore opens in the membrane, followed by outward membrane curling, and finally eversion.

### Pore opening and the importance of line tension

Under moderate tensions of $10^{-6}$ N/m, membranes may expand under tension thanks to the reservoir of membrane area stored in wrinkles due to thermal fluctuations [23]. At sufficiently high stress of $10^{-3}$ N/m however, the membrane can support only few % of expansion before rupturing. The amphiphilic molecules rearrange themselves to minimize exposure of their hydrocarbon regions to water. The reorganization of the molecules

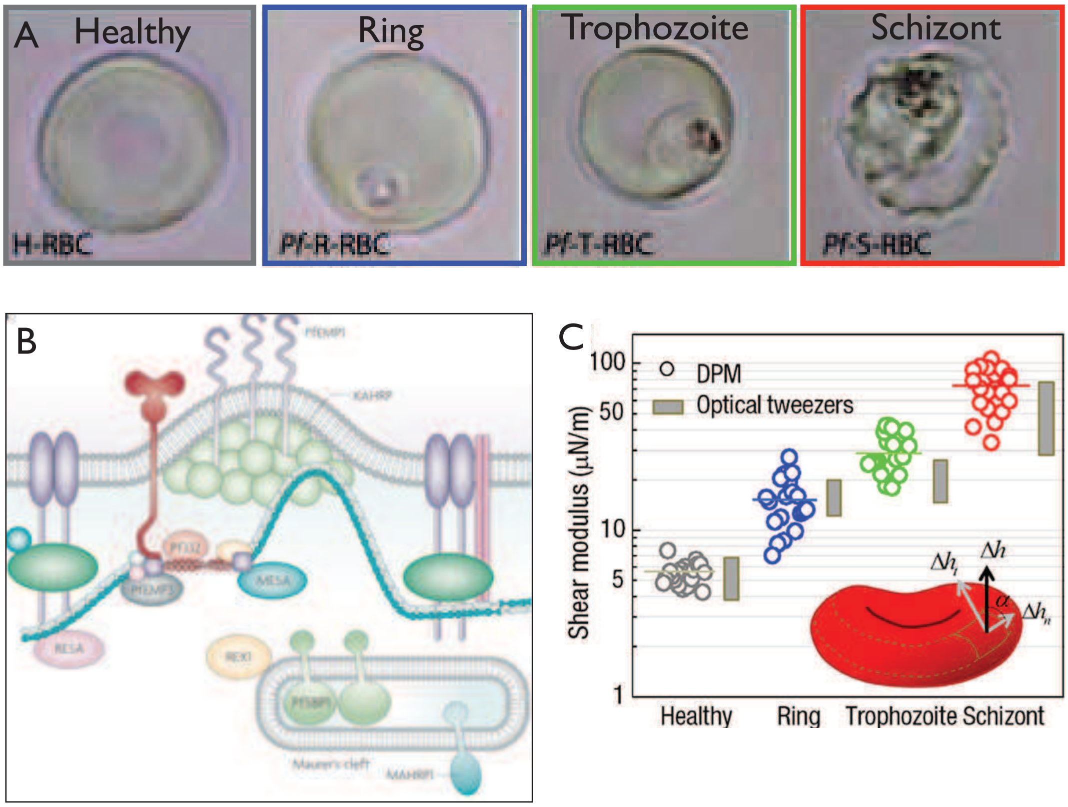

Figure 2.6: A-Different developmental stage of the parasite into a RBC: healthy RBC, early ring stage, trophozoite stage, and schizont stage before egress (from [55]). B-Schematic drawing of the modified structure of an iRBC (from [50]). C- Mechanical measurement of the shear modulus of the membrane using Diffraction Phase Microscopy (DPM) of an iRBC at the different stages represented in (A) (from [54]).

implicates an energy cost for the formation of edges. This is expressed by a line tension $\gamma$, which is an energy per unit length along the edge. This has been measured to values of the order of $\gamma \sim 10$ pN in case of lipid vesicles [40]. We will use this value in the following sections. Therefore, the energy associated with the formation of a pore of radius $l$ in the plasma membrane, is written simply by:

$$U_\gamma = 2\pi l\gamma \tag{2.6}$$

, where the energy cost of the presence of an edge is simply proportional to the perimeter of the pore.

## 2.3 Potential Energies for the membrane dynamics

An obvious condition for the curling of a thin material, is the presence of an edge. This edge in axisymmetric geometry is represented by a hole. The nucleation of the pore at the onset of curling is attributed to the high surface tension induced by osmotic inflation just before egress in the case of iRBCs [29, 1] and UV-shining in the case of polymersomes [49]. Here, as in the case of polymersomes, we suppose that, since the radius of nucleation of the pore, $r^*$, is large enough, the rapid leaking of the internal content [65] produces a fast relaxation of the surface tension of the membrane (for iRBCs for instance, the radius $r_0$ of the circular pore before curling is measured to be a fraction of the size of the cell, see Figure 2.4). Consequently, once the pore is formed, we neglect energy terms coming from the tension and we suppose that the dynamics of bursting is solely governed by the Helfrich bending energy of the bilayer, the shear energy of the spectrin and line tension energy of the edge of the pore.

### 2.3.1 Bending Energy

For axially symmetric membranes, such as that displayed in Fig.2.7, the shape can be described by the function $r(\psi)$, where $r$ is the distance from the symmetry axis to the surface, $\psi(s)$ is the angle between the normal vector and the symmetry axis and $s$ is the arclength position. The principal curvatures are respectively, $\kappa_1 = \frac{d\psi}{ds}$ and $\kappa_2 = \frac{\sin\psi}{r}$ [74] and Eq.2.4 gives

$$\mathcal{F}_B = \frac{K_B}{2}\left(\frac{d\psi}{ds} + \frac{\sin\psi}{r} - \kappa_0\right)^2 + K_G\left(\frac{\sin\psi}{r}\frac{d\psi}{ds}\right) \tag{2.7}$$

During curling, the membrane is described as a spherical cap of radius $R$ and opening angle $\theta$ attached to a quasi-toroidal rim (axisymmetric curled sector) where the local

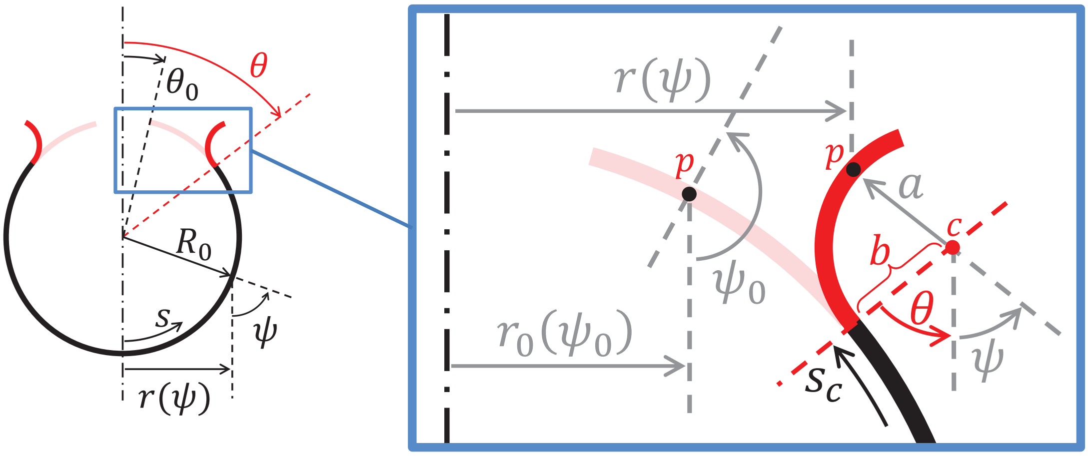

Figure 2.7: Schematic of a spherical shell in a early stage of curling with axial symmetry.

radius of curvature will be equivalent to a slow-varying function $a(\psi) > 0$ so that, in the rim, we write $\frac{d\psi}{ds} = -1/a$. Denoting the natural radius of curvature by $a_0 = -1/\kappa_0 > 0$, we see that the local decrease of bending energy density in the rim is

$$(\triangle\mathcal{F}_B)_{rim} = -\frac{1}{2}\frac{K_B}{a_0^2}\left[\left(1+2\frac{a_0}{R_0}\right)^2 - \left(1-\frac{a_0}{a}+\frac{a_0}{r}\sin\psi\right)^2\right] - \frac{K_G}{a_0^2}\left[\frac{a_0^2}{a}\frac{\sin\psi}{r} + \left(\frac{a_0}{R_0}\right)^2\right] \tag{2.8}$$

, where $R_0$ is the radius of the membrane immediately after the pore is formed. We must distinguish the cap radius, $R = R(\theta)$, of the initial one, $R_0 = R(\theta_0)$, to account the possibility of a dynamic variation due to surface flow. The decrease of bending energy density in the cap is given by the instantaneous value of its radius $R$, then:

$$(\triangle\mathcal{F}_B)_{cap} = \frac{1}{2}\frac{K_B}{a_0^2}\left[\left(1+2\frac{a_0}{R}\right)^2 - \left(1+2\frac{a_0}{R_0}\right)^2\right] + \frac{K_G}{a_0^2}\left[\left(\frac{a_0}{R}\right)^2 - \left(\frac{a_0}{R_0}\right)^2\right] \tag{2.9}$$

The total bending energy released, $U_B$, for an arbitrary opening angle $\theta$, corresponds to the integration of $(\triangle\mathcal{F}_B)_{rim}$ and $(\triangle\mathcal{F}_B)_{cap}$ in the rim and cap surfaces, therefore

$$\frac{U_B}{2\pi R_0^2} = \{1-\cos\left[\psi_0(s_c)\right]\}\left(\triangle\mathcal{F}_B\right)_{cap} + \int_{\psi_0(s_c)}^{\pi-\theta_0} (\triangle\mathcal{F}_B)_{rim} \times \sin\psi_0 \cdot d\psi_0 \tag{2.10}$$

, where $\psi_0$ is the angle between the normal vector and the axis of symmetry of an arbitrary point, $p$, just after the nucleation of the pore (in contrast with the angle $\psi$ of the same point $p$ during curling, see Fig.2.7). Accordingly, $\psi_0\left(s_c\right)$ is the angle $\psi_0$ associated with the first boundary of the curling region at $s = s_c$, so $\psi_0(s_c) = \psi(s_c) = \pi - \theta$ only when $R = R_0$. Since the initial polar distance of any point after poration is expressed by $r_0 = R_0 \sin\psi_0$, the angle $\psi_0(s)$ constitutes the initial local configuration of the membrane.

The general value of $\psi_0(s_c)$ for $R \neq R_0$ can be calculated easily through the conservation of the global area:

$$2\pi R_0^2 (1 + \cos\theta_0) - 2\pi R^2 (1 + \cos\theta) = 2\pi R_0^2 \int_{\psi_0(s_c)}^{\pi - \theta_0} \sin\psi_0 \cdot d\psi_0$$

and therefore,

$$\cos[\psi_0(s_c)] = 1 - \left(\frac{R}{R_0}\right)^2 (1 + \cos\theta) \tag{2.11}$$

This formula is very important for the subsequent calculations because it allows us to define the limits for the surface integrals of the different density energies in the problem.

In consideration to the slow variation of $a(\psi)$, we proceed with the limit of very small dispersion of the curvature center position of the curling profile. Thus, the average point (denoted by $c$ in the Fig.2.7) will be used as a reference for the geometrical description. For instance, if $b$ is the distance from the surface at $s = s_c$ to the center point $c$, the polar length $r$ in the rim can be expressed by

$$r = (R + b)\sin\theta - a\sin\psi \tag{2.12}$$

In the rim, the relationship between the angles $\psi$ and $\psi_0$ can be obtained from the local conservation of surface area: $rad\psi = -r_0 R_0 d\psi_0$, where the negative sign reflects the change of sign of the Gaussian curvature. Therefore,

$$\left(\frac{d\psi}{d\psi_0}\right)_{rim} = \frac{-\frac{R_0}{a}\sin\psi_0}{(\frac{R}{R_0} + \frac{b}{R_0})\sin\theta - \frac{a}{R_0}\sin\psi} \tag{2.13}$$

, where the subindex, *rim*, implies that the derivative is taken in some place on the rim. Using the condition $\frac{a}{R_0} \lesssim \frac{b}{R_0} \ll 1$, we have that, for large nucleation pore (so $\theta$ is never close to zero), the Eq.2.13 can be approximated by

$$\left(\frac{d\psi}{d\psi_0}\right)_{rim} = -\left(\frac{R_0}{a}\right)\left(\frac{R_0}{R}\right)\frac{\sin\psi_0}{\sin\theta} \tag{2.14}$$

Returning to the estimation of the bending energy (given by Eq.2.10), we see that for very large spontaneous curvature and large radius of nucleation of the pore, the term in $K_G$ can be neglected. Actually, for $\frac{a_0}{R} \ll 1$ the Eq.2.12 gives $\frac{a_0}{r}\sin\psi \approx \frac{\sin\psi}{\sin\theta}\left(\frac{a_0}{R}\right) \ll 1$ and the densities of energies (Eq.2.8 and Eq.2.9) are related by

$$(\triangle\mathcal{F}_B)_{cap} \ll (\triangle\mathcal{F}_B)_{rim} \approx -\frac{1}{2}\frac{K_B}{a_0^2}\left[1-\left(1-\frac{a_0}{a}\right)^2\right]$$

. Therefore, using Eq.2.10, at lead order, the released bending energy writes

$$U_B = -\pi K_B\left(\frac{R_0}{a_0}\right)^2\left\{\cos\theta_0 + 1 - \left(\frac{R}{R_0}\right)^2(1+\cos\theta) - I\left(\theta\right)\right\} \tag{2.15}$$

Where $I(\theta)$ represents the integral

$$I\left(\theta\right) = \int_{\psi_0(s_c)}^{\pi-\theta_0}\left(1-\frac{a_0}{a}\right)^2\sin\psi_0\cdot d\psi_0 \tag{2.16}$$

In the limit of $R = R_0$ and infinitely compact curling ($a \to a_0$ in all the rim), the function $I(\theta)$ is neglected and $U_B$ becomes analogous to the bending potential energy used in the model of curling of polymersomes [49].

In order to estimate the bending energy of a more realistic mode of curling, we consider the first order variation of the function $a(\psi)$, then

$$\frac{da}{d\psi} = \frac{h_c}{2\pi} \tag{2.17}$$

Where $h_c$ is a constant that can be interpreted as an effective thickness of the membrane (thicker than its absolute thickness $h$, see inset Fig.2.8). Now, combining Eq.2.17 with Eq.2.14 we get

$$\sin\psi_0\cdot d\psi_0 = -\left(\frac{2\pi R\sin\theta}{h_c R_0^2}\right)a\cdot da \tag{2.18}$$

and therefore, the Eq.2.16 gives

$$I\left(\theta\right) = 2\left(\frac{R}{R_0}\right)\frac{\sin\theta}{\beta}\left[\frac{1}{2}\left(\frac{b}{a_0}-1\right)\left(\frac{b}{a_0}-3\right)+\ln\left(\frac{b}{a_0}\right)\right] \tag{2.19}$$

Where $\beta = \frac{h_c R_0}{\pi a_0^2}$ is a geometric parameter that characterizes curling geometry. The integration limits for $a$ has been considered from $b$ to $a_0$ (which is compatible with the condition of zero moment at the free edge). Also, after the integration of the Eq.2.18, the relationship between $b$ and $\theta$ is obtained:

$$\frac{b}{a_0} = \sqrt{1+\frac{\beta}{\sin\theta}\left[\frac{R_0}{R}\left(1+\cos\theta_0\right)-\frac{R}{R_0}\left(1+\cos\theta\right)\right]} \tag{2.20}$$

. Replacing Eq.2.20 into Eq.2.19 we can verify that the function $I\left(\theta\right)$ satisfies the property of compact curling:

$$\lim_{\beta\to 0} I\left(\theta\right) = 0$$

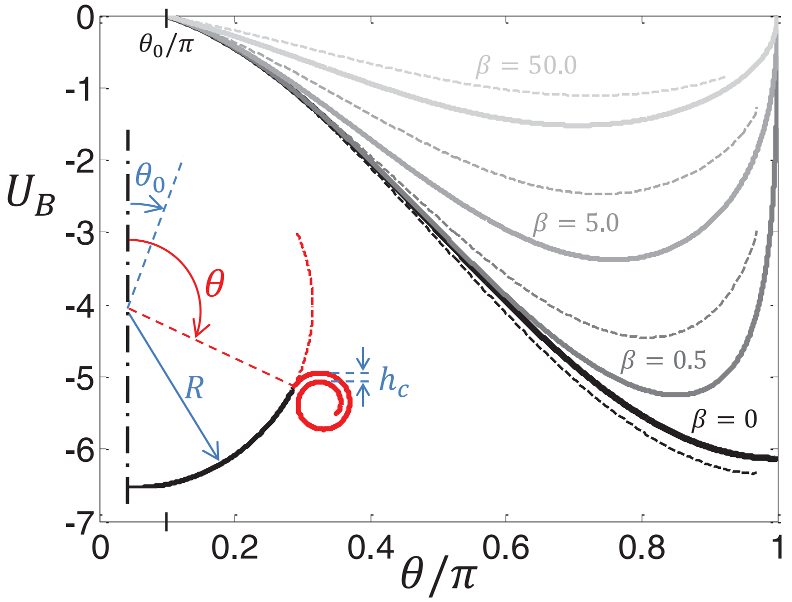

Figure 2.8: The released rim bending energy, $U_B$, as a function of the pore opening angle $\theta$ for different $\beta$. $U_B$ is plotted in units of $K_B R_0^2/a_0^2$. Solid lines are the resultant values from the combination of Eq.2.20, Eq.2.19 and Eq.2.15 (analytical approximation of the model); while the dashed lines are the respective numerical results obtained from the evaluation of Eq.2.8 after solving numerically Eq.2.13 coupled to Eq.2.17.

Combining Eq.2.20, Eq.2.19 and Eq.2.15, we obtain an approximation $U_B = U_B(\theta, R, \theta_0, \beta)$ which is analytical but valid only for large nucleation pores and $a \ll R_0$. In Figure 2.8, we show both such analytical approximation of $U_B$ with the opening angle $\theta$ (solid lines) together with its full value (dashed lines) obtained directly from Eq.2.8 (with $K_G = 0$ and $a_0 = R_0/100$) after solving numerically Eq.2.13 coupled to Eq.2.17. The curves are shown for different values of $\beta$, at an identical angle of poration $\theta_0 = \pi/10$ and for a fixed cap radius $R = R_0$. Interestingly, there is a minimum in the energy which is a direct consequence of the three-dimensional non-compact curling: since $U_B$ is proportional to the rim radius, $l = R\sin(\theta)$, curling will slow down and then stop as $l$ decreases, since less and less elastic energy is released into the rim.

This result is a key point that could play an important role in curling dynamics. Indeed, previous works [48, 1] are simply based on the assumption of compact curling of initially flat membranes, which implies in our approach $\beta \sim 0.1$, where no minima in the bending energy are present. However, this value of $\beta$ is quite unrealistic either for iRBCs or for polymersomes. For instance, for iRBCs compact curling might be hampered by structures remaining attached to the iRBC membrane, after egress, such as the sub-membrane skeleton and/or the Maurer's clefts which are structures exported by the parasite, previously shown to remain attached to the RBC membrane [3, 16, 46]. Moreover, viscous effects, that we will explore later in this manuscript prevent contact and a consequent volume of liquid can be trapped in the toroidal rim increasing artificially $h_c$ to values much higher than $h$. In this case, large values of $\beta$ should be considered in the problem. For instance, if $h_c \sim 20h$, $\beta \sim 4$, showing that the dynamics of curling will be influenced early on by the spherical geometry of the problem. Curling will slow down close to the equator of the membrane. This is consistent with the work reported in [1] (Fig. 2.3B) where the membrane curling slows down after passing the equator and where the membrane buckles.

### 2.3.2 Shear energy of the spectrin

The shear elastic energy due to the spectrin is taken under the hypothesis that its resting state coincides with the initial configuration after the formation of the pore (this idea is sustained with the concept of large nucleation pore, where, because of the leak-out of internal liquid, the tensions in the membrane are rapidly relaxed). Therefore, the stretch ratios in the rim are defined as $\lambda_1 = \frac{a}{R_0}\frac{d\psi}{d\psi_0}$ and $\lambda_2 = r/r_0$, and, by the local surface area conservation: $\lambda_1 = 1/\lambda_2 = \lambda_{rim}$. With Eq.2.5 we find directly that the amount of density of shear energy in the rim is

$$(F_G)_{rim} = \frac{G}{2}\left(\lambda_{rim}^2 + \frac{1}{\lambda_{rim}^2} - 2\right) \tag{2.21}$$

Also, from Eq.2.14, we see that

$$\lambda_{rim} \approx -\frac{R_0}{R}\frac{\sin\theta}{\sin\psi_0} \tag{2.22}$$

In the cap, the density of shear energy depends on $R/R_0$ (in the resting state of the spectrin $R/R_0 = 1$ and the shear must be equal to zero). By local conservation of area in the cap, we have

$$\left(\frac{d\psi}{d\psi_0}\right)_{cap} = \left(\frac{R_0}{R}\right)^2 \frac{\sin\psi_0}{\sin\psi} \tag{2.23}$$

After an integration by parts of Eq.2.23, we get

$$\sin\psi = \left(\frac{R_0}{R}\right)\sqrt{2\left(1-\cos\psi_0\right) - \left(\frac{R_0}{R}\right)^2\left(1-\cos\psi_0\right)^2}$$

, therefore

$$\lambda_{cap} = \sqrt{\frac{(1+\cos\psi_0)}{2-\left(\frac{R_0}{R}\right)^2(1-\cos\psi_0)}} \tag{2.24}$$

, where $\lambda_{cap} = \frac{R}{R_0}\left(\frac{d\psi}{d\psi_0}\right)_{cap}$ is the tangential stretch ratio in the cap. Then, the amount of density of shear energy in the cap, in analogy to Eq.2.21, is

$$(F_G)_{cap} = \frac{G}{2}\left(\lambda_{cap}^2 + \frac{1}{\lambda_{cap}^2} - 2\right) \tag{2.25}$$

The total shear energy, $U_G$, correspond to the sum of the surface integrals of $(F_G)_{cap}$ and $(F_G)_{rim}$ on the cap and rim respectively. Therefore,

$$\frac{U_G}{\pi R_0^2 G} = A_{cap}(\theta, R) + A_{rim}(\theta, R) \tag{2.26}$$

where,

$$A_{cap}(\theta, R) = \frac{2}{G}\int_0^{\psi_0(s_c)} (F_G)_{cap} \times \sin\psi_0 \cdot d\psi_0$$

and

$$A_{rim}(\theta, R) = \frac{2}{G}\int_{\psi_0(s_c)}^{\pi-\theta_0} (F_G)_{rim} \times \sin\psi_0 \cdot d\psi_0$$

The analytical expressions for these functions (valid for $\lambda_{cap}$ and $\lambda_{rim}$ established in Eq.2.24 and Eq.2.22 ) are

$$A_{rim}(\theta, R) = \frac{\sin^2\theta}{2}\left(\frac{R_0}{R}\right)^2 \ln\left\{\frac{(1+\cos\theta_0)\,(1+\cos[\psi_0(s_c)])}{(1-\cos\theta_0)\,(1-\cos[\psi_0(s_c)])}\right\} +$$

$$+\frac{1}{\sin^2\theta}\left(\frac{R}{R_0}\right)^2\left\{\cos\theta_0 + \cos[\psi_0(s_c)] - \frac{1}{3}\left(\cos^3[\psi_0(s_c)] + \cos^3\theta_0\right)\right\} - 2\left(\cos[\psi_0(s_c)] + \cos\theta_0\right)$$

and

$$A_{cap}(\theta, R) = 2\left(\frac{R}{R_0}\right)^4\left[1-\left(\frac{R_0}{R}\right)^2\right]\ln\left\{1-\frac{1}{2}\left(\frac{R_0}{R}\right)^2+\frac{1}{2}\left(\frac{R_0}{R}\right)^2\cos[\psi_0(s_c)]\right\} +$$

$$-2\left[1-\left(\frac{R_0}{R}\right)^2\right]\ln\left\{\frac{1}{2}+\frac{1}{2}\cos[\psi(s_c)]\right\} + \left[\left(\frac{R_0}{R}\right)^2+\left(\frac{R}{R_0}\right)^2-2\right]\{1-\cos[\psi_0(s_c)]\}$$

Using Eq.2.6, the increase of energy associated with the line tension in the edge of the pore is

$$U_\gamma = 2\pi R_0 \gamma \left( \frac{r\left(s_f\right)}{R_0} - \sin\theta_0 \right) \tag{2.27}$$

, where $r\left(s_f\right)$ is the polar distance of the free edge. Since $\frac{r(s_f)}{R_0} \approx \left(\frac{R}{R_0}\right)\sin\theta$, we make the approximation

$$U_\gamma = 2\pi\gamma R_0 \left[ \left( \frac{R}{R_0} \right) \sin\theta - \sin\theta_0 \right] \tag{2.28}$$

. For $R = R_0$, the cap is in its resting state and the ratio between the shear energy and the line tension energy is therefore

$$\frac{U_G}{U_\gamma} = \frac{1}{2}\frac{R_0 G}{\gamma}\frac{A_{rim}}{\sin\theta - \sin\theta_0} \tag{2.29}$$

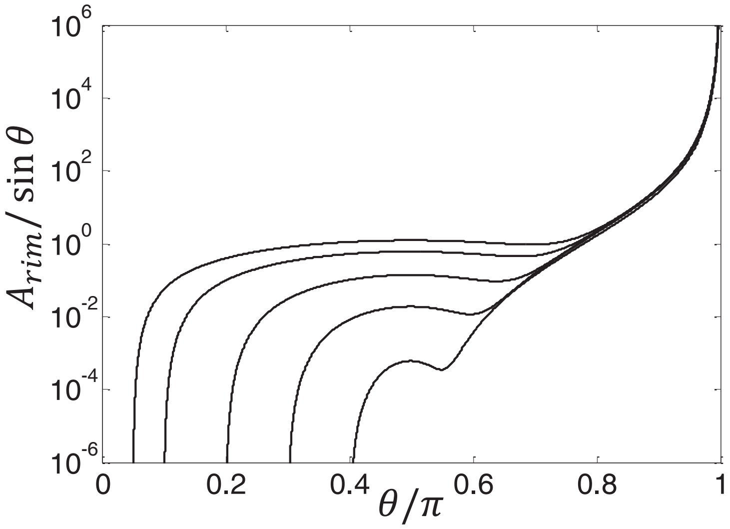

Figure 2.9: Geometric prefactor $A_{rim}\left(\theta, R = R_0\right)$ of the spectrin shear energy over the normalized radius of the pore $\sin\theta$. Each curve has a different $\theta_0$ (intersecting points with the horizontal axis), from left to rigth: $\theta_0 = 0.05\pi$; $0.1\pi$; $0.2\pi$; $0.3\pi$; $0.4\pi$.

In Eq. 2.29, $\gamma/G$ defines a characteristic radius where shear dominates. As shown in Fig.2.9, the function $A_{rim}/\sin\theta$ is small on a large interval of $\theta$ (it is much bigger than the unity only when $\theta \gtrsim 0.9\pi$). In particular for $\theta_0 \approx \pi/10$ (which is the typical value for the parasite egress), $A_{rim}/\sin\theta$ reaches rapidly a plateau with a value close to one. Thus, shearing of the spectrin network can be considered relevant (for $\theta < 0.9\pi$) only when $R_0 > 10\gamma/G$. Since in a healthy RBCs $\gamma/G \approx 4$ $\mu$m, Fig. 2.9 shows that during the egress, the spectrin cortex (with $G \sim 10$ $\mu$N/m) should not play an important role.

### 2.3.3 Curling nucleation: role of shear resistance versus line tension

Even if $G$ is very large, we can not expect shear resistances in an early stage of curling to be important, since the initial configuration of the membrane coincides with the resting state of spectrin. Therefore, soon after the nucleation of the pore, the necessary condition for curling is that the negative variation of the bending energy with respect to $\theta$ is larger than the associated increment in the energy associated to the line tension, otherwise the pore will close. Thus, in the critical situation:

$$\left[\frac{\partial U_B}{\partial \theta}\right]_{\theta=\theta_0} + \left[\frac{\partial U_\gamma}{\partial \theta}\right]_{\theta=\theta_0} = 0$$

, and therefore, for $a = a_0$ and $R = R_0$ we have

$$\frac{R_0}{a_0^*} = \sqrt{\frac{2\gamma R_0}{K_B \tan\theta_0}} \tag{2.30}$$

, where $R_0/a_0^*$ is the normalized critical natural curvature for curling to occur (at least in a first stage). The formula above shows that the critical spontaneous curvature increases dramatically for small initial angles (it tends to infinity when $\theta_0 \to 0$).

In order to calculate the conditions of curling to proceed, we calculate the total potential energy of the curling denoted by

$$U = U_B + U_\gamma + U_G \tag{2.31}$$

, where each term is given by there respective analytical approximations given in Eq.2.15, Eq.2.28 and Eq.2.26. In Fig.2.10 the total potential energy, for $R = R_0$ and $R_0/a_0 = 35 > R_0/a_0^* = 33$, is shown as a function of $\theta$. Following the same method of the numerical computation of the energies in Fig.2.8, both the analytical approximation (red color line) and numerical approach (black color line) have been plotted (the numerical approach is based in the evaluation and integration of the respective energy densities after solving Eq.2.13 coupled to Eq.2.17). The comparison of the principal curves shows that, due to the simplifications, the analytical approach looses the resolution of the oscillations inherent to the cycloidal nature of axisymmetric curling. This can imply an important conflict wit models forgetting the axisymmetric nature of the problem, because when $R_0/a_0$ is not large enough, a local minimum appears very close to the initial angle $\theta_0$ (see zoom-inset of Fig.2.10), which could eventually prevent a further propagation of the curling. The energy barrier centered around $\theta = 0.15\pi$ can not be overcome with thermal activation because $0.02 \times K_B R_0^2/a_0^2 \approx 2 \times 10^3\ k_B T$. In this situation, although $1/a_0 > 1/a_0^*$, the curling is rapidly blocked after poration, so the critical curvature for a relevant curling dynamics must be larger than the one proposed in Eq.2.30. For instance, when $R_0/a_0 \approx 43$, under the same remaining conditions of the plotting, the local minimum disappears (grey line in the zoom-inset of Fig.2.10). In Fig.2.10, we can also see that the contribution of the shear resistance to the total potential energy is relevant only for high opening angles (the dashed lines are the respective $U$-functions for $G = 0$). That is in accordance with what has been established before: during curling with high spontaneous curvature, the shear resistance is dominant only when the radius of the cell is much larger than the characteristic length $\gamma/G$ (for healthy RBCs, $\gamma/G \approx 4$ $\mu$m ).

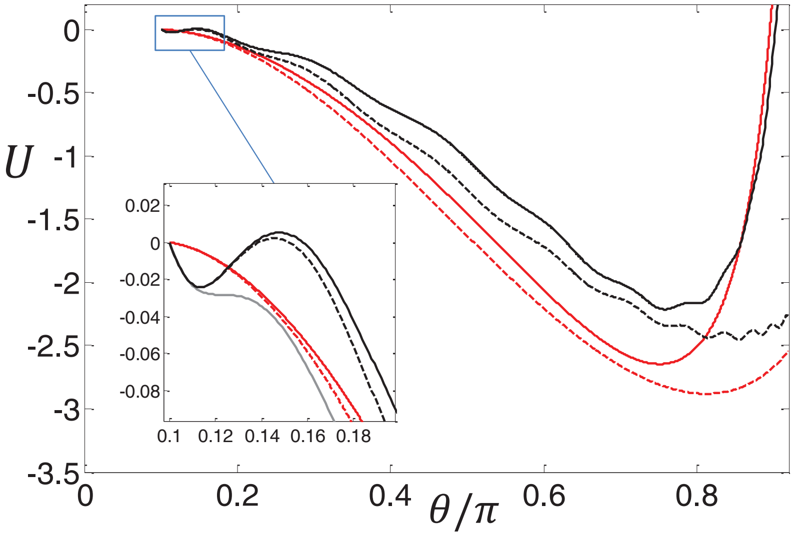

Figure 2.10: Total potential energy for curling as a function of $\theta$ for $R = R_0$ (the energy appears in units of $K_B R_0^2/a_0^2 \approx 10^5$ $k_B T$). Red lines are the trends associated with the analytical approximation of the model (dashed line is when the spectrin cortex is not considered). Black lines are the trends associated with the numerical solutions of the energies (dashed line is when the spectrin cortex is not considered). The parameters used in the curves are $a_0 = R_0/35$ (for the grey line in the zoom-inset $a_0 = R_0/43$), $R_0 = 3$ $\mu$m, $h_c = 10h = 50$ nm, $\gamma = 10$ pN, $G = 2.5 \times 10^{-6}$ N/m.

Returning to the analysis of curling nucleation, one might expect that the energy barrier shown in the zoom-inset of the Fig.2.10 can be overcome if the material flows from the cup to the rim (feeding), meaning that, it allows to increase the surface area with smaller density energy. However, as it can be observed in Fig.2.11, although the total energy effectively decreases when $R$ decreases, the local minimum moves progressively to smaller angles, which would cause the curling to move back to close the pore instead of progressing. In this sense, if the feeding is a plausible mechanism, the static equilibrium of a pore can not be reached in absence of a huge shear resistance. In a standard giant pore picture, the surface area of the cap is still much larger than the projected area of the pore, so a sealing would not modify appreciably the cap radius neither the bending energy; therefore, if the curling is early blocked, the system can always reach (with feeding) the lowest level of energy (without pores). This analysis seems in contradiction with a more refined theoretical treatment of opening-up vesicles with single and two holes [77], which indicates that for low line tension, and without shear resistance, stable holes in spherical vesicles can be obtained. However the numerical method used in [77] is based in a boundary condition in the cup that prevent feeding.

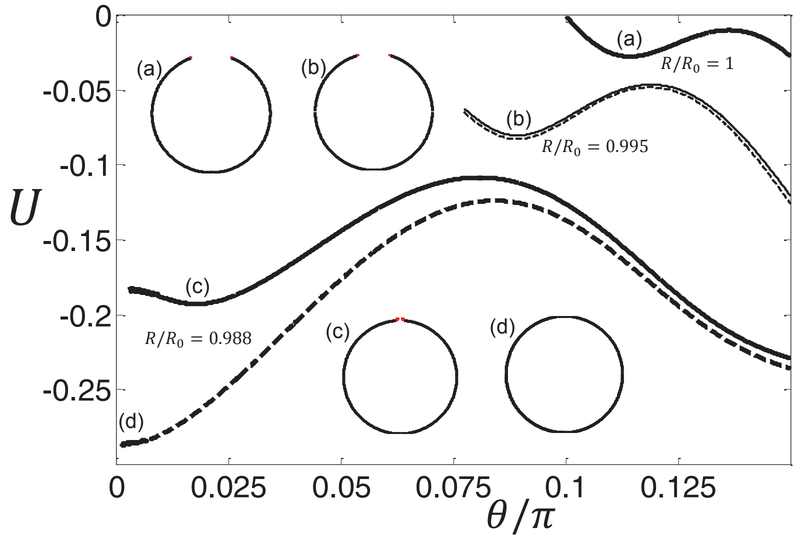

Figure 2.11: Numerical prediction of the total potential energy for curling as a function of $\theta$ for $a_0 = R_0/35$ and $\theta_0 = 0.1\pi$, but and different values of $R/R_0$. Dashed lines represents the numerical predictions without considering spectrin cortex. The parameters used in the curves are, $R_0 = 3$ $\mu$m, $h_c = h = 5$ nm, $\gamma = 10$ pN, $G = 2.5 \times 10^{-6}$ N/m. The inset shape profiles are the configurations associated with each local minimum of energy.

From these results one can conclude that the only way to get curling is by means of an increment of the spontaneous curvature. Using the numerical approach for the computation of the energies, we can localize the real critical normalized curvature $R/a_0^*$ for the curling nucleation. In Fig.2.12, the results, for the specific situation of $\theta_0 = \pi/10$, are presented as a function of the dimensionless parameter $\gamma R_0/K_B$; it shows that for typical values of RBCs ($\gamma R_0/K_B \approx 200$) the critical curvature is, between 20 and 30 percent, larger than the predicted by Eq.2.30.

## 2.4 Axisymmetric curling dynamics

In the geometry of curling described in the previous sections, we have been considering implicitly two independent dynamical modes of deformation: i) pure curling, where the angle $\theta$ changes for a constant radius $R$ of the cup and, ii) a feeding mechanism, where $R$ changes with a constant $\theta$. In this last part, we will calculate the dynamics of curling

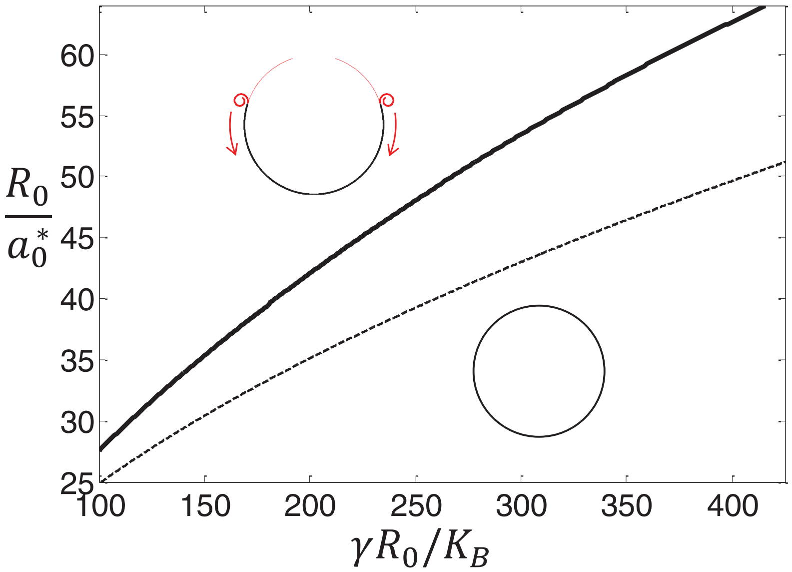

Figure 2.12: Phase diagram for curling nucleation considering $\theta_0 = 0.1\pi$. Solid lines gives the critical parameter for real curling, while dashed line represents the critical parameters for the fast closing of the pore (Eq.2.30).

based on a balance of energies present in the system together with the two possible sources of viscous dissipation, based respectively on the large scale flow around the curling rim and the membrane surface dissipation due to matter redistribution. Because of feeding, the time evolution of $\theta$ then couples to $R$. In the following, we put ourselves in the regime where curling can occur, *i.e.* where $1/a_0 > 1/a_0^*$.

### 2.4.1 Surface and bulk viscous dissipations

The viscous power dissipated in the system contains two contributions: a bulk term, $\Phi_b$, due to the movement of the membrane with respect to the background solvent, and a surface term, $\Phi_s$, due to axisymmetric lipid flow in the plane of the membrane.

We consider that the surface term is mainly due to axisymmetric lipid flow (or reorganization) neglecting interlayer dissipation. Generally, viscous dissipation in fluid dynamics, is given by the volume integration of the square of the components of the gradient of the velocity field, $V$ (see Eq.3.18 in the section 3.2.2 for a general expression of the density of viscous power dissipated in a liquid flow). In the case of lipid membranes, since the thickness is constant, and that we consider no interlayer dissipation, only the surface gradients of the velocity field will appear. In virtue of the axisymmetric geometry and the small inertia of the system, the velocity field can be represented only by the local meridian component, $V_s = d(s - s_0)/dt$, of the flow. Then, the gradient of the speed is equivalent to the time derivative of the tangential stretching ratio $\lambda = ds/ds_0$. Thus, denoting the membrane surface viscosity by $\eta_s$, the power dissipated per unit surface due to the redistribution of lipids is expressed by $\phi = 2\eta_s\dot{\lambda}^2$, where the overdot denotes a time derivative.

Considering the Eq.2.22 and Eq.2.24 we write in the rim

$$\dot{\lambda} = \dot{\lambda}_{rim} = \frac{R_0}{R}\left(\frac{\dot{R}}{R}\frac{\sin\theta}{\sin\psi_0} - \dot{\theta}\frac{\cos\theta}{\sin\psi_0}\right)$$

, and in the cap

$$\dot{\lambda} = \dot{\lambda}_{cap} = \left(\frac{R_0}{R}\right)^2 \frac{\dot{R}}{R}\frac{(1-\cos\psi_0)\sqrt{1+\cos\psi_0}}{\left[2-\left(\frac{R_0}{R}\right)^2(1-\cos\psi_0)\right]^{3/2}}$$

, and the total power dissipated during the redistribution of lipid becomes

$$\Phi_s = 4\pi\eta_s R_0^2\left\{\int_{\psi_0(s_c)}^{\pi-\theta_0}\dot{\lambda}_{rim}^2\sin\psi_0\cdot d\psi_0 + \int_0^{\psi_0(s_c)}\dot{\lambda}_{cap}^2\sin\psi_0\cdot d\psi_0\right\} \tag{2.32}$$

Moreover, the bulk term is approximated here by the Stokes friction due to motion of the rim with respect to the fixed cup. The rim is modeled by a cylinder of length $W = 2\pi R\sin\theta$ and radius $b$ moving at a speed $v = R\dot{\theta}$. The drag force on such a cylinder moving perpendicularly to its axis is [43]

$$f_D = \frac{4\pi^2\eta_0 W v}{\ln\left(\frac{3.7}{Re}\right)} \tag{2.33}$$

, where $\eta_0$ is the viscosity of the medium and $Re = bv\rho_0/\eta_0$ is the Reynolds number with $\rho_0$, the density of the medium (the $Re$ number is more appropriately introduced in the section 3.2.1). Because the curling occurs in an interval of around 250 ms, the characteristic value of $v$ is 3 $\mu$m/250 ms $\approx 10^{-5}$ m/s and then, with $b \sim a_0 \approx R_0/45$ we have $Re \sim 10^{-6}$ in water. Therefore, since 2.33 varies slowly with $Re$, the bulk power dissipated, $\Phi_b\mid_R = vf_D$, is taken

$$\Phi_b\mid_R \approx 0.3\pi^2\eta_0 R^3\dot{\theta}^2\sin\theta \tag{2.34}$$

. Here, the subscript $R$ means that the function is taken for $\dot{R} = 0$ describing the pure curling mode. From the Eq.2.32 we have also

$$\Phi_s\mid_R = 2\pi R_0^2\eta_s\mathcal{C}(\theta, R)\dot{\theta}^2$$

, where

$$\mathcal{C}(\theta,R)=\left(\frac{R_0}{R}\right)^2\left\{\cos^2\theta\cdot\ln\left[\frac{2(1+\cos\theta_0)-\left(\frac{R}{R_0}\right)^2(1+\cos\theta)(1+\cos\theta_0)}{\left(\frac{R}{R_0}\right)^2(1+\cos\theta)(1-\cos\theta_0)}\right]\right\}$$

In the case of the feeding dynamics, modifications on the cap radius induces a leak-out of the internal liquid. This leak-out will be considered the dominant contribution to $\Phi_b\mid_\theta$, where the subscript $\theta$ means that the function is taken for $\dot\theta=0$. This term can be estimated as follows. First, the volume of liquid in the cap is $\frac{2}{3}\pi R^3\left(1-\frac{1}{2}\cos\theta\right)(1+\cos\theta)^2$, then, the conservation of matter allows us to link the time derivative of the cap volume with the characteristic speed of leak-out $\langle v\rangle$:

$$2\pi\left(1-\frac{1}{2}\cos\theta\right)(1+\cos\theta)^2R^2\dot R=\pi R^2\sin^2\theta\,\langle v\rangle \tag{2.35}$$

, where the right side of the equations is the flow through the hole of radius $l=R\sin\theta$.

Second, the power dissipated can be established taking into account that the dominant gradient of the velocity field inside the cap is $\sim\langle v\rangle/l$. Therefore, using Eq.3.18 we construct

$$\Phi_b\mid_\theta\approx 2\eta\left(\frac{\langle v\rangle}{l}\right)^2\frac{2}{3}\pi R^3\left(1-\frac{1}{2}\cos\theta\right)(1+\cos\theta)^2$$

and replacing the value of $\langle v\rangle$, obtained from the volume conservation (Eq.2.35), we get

$$\Phi_b\mid_\theta\approx\frac{2\pi}{3}\frac{(2-\cos\theta)^3(1+\cos\theta)^6}{\sin^6\theta}\eta R\dot R^2 \tag{2.36}$$

Noteworthy, due to the geometric complexity of the problem, this dissipative terms is approximate, and an accurate geometric coefficient can be absorbed into the definition of the viscosity $\eta$. We also note that the viscosity of the fluid inside the cap, $\eta$, is different than the solvent viscosity, $\eta_0$. We assume that the solvent and the merozoites that are pushed forward behave as a colloidal suspension with a viscosity that may be as much as 10-100 times $\eta_0$, depending on the volume fraction of merozoites [78].

Directly from the Eq.2.32 we have

$$\Phi_s\mid_\theta=2\pi\eta_s\left[\mathcal{D}_{rim}(\theta,R)+\mathcal{D}_{cap}(\theta,R)\right]\dot R^2$$

Where

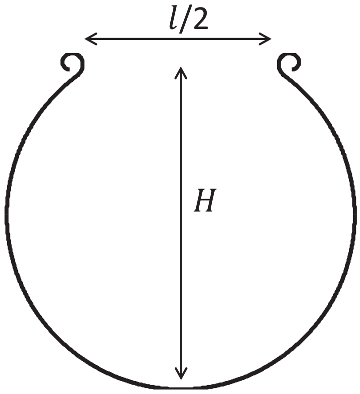

Figure 2.13: Characteristic lengths during the dynamics of the membrane: Cap depth,$H$, and pore radius $l$.

$$\mathcal{D}_{rim}(\theta,R)=\left(\frac{R_0}{R}\right)^4\left\{\sin^2\theta\cdot\ln\left[\frac{2(1+\cos\theta_0)-\left(\frac{R}{R_0}\right)^2(1+\cos\theta)(1+\cos\theta_0)}{\left(\frac{R}{R_0}\right)^2(1+\cos\theta)(1-\cos\theta_0)}\right]\right\}$$

and

$$\mathcal{D}_{cap}(\theta,R)=2\left\{\ln\left[\frac{1}{2}-\frac{\cos\theta}{2}\right]+\frac{2+2\left[\left(\frac{R_0}{R}\right)^2-2\right]\cos\theta}{(1-\cos\theta)^2}+\frac{1}{2}\left(\frac{R_0}{R}\right)^2-\frac{3}{2}\right\}$$

### 2.4.2 Dynamical equations

The dynamical equations of motion of the rim can then be simply obtained by writing the balance of energy in the two modes of deformation.

For pure curling, one obtains

$$\dot{\theta}\frac{\partial U}{\partial\theta}+\Phi_b\mid_R+\Phi_s\mid_R=0 \tag{2.37}$$

Then, directly from Eq.2.37, we obtain the first dynamical equation in the problem, relating the angular speed variation to R:

$$\dot{\theta}=f(\theta,R)=\frac{-\frac{\partial U}{\partial\theta}}{2\pi R_0^2\eta_0\left[\frac{1}{2}R\left(\frac{R}{R_0}\right)^2\sin\theta+\frac{\eta_s}{\eta_0}\mathcal{C}\right]} \tag{2.38}$$

Similarly, in the case of the feeding dynamics, we have

$$\dot{R}\frac{\partial U}{\partial R} + \Phi_b \mid_\theta + \Phi_s \mid_\theta = 0 \tag{2.39}$$

Thanks to Eq.2.39, the time derivative of the cap radius can be expressed as a function of the angle by

$$\dot{R} = g\left(\theta, R\right) = \frac{-\frac{\partial U}{\partial R}}{2\pi\eta\left\{\frac{(2-\cos\theta)^3(1+\cos\theta)^6}{3\sin^6\theta}R + \frac{\eta_s}{\eta}\left(\mathcal{D}_{rim} + \mathcal{D}_{cap}\right)\right\}} \tag{2.40}$$

This coupled dynamical system of equations ( Eq.2.38 and Eq.2.40) represent a second order non-linear differential equation that can be solved with standard techniques [72].

### 2.4.3 Results

The figure 2.14 illustrates the solutions $\theta(t)$ and $R(t)$ we obtain between $\theta = \theta_0 = 0.1\pi$ and $\theta = 0.7\pi$. It reveals in particular that feeding allows to a dynamical change in the cap radius which is quite sensitive to the surface viscosity. Indeed, the cap radius decreases with time until it reaches a minimum for relatively high $\theta$; after that, the angle $\theta$ continues to increase and $R$ grows, causing a relative flattening of the cap. The time scale of the process depends strongly on $\eta_s$. In fact, if one neglects the surface viscosity, the characteristic time associated with the dynamics is less than a millisecond for a spontaneus curvature, $1/a_0 = 45/R_0$, relatively close to the critical curvature of curling (see first trend from the left in Fig.2.14). This time is too small to explain the curling dynamics observed in Abkarian et al. [1] where the full curling process takes aproximately two hundred milliseconds. Moreover, comparison of our model with membrane dynamics during parasite egress from RBCs suggests that membrane viscous stresses may be the dominant dissipative mode. Indeed, fitting our experimental data for the cap depth, $H = R(1+\cos\theta)$ (see Fig.2.13), with our model, we obtain $1/a_0 = 45/R_0$ and $\eta_s/\eta_0 = 650$ $\mu$m (see Fig.2.15). The value of the spontaneous curvature is consistent with measurements [1]. We have taken $h_c = 50$ nm $= 10h$ as the standard thickness compressibility of a red cell membrane in situ [32]. Where $h$ is the only the lipid membrane thickness. In addition, in obtaining our fit parameters, we have taken $\eta \approx 10\eta_0$. This choice reflects the contribution of the merozoites to the bulk viscous dissipation during leak-out. Nonetheless, the values of $a_0/R$ and $\eta_s/\eta_0$ are largely insensitive to $\eta$: a 50% change in $\eta$ results in changes in $a_0/R$ and $\eta_s/\eta_0$ of $< 1$ %. Finally, to avoid the proliferation of too many fit parameters, we have fixed those, such as $K_B$, $h_c$, and $\gamma$, that are reasonably well known, and have only kept as trial parameters those related to the RBC membrane that are susceptible to modification by the parasites, i.e., $a_0/R$ and $\eta_s/\eta_0$.

From Fig.2.15, it is apparent that agreement between our theoretical model and the

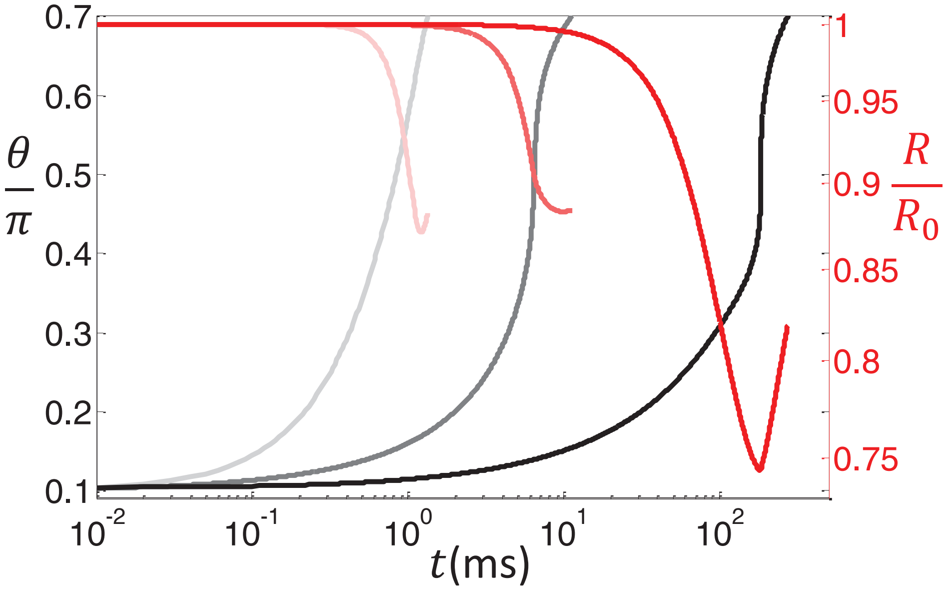

Figure 2.14: Curling dynamics during parasite egress. The pore openong angle, $\theta$, and normalized cap radius, $R/R_0$, versus $t$. They are shown for different values of the ratio of surface to bulk viscosities, $\eta_s/\eta_0$. From lef to rigth: $\eta_s/\eta_0 = 0$ $\mu$m; 50 $\mu$m and 650 $\mu$m. The fixed parameters are: $R_0/a_0 = 45$, $R_0 = 3$ $\mu$m, $h_c = 10h$, $\eta = 10\eta_0$, $\gamma = 12.6$ pN and $K_B = 2.0 \times 10^{-19}$ Nm.

experimental values of the cap depth and cap radius breaks down at long times, at which they rapidly passes through zero and changes sign. In fact, Abkarian and co-workers [1] have shown that the final step of parasite egress from RBCs involves an eversion of the membrane cap, leading to dispersal of the last parasites. Similar eversion behavior was also observed in the last stages of polymersome bursting [49].

## 2.5 Discussion

An unresolved problem in the study of malaria infection is the mechanism by which parasites exit red blood cells, thereby transmitting the disease in the bloodstream. Motivated by recent work on the transmission mechanism, and inspired by modeling of bursting polymersomes, we have developed a theoretical description of the membrane energetics and dynamics that enable parasite egress from infected RBCs. Starting from the experimental observation that parasites induce a spontaneous curvature in the RBC plasma membrane before egress, driving pore formation and outward curling of the membrane, our model makes qualitative and quantitative predictions for the membrane dynamics leading to egress.

The main theoretical finding of our work is that the RBC membrane dynamics during parasite can be considered as the superposition of two types of membrane movement: 1), *Pure curling*, where the membrane bend on itsef, varing $\theta$, but keeping the radius of the cup constant; and 2), *Feeding*, where the radius of the cap changes with $\theta$ constant. These two coupled modes of deformation stem from the axisymmetric character of the RBC membrane, implying a non monotonic dependence of the rim elastic energy on the pore opening angle. In order to explain the membrane dynamics involved in parasite egress from RBCs, observed experimentally, the surface dissipation must dominates bulk dissipation. By fitting our model to experimental data, we found that $R_0/a_0 \approx 45$, in agreement with earlier findings [1]. In addition, we found that the length scale below which surface dissipation dominates bulk dissipation, $\eta_s/\eta_0$, is on the order of 1 mm. Interestingly, this value is much larger than one would expect by naively assuming a value of $\eta_s = 10^{-9}$ Pa·s·m (yielding $\eta_s/\eta_0 = 1$ $\mu$m for $\eta_0 = 10^{-3}$ Pa·s), typical for a lipid membrane [20]. The membrane viscosity of malaria-infected RBCs is not known; however, our fit value is comparable to viscoelastic relaxation measurements on healthy RBCs, yielding $\eta_s = 10^{-6}$ Pa·s·m [34]. The dynamical approach developed here is based on

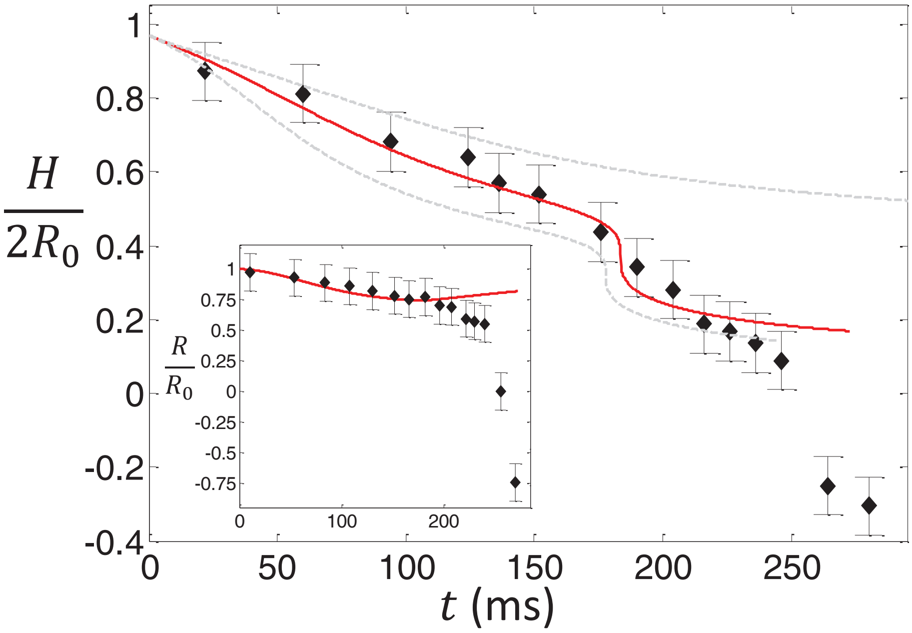

Figure 2.15: Model fitting to experimental results. The normalized cap depth , $H/2R_0$, versus $t$ during parasite egress from RBCs. Data from Abkarian et al.[1] (◆) is fitted with the model developed in this work (red lines). Deviation between the data and the model is expected for small $h$. Inset: Normalized cap radius,$R/R_0$, versus $t$ for the same experiment. The fit parameters are: $\eta_s/\eta_0 = 650$ $\mu$m and $R_0/a_0 = 45$. The other fixed parameters are: $R_0 = 3$ $\mu$m, $h_c = 10h$, $\eta = 10\eta_0$, $\gamma = 12.6$ pN and $K_B = 2.0 \times 10^{-19}$ Nm. The grey dashed lines, are for $h_c = 20h$ (upper line) and $h_c = h$.

the wide separation of two length scales: the RBC radius, $R_0$, and the inverse spontaneous curvature, $1/a_0$. The inequality $a_0/R_0 \ll 1$ allows to an analytical approximation for the potential energies which are used to express the gradients $\frac{\partial U}{\partial \theta}$ and $\frac{\partial U}{\partial R}$ in the dynamical equations ( Eq.2.38 and Eq.2.40). However, with the approximations, the cycloidal nature of the curling movement is neglected, and it cannot predict the critical curvature of curling, $1/a_0^*$, accurately. Also, for large $h_c$, the analytical approximation shows an important deviation with respect to the different numerical computations of the energies in the problem (without approximations), that can reach even a 30% of difference. An alternative approach for the performed numerical solution of the second order nonlinear differential equation (represented by Eq.2.38 and Eq.2.40), would be to attempt to use, for the energy gradient computations, numerical trends of the potential energies (instead of the analytical approximation), but the solving numerical method of the resultant system, would require a significant change that could not be completed at the last stage of the thesis.

It is important to note that the parameter $h_c = 10h$ used for the fitting of the model is, in some sense, arbitrary and represented a minimum value. This choice does not consider any contribution due other steric elements that are present on an iRBC membrane or/and any hydrodynamic forces that can be large. Actually, for the later, if we take in consideration the lubrication flow between successive layers in the rim, using Eq.3.22, the minimum time for the squeezing of the layers is estimated to be $10^7 \times \frac{\eta_0 h^3}{K_B} \approx 100$ ms. This suggests that the liquid trapped between the layers in the rim, can not escape during the time of curling, therefore $h_c$ must be larger than the thickness compressibility. In Fig.2.15, the grey dashed lines are the theoretical predictions when the parameter $h_c$ is modified. For $h_c = h$ the trend does not vary a lot respect to the principal one (of the fit), while for $h_c = 20h$ (upper dashed line), the characteristic time of curve is significantly increased (the fit with $h_c = 20h$ gives a reduction of the value of $\eta_s$ in approximately 30% respect to the fit obtained with $h_c = 10h$). Thus, a reliable measurement of $\eta$ through the fitting of the proposed model, can be done only if $h_c$ is properly estimated in the context of the fluid-dynamics. Some important elements of fluid dynamics coupled to curling are clarified in the next chapters, where the curling dynamics in macroscopic ribbons is studied experimentally.

## 2.6 Conclusions

As a result of the three-dimensional axisymmetric nature of the problem, the membrane dynamics can be separated in two independent modes of elastic-energy release: 1), at short times after pore opening, the free edge of the membrane curls into a toroidal rim attached to a membrane cap of roughly fixed radius; and 2), at longer times, the rim is fixed, and lipids in the cap flow into the rim. The model is compared with the experimental data of

Abkarian and co-workers [1] and an estimate of the induced spontaneous curvature and the membrane viscosity, which control the timescale of parasite release, are obtained.

Our model integrate different aspect of membrane dynamics and propose a fitting procedure to extract $\kappa_0$ from dynamical parameters. Importantly, the measurement of spontaneous curvature which is biologically relevant in the case of Malaria is a real experimental challenge and there are actually no direct and simple experimental techniques allowing the extraction of $\kappa_0$. Therefore, the development of realistic models capable to capture the dynamics of pore opening during curling are highly valuable to understand the biological origin of curling.

# Chapter 3

# Mechanics of naturally curved ribbons

---

In this chapter, we introduce some basic mechanical and elaso-viscous ingredients necessary to understand the following two chapters about the curling dynamics of ribbons at varying Reynolds number in media as different as air, water and viscous Silicon oils. Moreover, we discuss the specific mechanical behaviors of ribbons bearing a unidirectional spontaneous (natural) curvature along with their geometric and mechanical characteristics relevant for the experiments we perform later.

## 3.1 Introduction to bending elasticity of ribbons

### 3.1.1 Bending of thin solid materials

In a solid system, small deformations around an arbitrary point $\mathbf{r}$ of the body, are quantified by the local strains ($\varepsilon_1$, $\varepsilon_2$, $\varepsilon_3$) along the local principal axes ($\hat{e}_1$, $\hat{e}_2$, $\hat{e}_3$) which are, before and after deformation, mutually perpendicular. When the material is thin enough, the local unitary vector $\hat{n}$, normal to the surface, is always parallel to one of the principal axes (see Fig.1.4A). By convention we will write $\hat{e}_3 = \hat{n}$. A general strain $\varepsilon_i$ can be interpreted as the normalized linear stretching of an infinitesimal spring placed parallel to the direction $\hat{e}_i$; then $\varepsilon_i = (dr'_i - dr_i)/dr_i$, where $dr_i$ is the infinitesimal distance along the $\hat{e}_i$ axis in the resting state (or natural length of the spring) and $dr'_i$ is the infinitesimal distance after deformation (or stretched length of the spring). Actually, the essence of the solid response of a system can be always captured by an arrangement of springs as shown in Fig.1.4B.

The degrees of freedom of the intrinsic configuration of matter leads to identify two independent linear modes of local deformation: a pure homogeneous dilation (or pure compression) where $\varepsilon_1 = \varepsilon_2 = \varepsilon_3$ and a pure inhomogeneous dilation (or pure shear) where $\varepsilon_1 + \varepsilon_2 + \varepsilon_3 = 0$ (without varying the infinitesimal amount of volume). The pure compression and pure shear part of an arbitrary deformation are characterized respectively by the relative variation of volume $\varepsilon_1 + \varepsilon_2 + \varepsilon_3$ and $\varepsilon_1^2 + \varepsilon_2^2 + \varepsilon_3^2 - \frac{1}{3}(\varepsilon_1 + \varepsilon_2 + \varepsilon_3)^2$, which reflects the contribution of the inhomogeneous dilation mode, in the increment of surface area in the infinitesimal enclosed volume (see appendix A.1). A linear expansion of these two quantities allow us to write the elastic energy density (energy per unit volume) [44]:

$$\mathcal{F}(\mathbf{r}) = \frac{1}{2}K\left(\varepsilon_1 + \varepsilon_2 + \varepsilon_3\right)^2 + G\left[\varepsilon_1^2 + \varepsilon_2^2 + \varepsilon_3^2 - \frac{1}{3}(\varepsilon_1 + \varepsilon_2 + \varepsilon_3)^2\right] \tag{3.1}$$

, where $G$ and $K$ are the shear and compression modulus of the material. When the system is very thin, it avoids any tensile stresses normal to the surface, then the strain $\varepsilon_3$ in the normal direction, is simply determined by minimization of $\mathcal{F}$. Thus, introducing the Young modulus $E = \frac{9KG}{3K+G}$ and the Poisson's ratio $\nu = \frac{1}{2}\frac{(3K-2G)}{(3K+G)}$, we obtain $\frac{\partial \mathcal{F}}{\partial \varepsilon_3} = 0 \Leftrightarrow \varepsilon_3 = -\frac{\nu}{1-\nu}(\varepsilon_1 + \varepsilon_2)$ and the elastic energy density rewrites

$$\mathcal{F}(\mathbf{r}) = \frac{E}{2(1+\nu^2)}\left\{(\varepsilon_1 + \varepsilon_2)^2 - 2(1-\nu)\varepsilon_1\varepsilon_2\right\} \tag{3.2}$$

The general relation between the elastic energy and an arbitrary curvature configuration in the body, can be obtained from Eq.3.2 using a variational approach with respect to the strains of the centre surface of the material; the result is condensed in a set of partial differential equations known as Föppl-von Kármán equations [47]. These equations are highly nonlinear and complex. The preponderant complications, lie in the fact that the curvature variation usually involves a nontrivial modification in the metric of the surfaces. A special case appears when the bending deformation is characterized by a zero Gaussian curvature before and after deformation (planar bending). In this case, the metric does not change [74], one of the strains is always zero and the others become proportional to the principal curvature $\kappa$ of the bending. Then, the elastic energy per unit surface is basically $\frac{1}{2}B\kappa^2$, where $B \sim Eh^3$ is the bending stiffness of the material and $h$ is the thickness qualifying straight ribbons as elastic beams.

### 3.1.2 Curvature-Strain coupling for elastic Beams

The resistance to bending of beams, comes from the simple fact that two parallel lines in the material cannot be curved simultaneously without altering their initial lengths. This idea has been illustrated in the Fig.3.1, where a specific infinitesimal portion of the longitudinal profile of a rectangular beam (of thickness $h$), is considered before and after an arbitrary flexion. The centerline of the profile (red dashed line in Fig.3.1) is used as a reference to write the position of any point in the material. Thus, each point in

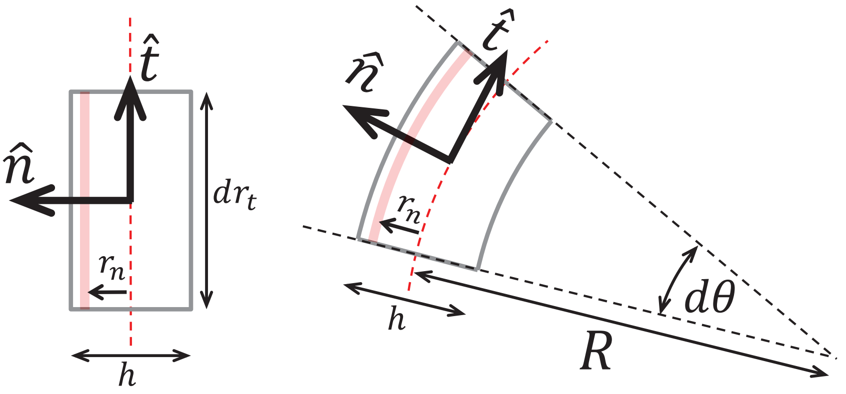

Figure 3.1: Resting state (left) and bending state associated with an infinitesimal portion of the profile of a rectangular beam of thickness $h$.

the bending plane, is represented by a couple of numbers $(r_t,\ r_n)$, where $r_t$ is the arc length position of the centerline (locally, $r_t$ grows along the tangent $\hat{t}$ direction) and $r_n$ is the distance, from the centerline, to any point in the local normal direction $\hat{n}$. Since the tangential and normal directions are always perpendicular, the principal strain axes in any point of the body, coincides with the Frenet frame $(\hat{t},\ \hat{n},\ \hat{b})$, where $\hat{b} = \hat{t} \times \hat{n}$ is the unitary binormal vector. The strain $\varepsilon_t$ along the tangential direction depends on the position $r_n$ and can be expressed as a simple proportion between the radius of curvature $R$ and the angular variation $d\theta$ of the flexion:

$$\varepsilon_t = \frac{dr'_t - dr_t}{dr_t} = \frac{(R - r_n)d\theta - Rd\theta}{Rd\theta} = \kappa r_n \tag{3.3}$$

, where $\kappa = 1/R$ is the local curvature and the centerline is supposed “free of strain".

For slender beams, the width $W$ is comparable with the thickness. Then, as well as in the normal direction, the tensile stresses along the binormal direction are negligible. Therefore, $\varepsilon_b$ is defined by simple minimization of Eq.3.2 (with $\varepsilon_1 \to \varepsilon_t$ and $\varepsilon_2 \to \varepsilon_b$):

$$\frac{\partial \mathcal{F}_S}{\partial \varepsilon_b} = 0 \Leftrightarrow \varepsilon_b = -\nu\varepsilon_t \tag{3.4}$$

The total bending energy $U_B$ of a rectangular beam of width $W$, thickness $h$ and length $L$ is given by the integral of the density function $\mathcal{F}_S(\mathbf{r})$ on the whole volume. Therefore,

$$\frac{U_B}{W} = \frac{1}{2}B\int_0^L \kappa^2 dr_t \tag{3.5}$$

, where $B = \frac{Eh^3}{12}$ is the bending stiffness. One could think that this relation is independent on the width $W$; however, when $W$ is very large, the tensions along the binormal directions cannot be ignored. For instance, whether $W/h \gg 1$ and, with some indulgence, Eq.3.3 and Eq.3.4 are still correct, we should expect a parabolic like deformation of the cross-section characterized by a curvature $\kappa_\perp = -\nu\kappa$. Nevertheless, a curved cross-section would induce an increment of the projected thickness of the profile in the order of $\sim \kappa_\perp W^2$ which is easily larger than the natural thickness. Then, the effective bending stiffness, should increase dramatically and, a hypothetical “free of strain" line, located in the centre surface of the beam, would not be possible. In this scenario $\varepsilon_b = 0$ is energetically much more favorable than the previous $\varepsilon_b = -\nu\varepsilon_t$. Thus, a pure bending deformation (where the strain elements are proportional to $\kappa r_n$) in a wide enough beam, has sense only when the Gaussian curvature is zero.

The restriction $\varepsilon_b = 0$ in beams, has the effect to increase the amount of energy density in a factor $\frac{1}{1-\nu^2}$ with respect to the result of Eq.3.5. Then, when $W/h \gg 1$ the total elastic energy can be written in the same way than before (Eq.3.5) but with $B = \frac{Eh^3}{12(1-\nu^2)}$ which is the typical bending stiffness of a solid sheet.

Until now, the planar bending deformations have been treated for materials whose resting state coincides with a flat configuration (where $\kappa = 0$). However, in the curling dynamics of ribbons studied in the following chapters, the resting state corresponds to a cylindrical shape with a specific curvature. For the general situation of planar bending of naturally curved materials (with natural curvature $\kappa_0$), the strain of the Eq.3.3 must be written $\varepsilon_t = (\kappa - \kappa_0) r_n$, and therefore, all the elastic equations can be used with the simple transformation $\kappa \rightarrow (\kappa - \kappa_0)$.

### 3.1.3 Dynamics of flexural beams

Regardless of the aspect ratio of the cross-section of the rectangular beam, the local tangential stress due to bending $\sigma = \frac{\partial \mathcal{F}_S}{\partial \varepsilon_t}$ (along the tangential direction) is always an odd function of $r_n$; hence, the pure bending force in an arbitrary cross-section $\int_{-W/2}^{W/2}\int_{-h/2}^{h/2} \sigma dr_n dr_b$ is patently zero. However, the resultant torque $\mathbf{M}(r_t)$ is not. Actually,

$$\frac{\mathbf{M}(r_t)}{W} = (\hat{n} \times \hat{t}) \int_{-h/2}^{h/2} \sigma r_n dr_n = (\hat{n} \times \hat{t}) B\kappa \tag{3.6}$$

The mechanical equilibrium of the beam portion between two cross-sections separated by an infinitesimal distance $ds$ (as is shown in the sketch in Fig.3.2) can be obtained by using the hypothesis that the state of stress of any cross-section can be characterized by a resultant elastic force $\mathbf{F}(r_t)$ and the resultant elastic torque $\mathbf{M}(r_t)$. We suppose no tortion in the system, so the configuration of the beam is completly defined in the plane where the centerline resides.

If the vectorial position of the considered portion is denoted by $\mathbf{r}$, the equilibrium of

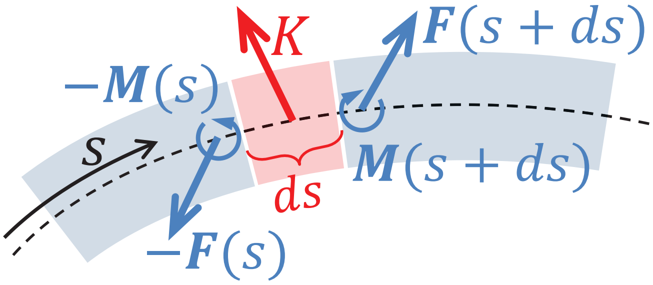

Figure 3.2: Sketch of the relevant forces and torques in the mechanical equilibrium of any infinitesimal portion of a beam.

forces gives

$$\frac{\partial \mathbf{F}}{\partial s} + \mathbf{K} = \varrho \ddot{\mathbf{r}} \tag{3.7}$$

, where $\mathbf{K}$ is an arbitrary external force per unit length, $\varrho\ddot{\mathbf{r}}$ is the inertial force per unit length of the infinitesimal portion (the overdots represent time derivatives and $\varrho$ is the linear mass density) and the coordinate $r_n$ is denoted explicity by the arc length symbol $s$. Moreover, the torque equilibrium gives

$$\frac{\partial \mathbf{M}}{\partial s} + \hat{t} \times \mathbf{F} = (\hat{n} \times \hat{t})\frac{\varrho h^2}{12}\dot{\omega} \tag{3.8}$$

, where $\omega$ is the local angular speed, so the rigth side of the equation is exactly the time derivative of the angular momemtum (per unit length) of the infinitesimal portion.

By definition, the curvature represents a spatial derivative of the normal or tangential unitary vectors:

$$\kappa = \hat{t} \cdot \frac{d\hat{n}}{ds} = -\hat{n} \cdot \frac{d\hat{t}}{ds}$$

. Similarly, the angular speed is linked with the time derivative of the same unitary vectors.

$$\omega = \hat{t} \cdot \dot{\hat{n}} = -\hat{n} \cdot \dot{\hat{t}}$$

. In consequence, the angular speed is related with the curvature in the way

$$\frac{d\omega}{ds} = \dot{\kappa} \tag{3.9}$$

, and taking advantage of $\hat{t} = \frac{d\mathbf{r}}{ds}$, the coupling between the acceleration and the curvature can be obtained through

$$\frac{d\ddot{\mathbf{r}}}{ds} = \ddot{\hat{t}} = -(\hat{t}\omega^2 + \hat{n}\dot{\omega}) \tag{3.10}$$

Thanks to these kinematic relations (Eq.3.9 and Eq.3.10), the equilibrium equations (Eq.3.7 and Eq.3.8) can be expressed only in terms of partial derivatives or integrals of the curvature. In the limit of small deflections, the mathematical description is much simpler. Actually, in absence of external forces, the combination of the different equations gives (see appendix A.2)

$$BW\frac{\partial^4\kappa}{\partial s^4} - \varrho\ddot{\kappa} = \frac{\varrho h}{12}\frac{\partial^2\ddot{\kappa}}{\partial s^2} \tag{3.11}$$

, which is the famous Kirchhoff equation for small deflexion. It has solutions in the form $\kappa(s,t) = f(\zeta)$, where the self-similarity variable is $\zeta \sim s/\sqrt{t}$ [6, 2]. This reflects the despersive nature of Eq.3.11, where a progresive wave with constant velocity, $s \sim t$, is incompatible, but instead a self similar solution $s \sim \sqrt{t}$ appears.

## 3.2 Introduction to Elasto-Viscous Interactions

The dynamic of curling (or elastic bending) of a specific material are, in general, accompanied by dissipative processes due to the inherent viscocity in the external medium or in the material itself. These processes give rise to dissipative forces that can even control the bending modes.

### 3.2.1 Planar Bending coupled to Drag

In curling dynamics the material is transported in a well defined curled body of characteristic frontal size $D$, the movement produces a large scale fluid stream, which exerts a resultant force against the curling propagation. The force $F_d$ on the body along the stream axis is called *drag* and is defined in term of the drag coefficient $C_d$:

$$C_d = \frac{F_d}{\frac{1}{2}\rho_f V^2 A} \tag{3.12}$$

, where $A$ is the characteristic area of the body (*frontal area* for thick bodies such as cylinders, or *planform area* for flat bodies), $V$ is the relative free-stream velocity (or velocity of the body with respect to the fluid, at rest, at infinity) and $\rho_f$ is the density of the fluid. In consideration to a hypothetical external work $F_d X$ necessary to maintain, along a distance $X$, a constant travelling speed $V$ of the body (or equivalently constant stream of the fluid), the power dissipated by the drag is simply computed by $F_d\frac{dX}{dt} = F_d V$. The ratio between kinetic energy in the fluid and the dissipated energy associated with the drag is the Reynolds number $Re$ and is based upon the velocity $V$, the characteristic length $D$ of the body and the dynamic viscocity $\eta_0$.

$$Re = \frac{\rho_f V D}{\eta_0} \tag{3.13}$$

There is at the present no satisfactory theory for the forces on an arbitrary geometry immersed in a stream flowing at an arbitrary $Re$ [82]. However, there exist two aspects that seem to be general. First, for the same body, the experimental values of $C_d$ are approximately constant in an extensive range of high $Re$ (Rayleigh drag), for instance, when $10^2 < Re < 10^5$, the two-dimensional flow past a cylinder shows $C_d \approx 1$ (for higher $Re$ the surfaces roughness of the body induces turbulence and a strong reduction in the observable $C_d$). Second, for low Reynolds number $Re \lesssim 10^{-1}$, the inertia of the fluid is neglected, the hydrodynamic equations are simplified and $C_d \backsim 1/Re$ can be obtained analytically (Stokes's law) with a good experimental agreement [80].

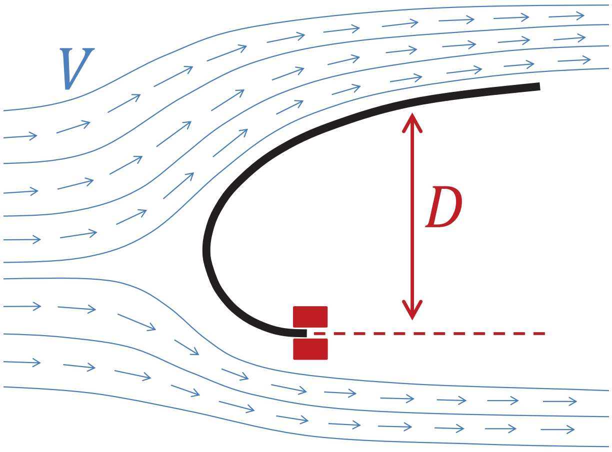

Figure 3.3: Scheme of the bending response of an embedded rod, under the drag associated with a passing flow with velocity $\mathbf{V}$.

The bending response of the material under such drag forces, can be studied as sketched in Fig.3.3 where an embedded sheet is deformed by a stream of fluid. The effective length of deflection $D$ is estimated after comparing the elastic torque of the beam $\sim \frac{BW}{D}$ (see Eq.3.6) with the drag torque $\sim F_d D = C_d \rho_f V^2 W D^2$. Then, for high Reynolds number (in the range where $C_d$ is approximately constant), we have $D \sim L_d$, where $L_d = \left(\frac{B}{\rho_f V^2}\right)^{1/3}$ is a mechanical parameter (with unit of length) that gives the magnitude of the elastic deformation due to drag. Actually $D/L_d \sim C_y^{1/3}$, where $C_y = \rho_f V^2 D^3/B$ is the Cauchy number, the dimensionless ratio of aerodynamic Rayleigh force $\rho_f V^2 W D$ to bending force $BW/D^2$ [8].

For low $Re$, the situation is different. Since $C_d \sim 1/Re$, the drag torque is $F_d \sim V D \eta_0 W$, then $D \sim L_v = \sqrt{\frac{B}{V\eta_0}}$ which is the elasto-viscous length.

### 3.2.2 Planar Bending coupled to lubrication dynamics

Because curling represents a continuous bending of the material on itself, it induces the presence of a fluid film whose draining will dissipate energy (squeezing) that, depending on the *Re*, can be dominant (chapter 5). In this situation, the dissipated energy (and forces associated) arise on much smaller scale than the typical length of drag studied before, and they can be approached in the context of lubrication dynamics.

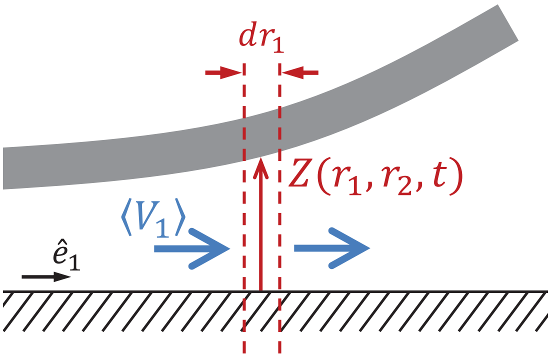

Figure 3.4: Diagram for the generic description of thin film flows.

In order to see how the theoretical treatment of lubrication in soft interfaces arises, let's consider the flow of a liquid film confined between a solid sheet and a solid substrate as is shown in Fig.3.4. The local thickness of the fluid film in any position ($r_1$, $r_2$) i-with respect to the surface of the substrate (in Fig.3.4, $r_2$ changes in the direction normal to the paper) is characterized by the function $Z(r_1, r_2)$. When $Z(r_1, r_2)$ is small compared with any other scale, the flow is basically parallel to the local tangential plane of the substrate, then the velocity field $\mathbf{V} = \mathbf{V}(r_1, r_2, r_3, t)$ of the fluid can be written $\mathbf{V} = V_1\hat{e}_1 + V_2\hat{e}_2$, where $V_1 = V_1(r_1, r_2, r_3, t)$ and $V_2 = V_2(r_1, r_2, r_3, t)$ are the scalar components of the field along the two perpendicular directions ($\hat{e}_1$, $\hat{e}_2$). The flow of matter per unit width (volume transported per unit time divided by the cross length of the flow) in the directions $\hat{e}_1$ and $\hat{e}_2$ are respectively $Q_1(r_1, r_2) = \langle V_1 \rangle\, Z(r_1, r_2)$ and $Q_2(r_1, r_2) = \langle V_2 \rangle\, Z(r_1, r_2)$, where $\langle V_1 \rangle$ and $\langle V_2 \rangle$ are the averages values of the components of the field in the local thickness $Z(r_1, r_2)$ of the fluid.

From the mass balance

$$\frac{\partial}{\partial t} Z(r_1, r_2) + \frac{\partial}{\partial r_1} Q_1(r_1, r_2) + \frac{\partial}{\partial r_2} Q_2(r_1, r_2) = 0 \tag{3.14}$$

The velocity field of an incompressible Newtonian fluid is related with the field of pressure $P$ by means of the Stokes equations,

$$\bigtriangledown P = \eta_0 \bigtriangledown^2 \mathbf{V} \tag{3.15}$$

, where $\eta_0$ is the dynamic viscosity. Since $Z$ is small and the fluid is confined with solid boundaries, the $r_3$-derivatives dominate in the description of the flow. Then $\bigtriangledown^2\mathbf{V} = \hat{e}_1\frac{\partial^2 V_1}{\partial r_3^2} + \hat{e}_2\frac{\partial^2 V_2}{\partial r_3^2}$ and Eq.3.15 gives the three scalar equations: $\frac{\partial P}{\partial r_1} = \eta_0\frac{\partial^2 V_1}{\partial r_3^2}$, $\frac{\partial P}{\partial r_2} = \eta_0\frac{\partial^2 V_2}{\partial r_3^2}$ and $\frac{\partial P}{\partial r_3} = 0$. From the last term, one can deduce that $P = P(r_1, r_2)$ and from the other terms:

$$V_1 = \frac{1}{2\eta_0}\left(\frac{\partial P}{\partial r_1}\right)\left(r_3^2 - Zr_3\right) + \frac{ur_3}{Z} \Rightarrow \langle V_1\rangle = -\frac{Z^2}{12\eta_0}\left(\frac{\partial P}{\partial r_1}\right) + \frac{1}{2}u \tag{3.16}$$

$$V_2 = \frac{1}{2\eta_0}\left(\frac{\partial P}{\partial r_2}\right)\left(r_3^2 - Zr_3\right) + \frac{vr_3}{Z} \Rightarrow \langle V_2\rangle = -\frac{Z^2}{12\eta_0}\left(\frac{\partial P}{\partial r_2}\right) + \frac{1}{2}v \tag{3.17}$$

, where $u = V_1(r_3 = Z)$ and $v = V_2(r_3 = Z)$ are the relative horizontal components of the instantaneous velocity of the solid sheet respectively to the substrate. Note that the averages of the velocities have a term proportional to the variation of the pressure in the direction of the flow, this term is equivalent to a Darcy's flow with permeability $Z^2/12$. The other term, is the drag flow caused by the horizontal displacement of the sheet respectively to the substrate. Moreover, the power dissipated $\phi$ per unit volume is proportional to the square of the spatial derivatives of the components of the velocity field, more precisely [43]:

$$\phi = 2\eta_0\sum_{i,k}\left(\frac{\partial V_i}{\partial r_k}\right)^2 \tag{3.18}$$

Since during lubrication the $r_3$-derivatives dominate, these terms also dominate in the dissipation, therefore

$$\phi = 2\eta_0\left[\left(\frac{\partial V_1}{\partial r_3}\right)^2 + \left(\frac{\partial V_2}{\partial r_3}\right)^2\right] \tag{3.19}$$

Combining Eq.3.16 and Eq.3.17 with Eq.3.14, the lubrication equation is obtained

$$\frac{1}{12\eta_0}\left[\frac{\partial}{\partial r_1}\left(Z^3\frac{\partial P}{\partial r_1}\right) + \frac{\partial}{\partial r_2}\left(Z^3\frac{\partial P}{\partial r_2}\right)\right] = \frac{\partial Z}{\partial t} + \frac{1}{2}\left[\frac{\partial}{\partial r_1}(Zu) + \frac{\partial}{\partial r_2}(Zv)\right] \tag{3.20}$$

For planar bending deformations and $Z = Z(r_1)$, the local elastic pressure on the fluid film can be written $B\frac{\partial^4 Z}{\partial r_1^4}$ (see appendix A.3). By virtue of the action-reaction principle, we get $P = P(r_1) = B\frac{\partial^4 Z}{\partial r_1^4}$ and the flow is only in the direction $\hat{e}_1$. Now, without relative horizontal displacement between the sheet and the substrate, the lubrication equation (Eq.3.20) gives

$$\frac{B}{12\eta_0}\frac{\partial}{\partial r_1}\left(Z^3\frac{\partial^5 Z}{\partial r_1^5}\right)=\frac{\partial Z}{\partial t} \tag{3.21}$$

If the characteristic horizontal length at which $Z$ varies is defined by $L$, the dynamic of a given point will be roughly described by

$$\frac{\partial Z}{\partial t}\approx\frac{B}{12\eta_0}\frac{Z^4}{L^6}$$

Because $Z$ must be much smaller than any other scale in the geometry of the fluid film, we write $L/Z > 10$, so that the characteristic time $\tau$ required to decrease $Z$ in a quantity equivalent to the thickness $h$ of the elastic sheet is expressed by $\frac{h}{\tau}\lesssim 10^{-5}\times\frac{B}{\eta_0 L^2}$. Also, with $L/h > 10$ the linear elasticity approach is guaranteed and the characteristic time gives

$$\tau > 10^7\times\frac{\eta_0 h^3}{B} \tag{3.22}$$

Typically, for strong materials like stainless steel ($B/h^3 \sim 10^{11}\ N/m^2$), the lower bound for the characteristic time in glycerol ($\eta_0 \sim 10^0\ N\cdot s/m^2$) is in the order of $10^{-4}\ s$, while for soft materials like rubber ($B/h^3 \sim 10^6\ N/m^2$) is in the order of seconds, which is large considering that $h$ can be easily much smaller than $Z$.

## 3.3 Naturally curved Ribbons and Geometrical implications

### 3.3.1 Localized folding and rod-ribbon transition

If a rod with rectangular cross-section is subjected to external torques and forces, the final state exhibits a continuous evolution of curvature along the material as predicted by the Euler-Elastica theory of large deflections presented in the section 3.1. However, when one bends a **naturally curved** ribbon, the planar bending deformation often is localized in a fold (see Fig. 3.5A) similar to the hinge-like deformation observed when a tapespring is sufficiently curved [66].

In general, this localization phenomenon is the result of a buckling instability. It separates two distinct regions with parabolic and rectangular cross-sections. When the ribbon is longitudinally straightened, the cross-section adopts an arch shape without changing the natural metric of the ribbon (middle part of the picture in Fig. 3.5B). The final state is determined by the classical strain relationship for rods $\varepsilon_b = -\nu\varepsilon_t$ (see section 3.1 for details), where $\nu$ is the Poisson's ratio of the material and ($\varepsilon_t$, $\varepsilon_b$) are the

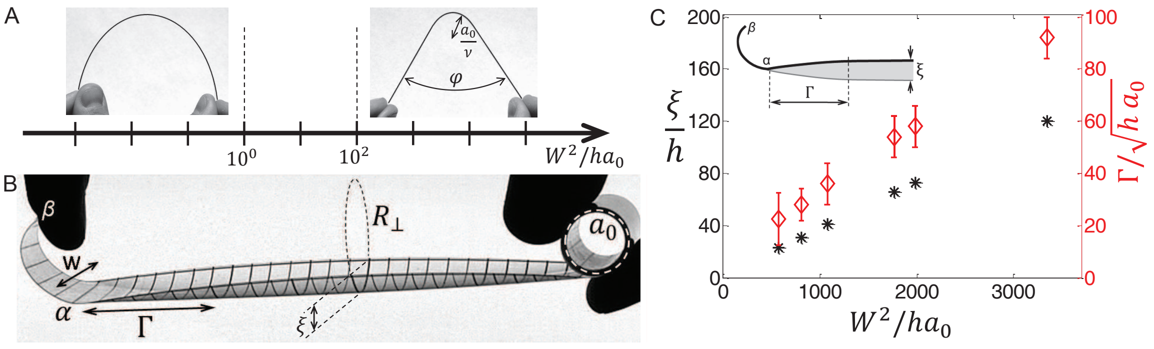

Figure 3.5: (A) Diagram showing two different deformation scenarios with a PVC200 ribbon with the same $a_0 = 0.75$ cm: (left) $W = 0.2$ cm, (right) $W = 1.0$ cm. (B) An uncoiled ribbon of natural radius $a_0$ and width $W$. (C) Experimental measurements of the lengths $\xi$ and $\Gamma$ normalized by $h$ and $\sqrt{ha_0}$ respectively. $\Gamma$ is defined by two times the distance between the point $\alpha$ and the point at which the effective thickness of the cross-section is equal to $\xi/2$ (the ribbons used were made with PP90 and different widths $W =$ [1.9cm; 2.3cm; 3.0cm; 3.5cm; 3.8cm; 4.8cm] associated with the natural radii $a_0 =$ [0.7cm; 0.73cm; 0.9cm; 0.81cm; 0.75cm; 0.75cm]).

strain elements along the tangential $\hat{t}$ and the binormal $\hat{b}$ directions (see Fig.3.6A). Thus, for this specific situation, the radius $R_\perp$ of the cross-section (see Fig. 3.5B) is related with the natural radius $a_0$ through the formula $R_\perp = a_0/\nu$. In addition, the density of elastic energy (energy per unit surface of the ribbon) stored in such straightened state is $F_s = \frac{Eh^3}{24a_0^2}$, where $E$ is the Young modulus and $h$ is the ribbon thickness. On the other hand, when the material is longitudinally curved, a parabolic cross-section is not compatible with an isometric deformation. Therefore, for a relatively low longitudinal curvature, the cross-section buckles and becomes rectangular ($\varepsilon_b \to 0$). The density of elastic energy in this region is $F_f = \frac{Eh^3}{24a_0^2}\frac{(1-\kappa)^2}{1-\nu^2}$, where $\kappa$ is the dimensionless curvature along the longitudinal direction (in this article, all dimensionless lengths or curvatures are constructed with respect to the natural radius $a_0$ or the natural curvature $1/a_0$). The minimum $\kappa$ admitted by a localized fold can be easily obtained by minimization of the elastic energy of the system: taking the right-side picture of Fig. 3.5A as a reference for the calculus, by virtue of the pure torque configuration, $\kappa$ is constant in the fold region which has a length $l_f \approx (2\pi - \varphi)/(a_0\kappa)$. Then, considering that the energy stored in the transition area between the distinct modes of deformation (see definition of $\Gamma$ in Fig. 3.5B) is independent of the shape of the fold, the dimensionless curvature compatible with the minimum of the total energy is obtained from

$$\frac{\partial}{\partial\kappa}\left(l_f F_f\right) - F_s\frac{\partial l_f}{\partial\kappa} = 0 \Leftrightarrow \kappa = \nu$$

The result is independent of the angle $\varphi$, implying that, when an arbitrary bending planar deformation is produced, $\nu$ represents the minimum $\kappa$ accessible by the ribbon. Noteworthy, $\nu$ is also the dimensionless curvature of the curved cross-section in the straightened state. This is analogous to the problem of the deployment dynamics of tapesprings [66]: once the fold is formed, the curvature becomes independent of external torques and it is given with a good approximation by the initial curvature of the cross-section.

Certainly, this analysis is valid for ribbons with sufficiently large widths $W$, otherwise the system can not be distinguished from a simple rod and localized folds should not form. In Fig. 3.5, we show that few millimeters in the width can make the difference between rod-like and ribbon-like behaviors. In order to quantify the critical $W$ for this rod-ribbon transition, we draw attention at the necessary geometrical conditions for buckling to occur and, therefore, the existence of a localized fold. We characterize the deformation of a rod by means of $\kappa$ and the dimensionless curvature $\kappa_\perp$ associated with the center line $C$ of the cross-section (see Fig. 3.6A). Then, we find the value of $W$ at which, for $\kappa \geq \nu$, a planar deformation (where $\varepsilon_b \to 0$ and $\kappa_\perp = 0$) minimizes the elastic energy. In fact, as we will see in the next paragraph, with a variational argument and using a small coupling between $\kappa_\perp$ and the strain elements, we extend the classic strain relationship to get a criterium that reflects the rod-ribbon transition.

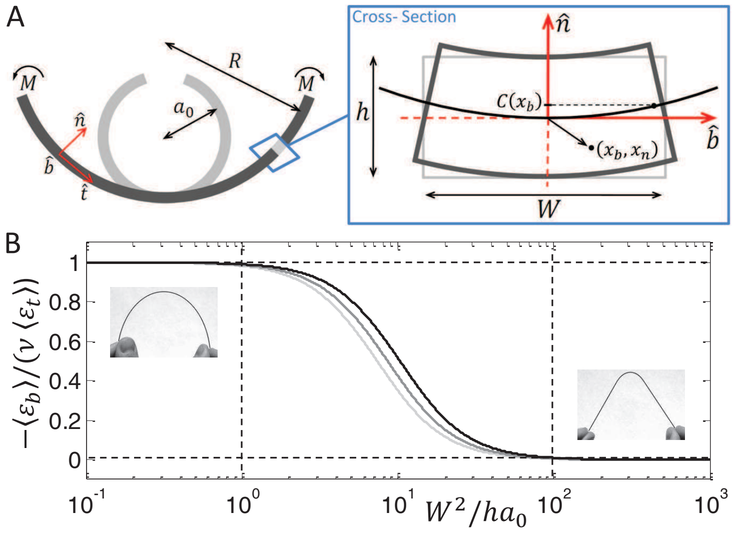

Figure 3.6: (A) Sketch of a bent rod of natural radius $a_0$ and rectangular cross-section (thickness $h$ and width $W$). The drawing describes the deformation of the cross-section through the perpendicular center line $C\,(x_b)$. (B) Plot of Eq.3.23 evaluated for $\kappa = \nu$ and for three different Poisson's ratios in the range of classical materials (from the light-grey curve to the black one: $\nu$=[0.3; 0.4; 0.5]). The vertical dashed lines indicate the limit of behavior between a perfect rod and a ribbon.

In the sketch of a bent rod in Fig. 3.6A, we define $(x_n,\, x_b)$ the dimensionless coordinates of any point of the cross-section with respect to the directions $\hat{n}$ and $\hat{b}$ of the neutral line. The center line of the cross-section $C\left(x_b\right)$ is approximated by the parabola $\frac{1}{2}\kappa_\perp x_b^2$. Considering only the first order displacements in the cross-section, the strain in the $\hat{t}$ direction is written $\varepsilon_t = (1-\kappa)(x_n + C)$ and the strain in the $\hat{b}$ direction is taken as a simple bending $\varepsilon_b = -\kappa_\perp x_n$. The general density of elastic energy (energy per unit volume) for small deformation in thin materials can be written [42]:

$$\mathcal{F} = \frac{E}{2\left(1-\nu^2\right)}\left\{\left(\varepsilon_t+\varepsilon_b\right)^2 - 2\left(1-\nu\right)\varepsilon_t\varepsilon_b\right\}$$

Minimizing the total energy of the cross-section with respect to $\kappa_\perp$, we obtain

$$-\frac{1}{\nu}\frac{\langle\varepsilon_b\rangle}{\langle\varepsilon_t\rangle} = \frac{1}{1+\frac{3}{80}\left(1-\kappa\right)^2\left(\frac{W^2}{ha_0}\right)^2} \tag{3.23}$$

,where $\langle\varepsilon_b\rangle = -\kappa_\perp x_n$ and $\langle\varepsilon_t\rangle = (1-\kappa)x_n$ are the average values of the strains along $W$. In Fig. 3.6B, we show the strain ratio $-\frac{1}{\nu}\frac{\langle\varepsilon_b\rangle}{\langle\varepsilon_t\rangle}$ evaluated at $\kappa=\nu$ as a function of $W^2/ha_0$. This parameter which we call the “Tape Spring Number" (TSN), also controls important aspects of curling dynamics as we will see later. When $\frac{W^2}{ha_0} \gtrsim 10^2$, $\varepsilon_b \to 0$ and the ribbon should be able to localize planar deformations. When $\frac{W^2}{ha_0} \lesssim 10^0$ however, the classical rod relationship is recovered. For a more intuitive interpretation of the TSN, we can argue that a curved cross-section generates an effective thickness $\xi \sim W^2/R_\perp \sim W^2/a_0$ (see Fig. 3.5B), much larger than $h$, resulting in a larger effective bending stiffness, so under flexion, a smaller length with rectangular cross-section ($\xi = h$) and bigger longitudinal curvature is energetically more favorable than a lower and homogeneous longitudinal curvature with $\xi \gg h$ and explains in a more qualitative manner the observed localization. The ratio $\xi/h$ is, indeed, proportional to $\frac{W^2}{ha_0}$.

### 3.3.2 The characteristic length $\Gamma$

When a ribbon is completely straightened, its shape is defined by $\kappa = 0$ and $\kappa_\perp = \nu$ (Fig. 3.5). During a typical curling deformation, the curled region propagates where $\kappa \geq \nu$ and $\kappa_\perp = 0$ (the fold region). These two zones are separated by the length $\Gamma$ which depends strongly on the width and where the Gaussian curvature does not cancel out. In this region, both stretching and bending energies vary with the same power law in $W$ [84]. The stretching deformation can be estimated through the characteristic elongation rate of the side border of the ribbon: $\Delta = \frac{-\Gamma+\sqrt{\Gamma^2+\frac{1}{4}\xi^2}}{\Gamma} \approx \frac{1}{8}\left(\frac{\xi}{\Gamma}\right)^2$. Thus, the stretching energy is $U_{\Gamma_S} \sim Eh\Delta^2 W\Gamma \sim Eh\frac{\xi^4}{\Gamma^3}W$. Also, the associated bending energy, can be taken directly as a scale of the energy required to keep rectangular the cross-section along the distance $\Gamma$: $U_{\Gamma_B} \sim \frac{Eh^3 W\Gamma}{a_0^2}$. Imposing the condition $\frac{U_{\Gamma_B}}{U_{\Gamma_S}} \sim W^0$ , and because $\xi \sim \frac{W^2}{a_0}$, the scaling law we find writes as: $\Gamma \sim \frac{W^2}{a_0^{1/2}h^{1/2}}$ and $\frac{\Gamma}{\sqrt{ha_0}} \sim$ TSN. In Fig. 3.5C, we plot $\frac{\Gamma}{\sqrt{ha_0}}$ as well as $\xi/h$ versus the TSNs and the curves show indeed the expected good linear trends.

## 3.4 Mechanical properties of the Ribbons used in the experiments

For the experiment we used long ribbons more than 1 meter long. They are cut with different widths $W$ ranging from 0.5 cm to 12 cm, from sheets of different materials and mechanical properties reported in Table 3.1. The natural radius $a_0$ is induced by cooking the ribbons over night winded up around metallic cylinders at 60°C in the case of plastic materials or using a flame and fast quenching in cold water for stainless steel. $a_0$ ranges typically from 0.5 cm to 6 cm much larger than the thickness $h$ to insure linear elasticity approximation.

Table 3.1: Ribbons properties used in the experiments ($B$, the Bending Stiffness; $\sigma$, surface density; $\nu$, Poisson's ratio; $h$, ribbon thickness)

| Material | Name | B mN.m | $\sigma$ Kg/m$^2$ | $\nu$ | h $\mu$m |
|---|---|---|---|---|---|
| PolyVinylChloride | PVC100 | $0.34 \pm 0.03$ | 0.143 | 0.38 | 100 |
| PolyVinylChloride | PVC200 | $2.1 \pm 0.1$ | 0.265 | 0.38 | 200 |
| PolyPropylene | PP90 | $0.15 \pm 0.02$ | 0.085 | 0.31 | 90 |
| Stainless Steel | SS100 | $1.1 \pm 0.2$ | 0.3 | 0.3 | 100 |

Bending stiffnesses $B$ are obtained by a simple cantilever experiment. Briefly, one end of a flat ribbon of dimensions 3.5 cm × 20 cm, is immobilized vertically on the sharp edge of a table to form a cantilever system. At the other end, different weights $N$ (between 3 and 25 grams) are hung and the ribbon takes the shape of an arch. The distance $d$ between the vertically clamped edge and the hanging one gives the bending stiffness of the material through de formula [42] $d = \sqrt{4BW/N}$. We obtain the value of the Poisson's ratio $\nu$ of the materials directly by the measure of the perpendicular radius $R_\perp = a_0/\nu$. In brief, a coiled ribbon of natural radius $a_0 = 0.5$ cm and dimensions 3.5 cm × 20 cm, is straightened on a table keeping flat its two extremities. We project a laser sheet over the transverse direction of the strip to obtain the profile of the curved cross-section that we fit by a circle of radius $R_\perp$. The measure is repeated for the different radii $a_0$ we use in the experiment.

### 3.4.1 Viscoelastic characterization

Some materials can exhibit both elastic and viscous characteristics when undergoing deformation. The simplest way to consider the bending response of such materials is by means of the Kelvin-Voigt model, which supposes that the infinitesimal tensile stress in any point of the material can be written:

$$\sigma = E\varepsilon + \eta \frac{d}{dt}\varepsilon \tag{3.24}$$

, where $E$ is the young modulus of the material (it is measured in quasi-static experiments), $\varepsilon$ is the local tensile strain and $\eta$ is the inner viscosity of the solid material. The equation expresses the stress, $\sigma$, with a linear combination of the a pure Hookean elastic term and a newtonian viscous stress.

For bending deformation, the principal strain is proportional to the local curvature (see Eq.3.3). Therefore, in consideration to the Eq.3.6, the resultant torque in the cross-section of a rectangular beam is

$$\frac{\mathbf{M}(r_t)}{W} = (\hat{n} \times \hat{t}) \left[ B\kappa + \frac{\eta h^3}{12a_0}\dot{\kappa} \right] \tag{3.25}$$

, where $\dot{\kappa}$ is the time derivative of the normalized local curvature.

PVC and PP are intuitively thought to behave as purely elastic materials. Their viscoelastic characteristics can nevertheless be well illustrated and measured by means of a cantilever experiment (see Fig. 3.7): a piece of a naturally straight ribbon is bent and released on one end while the other is maintained straight and immobile. Unlike SS ribbons, PVC and PP ribbons exhibit a damped oscillation around a bent geometrical configuration, different than the natural straight position. This state relaxes to the unstrained state in a time scale much larger than the period of one oscillation. This peculiar behavior can be described at short time scales ($\lesssim 10$ oscillations), by a Kelvin-Voigt solid model of viscosity $\eta_s$ and of the residual stress ratio $\phi$, which is the fraction between the stress associated with the centre line of the oscillation and the initial stress in the cantilever. Thus, using these two viscoelastic parameters, with Eq.3.25 we write the local flexural torque of the naturally curved ribbon

$$|\mathbf{M}| = \frac{B}{a_0}(1 - \phi - \kappa) - \frac{\eta_s h^3}{12a_0}\dot{\kappa} \tag{3.26}$$

. From the cantilever experiment, we have extracted $\eta_s \lesssim 10^6$ [Pa. s] for all materials as well as $\phi = 0.20 \pm 0.03$ and $\phi = 0.11 \pm 0.03$ for PP and PVC ribbons respectively (it was confirmed that SS ribbons behave in a purely elastic way with $\phi = 0.00 \pm 0.03$).

With the cantilever setup, the ribbons deform plastically when stressed with a fixed

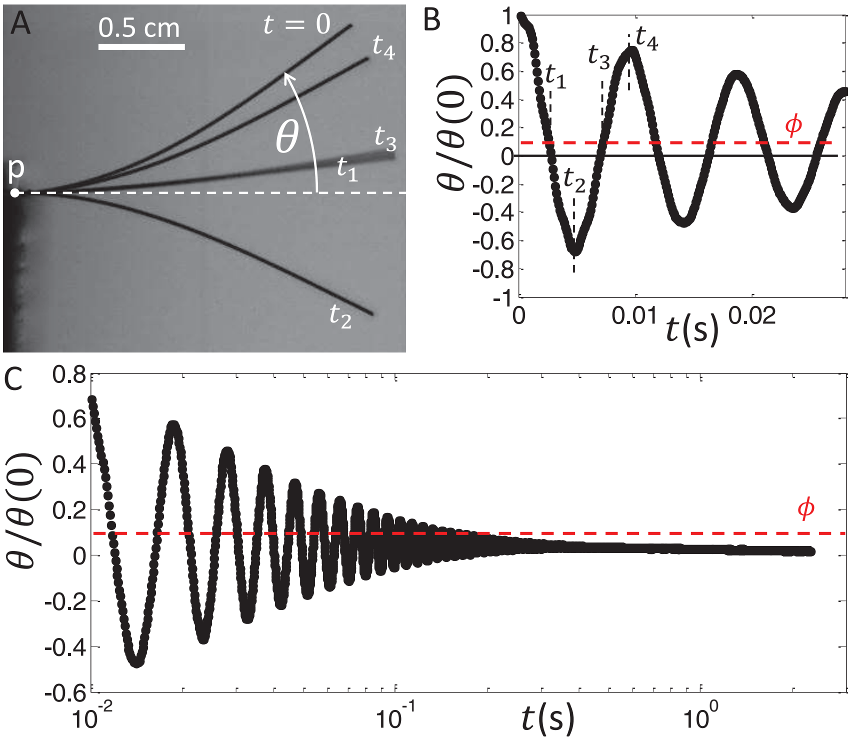

Figure 3.7: Oscillating cantilever experiment (with embedded point $p$) of a flat piece of PVC200. (A) Superposition of 5 pictures during the first oscillation in the experiment, the different times are: $t_1 \approx 2.5$ ms; $t_1 \approx 5.0$; $t_1 \approx 7.5$ ms; $t_1 \approx 10.0$ ms. For relatively small bending, the tangential angle $\theta(t)$ of the free end, defines the global state of deformation. (B) Tangential angle $\theta$ normalized by its initial value $\theta(0)$ as a function of time for the three first oscillations in the experiment. Since $\theta$ is linear with the strain and the strain is linear with the stress, the center of the normalized oscillation $\phi$ can be interpreted as the ratio between a residual stress in the material and the initial imposed stress. (C) $\theta/\theta(0)$ v/s time for the full experiment.

load on long time scales of several tens of minutes (creeping test). This effect can be measured easily. One needs only to keep a constant angle $\theta$ during a given time and observe, after releasing the load, how much the initial natural curvature of the ribbons have changed. This simple protocol shows that PP and PVC ribbons start to exhibit important plastic deformations (the natural curvature changes more than 5 %) when large deflections (strains of the order of 0.01) are applied on the cantilever during more than 5 min. This remark is especially important in the chapter 4 where the full process of curling in viscous oils of large viscosity (100000 cSt) could take easily more than 30 min. Thus, in order to be sure that the dynamics is not contaminated by plastic deformations, we worked with lower viscous oils (12500 cSt) in order to maintain the experimental curling times smaller than 3 min.

## 3.5 Experimental Setup for curling

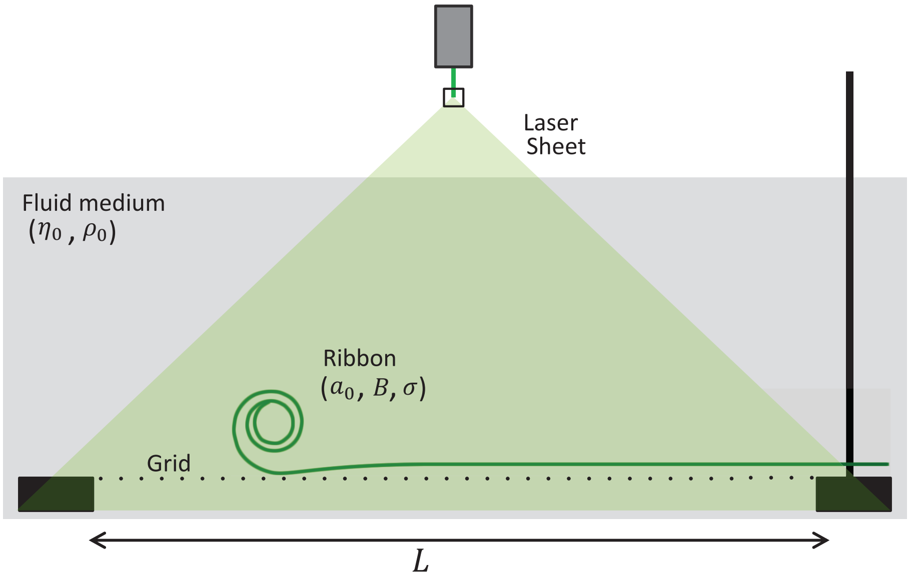

Figure 3.8: Scheme of the general setup used during curling experiments.

In a typical curling experiment, we release one end of a ribbon initially held straight on a horizontal grid by clamping its two extremities flat and we capture its movement with a high speed camera (Phantom V7, Vision research) or a simple shooting Nikkon camera with 18mm objective. A grid (dot line in Fig.3.8) is used as a platform for curling motion (instead of a substrate) to disregard any possible viscous addition in the contacts. The grid platform is placed inside of an aquarium of length $L \approx 1$ m, which is the container of the different liquids used in the experiments. When the curling is performed in very viscous oil, a laser sheet is used to visualize the profile of the ribbon.

# Chapter 4

# Curling of naturally curved ribbons at high Reynolds number

---

Here, using plastic and metallic ribbons, we tune separately the curvature, the width and the thickness, to study curling dynamics in air and in water, concentrating on the high Reynolds number regime. Our work separates the role of elasticity, gravity and hydrodynamics from inertia and geometry, emphasizing the fundamental differences between the curling of naturally curved ribbons and rods. Since ribbons are an intermediate class of objects between plates and rods, they allow us to explore the effect of non planar deformations and the role of Poisson's ratio on curling in the simplest possible manner.

## 4.1 Experimental results for curling and rolling

### 4.1.1 Curling deformation

The first salient observation in our experiments is the presence of a regime of curling deformation different than the numerical self-similar solution obtained for an Elastica [10], when the TSNs$\gtrsim$ 100. Compared to the low TSN case with the same $a_0$ (Fig. 4.1A), the ribbon buckles on a dimensionless length $S_{buck}$ after a time $t_{buck}$ (Inset Fig. 4.1B), and begins curling up into a spiral shape, but rapidly forms a compact cylinder of a fixed radius $R \approx 2a_0$ that rolls without sliding with constant velocity $V_r$ (Fig. 4.1B).

The dimensionless longitudinal curvature $\kappa$ is inferred from the profile analysis just before self-contact, and corresponding to a curved length $x_\alpha$. $\kappa$ is reported as a function of the dimensionless arc-length position $S$ for two different ribbons in Fig. 4.1C. $S$ goes from 0 at the point $\alpha$ (it marks the origin of the curling front, or in a more general way, the starting point of planar bending in the ribbon), to $x_\alpha$ at the free end $\beta$. The boundary condition at the free end imposes $\kappa = 1$ locally. The boundary condition at $\alpha$ is imposed by the localized fold criteria and thus depends on TSN. The curvature of the lowest TSN ribbon, increases monotonously from 0 (imposed by the substrate) towards 1, as expected. In contrast, for the high TSN ribbon $\kappa$ starts from a value of 0.4 close to the Poisson's ratio $\nu$ (the minimum $\kappa$ admitted in a localized fold that has been previously calculated), then, a plateau appears close to $a_0/R = e$ (the dimensionless curvature of rolling), followed successively by a local maximum and a minimum in the curvature and a final rapid increase towards 1 at the free end.

### 4.1.2 Full kinematics diagram

The second important observation of our experiments is the existence of different regimes in the propagation speed of the curling front. In Fig. 4.2 the full kinematics diagram of curling is shown: different trends of positions $(x_\alpha - S_{buck})$ as a function of the time $(t - t_{buck})/t_0$ are represented for ribbons with approximately the same $a_0$ but different TSNs. We use, as a renormalization time $t_0$, which represents the characteristic time for a flexural wave of wavelength $a_0$ to propagate down the material [10]: $t_0 = a_0^2\,(\sigma/B)^{1/2}$, where $B = \frac{Eh^3}{12(1-\nu^2)}$ is the bending stiffness and $\sigma$ is the surface density of the ribbon. At shorter time scales $(t - t_{buck})/t_0 \lesssim 1$, and after buckling, the curling front accelerates continuously for large TSNs, while it decelerates otherwise (lower inset in Fig. 4.2). This is represented by the fact that experimentally $(x_\alpha - S_{buck}) \sim (t - t_{buck})^\zeta$, where $\zeta$ ranges from 0.5 for TSNs$\lesssim 1$ to 2 when TSNs$\gtrsim 10^4$ (Fig. 4.2). At long time scales $(t - t_{buck})/t_0 \gtrsim 10$, all the ribbons reach a constant rolling velocity independent of the TSN (Upper inset in Fig. 4.2), but which varies with the elastic properties and the gravitational interaction (see red symbol Fig. 4.2).

Indeed, for a given material and ribbon geometry, when $a_0$ is greater than a critical value $a_0^*$, gravity dominates and curling is prevented. For $a_0 < a_0^*$, we observe that the roll normalized curvature $e$ decreases with the ratio $a_0^*/a_0$, as represented in Fig. 4.3, from values larger than 1 to a limiting average value of $0.48 \pm 0.2$, where gravity can be neglected (values of $a_0^*$ are given in the legend of Fig. 4.3).

Finally, in Fig. 4.4, we show the variation of $V_r$ obtained from Fig. 4.2 at long time scales, for three different materials as a function of $a_0^*/a_0$. When $a_0^*/a_0 \gg 1$, the speed changes linearly with the natural curvature and gravity is negligible. When $a_0^*/a_0$ is close to 1, the variation is non-linear and gravity plays a large role in the speed selection. Additionally, the velocity of transition $V_r(a_0 = a_0^*)$ is finite and different than zero.

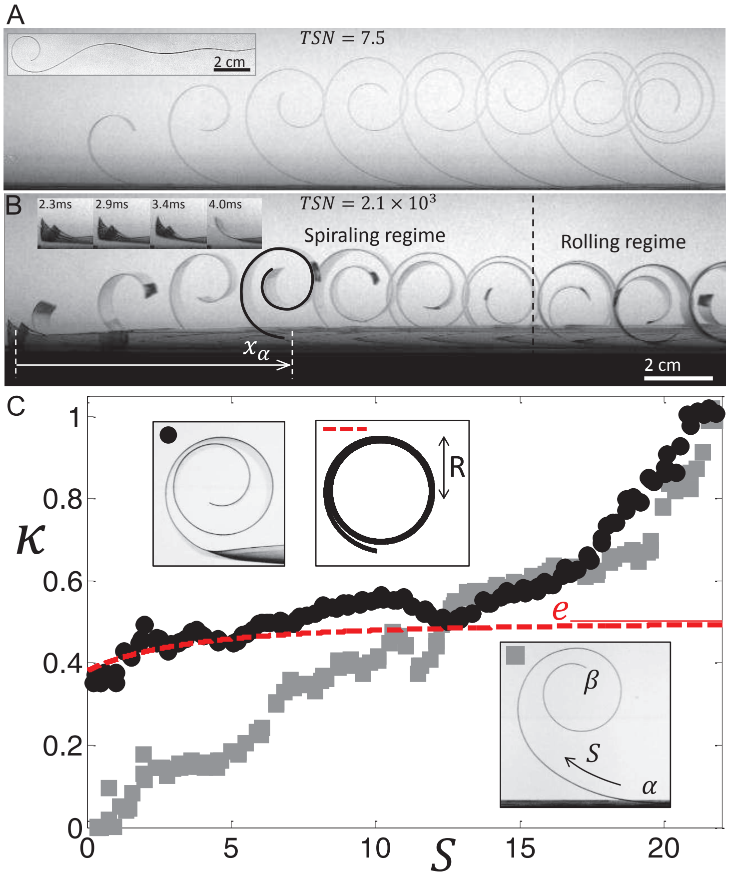

Figure 4.1: (A) Curling sequence (time lapse=10ms) for a ribbon with TSN= 7.5 (PVC200, $a_0$ = 0.6cm , $W$ = 0.3 cm). Inset: Picture shows the typical burst of flexural waves associated with a curling experiment performed without subtrate interaction and small TSN (TSN= 7.5, PVC200, $a_0 = 0.6$ cm, $W = 0.3$ cm). (B) Curling sequence (time lapse=10ms) for a ribbon with TSN= 2100 (PVC200, $a_0 = 0.6cm$,W=5 cm). Inset: Sequence of picture of the buckling instability observed before curling. (C) Dimensionless curvature $\kappa$ as a function of the dimensionless arc-length $S$: ■, for the profile of a ribbon with TSN= 7.5 at $x_\alpha \approx 22$; •, for a ribbon with TSN= $2.1 \times 10^3$ at $x_\alpha \approx 22$; (- - -) analytical solitary deformation front solution from an elasticity-inertia balance (the curvature associated with each point of the experimental profiles are obtained from the local fitting of a circle). Inset pictures: experimental profile before self-contact and shape of the solitary front solution, corresponding to the $\kappa$ versus $S$ curves. In the bottom inset, $\alpha$ and $\beta$ are defined as the boundaries of the curved part of the ribbon of length $x_\alpha$, corresponding respectively to the initial point of the curling front (when $\Gamma \to 0$ it coincides with the substrate contact point) and the free end.

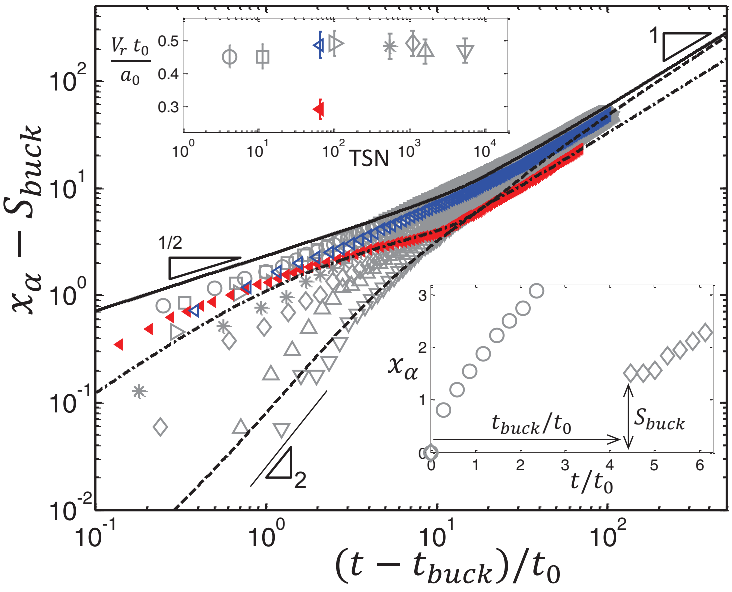

Figure 4.2: Experimental diagram of kinematics: $(x_\alpha - S_{buck})$ as a function of $(t - t_{buck})/t_0$ for PVC200 ribbons with the same $a_0 = 11$ mm $\approx 0.15 a_0^*$ (see text to clarify the meaning of $a_0^*$) and $t_0 = 1.1$ ms, except ◀, which is for a PVC100 ribbon with $a_0 = 38$ mm $\approx a_0^*$ and $t_0 = 0.4$ ms. Symbols represent different widths that produce the different TSNs: $\circ$, 4.5; $\square$, 13; ◁ and ◀, 73; ▷, 112; $\ast$, 611; ◇, 1210; △, 1800; ▽, 6100. We can resolve experimentally the buckling parameters $(S_{buck}, t_{buck})$ only when TSN$\gtrsim$ 100 (the different buckling length are $S_{buck} \approx 0.5$; 1.0; 1.5; 2; 4; for ▷, $\ast$, ◇, △, ▽ respectively). Lower right corner: evolution at short time scale for ($\circ$) and (◇). Upper inset: limit value of the normalized curling speed $V_r t_0/a_0$ for all curves. Numerical solutions of Eq.4.3 using $C_D = 1.1$, $\phi = 0.11$ (see text) and the approximation $\dot{x}_\alpha^3 \approx d(x_\alpha \dot{x}_\alpha^2)/dt$: (—) $W \to 0$ (TSN $\lll 1$) and $L_g \to \infty$; (- - -) with parameters of the ribbon in ◀; (- · -) same parameters as in (▽).

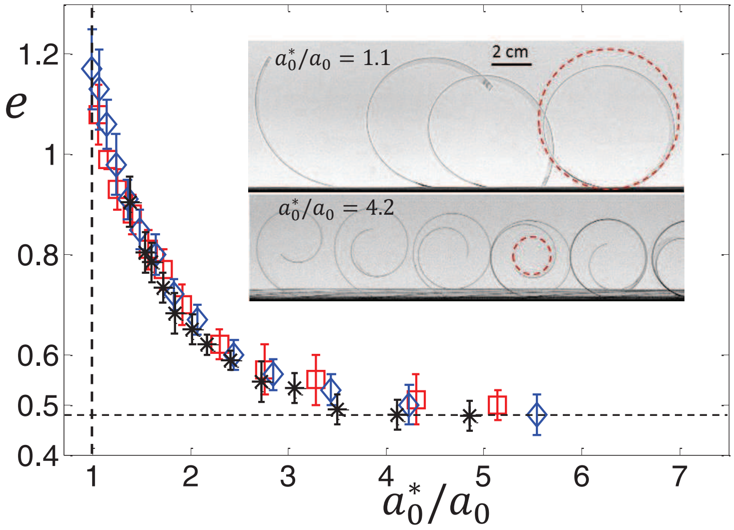

Figure 4.3: Dimensionless curvature of rolling $e = a_0/R$ as a function of $a_0^*/a_0$ (TSN = 300) for the three different materials: ($*$) PVC200 with $a_0^* = 5.7 \pm 0.2$ cm, (◊) PVC100 with $a_0^* = 3.8 \pm 0.2$ cm and (□) PP90 with $a_0^* = 3.7 \pm 0.2$ cm. The experimental data represent the averages of ten identical experiments (the magnitude of the error bars correspond to three times the associated standard deviations). Inset: curling propagation for PVC100 ribbons at $a_0^*/a_0 = 1.1$ (time lapse=0.1s) and $a_0^*/a_0 = 4.2$ (time lapse=0.5s). Dashed circles represent the natural profiles of the ribbons.

### 4.1.3 Curling front and Rolling as a propagating instability

The condition in $\alpha$ (imposed by the substrate for small TSN and by the localized fold criteria for TSN> 100) selects a single propagating front instead of the typical burst of flexural dispersive waves of positive and negative curvatures we observe in the air (inset Fig. 4.1A) and calculated for straight rods by Audoly et al.[2] and first predicted by Boussinesq [6]. In fact, the rolling regime is independent of the presence of a substrate. Since the tip of the $\Gamma$-region displays a much smaller effective bending stiffness than the resting ribbon with circular cross-section, the deformation remains localized and propagates progressively. This is indeed one of the mechanical criterion for a general class of instabilities in mechanics called "propagating instabilities" [41, 66], where a dynamical region of transition separates two deformation states, respectively the roll and the resting part of the ribbon. Propagating instabilities are capable of spreading over the entire material and hence are often described both as critical phenomena to understand in the viewpoint of damage control [41, 58, 36], but also as beneficial in the design of efficient and fast deployment systems in structural engineering [66, 13].

### 4.1.4 Effect of gravity of curling and rolling

#### Elastogravitational Length and The Critical curling radius

The comparison between Fig. 4.1A and 4.1B, shows that the “compact rolling" regime we observe is not due to gravity since, for these specific experiments, the ribbons have the same weight per unit width, and the observed inertial acceleration $V_r^2/R \approx 700\ m/s^2$ is much larger than the gravitational one. In fact, when gravity is not negligible, it stabilizes more the rolling behavior by further pulling down the curled part and, therefore, assures self-contact.

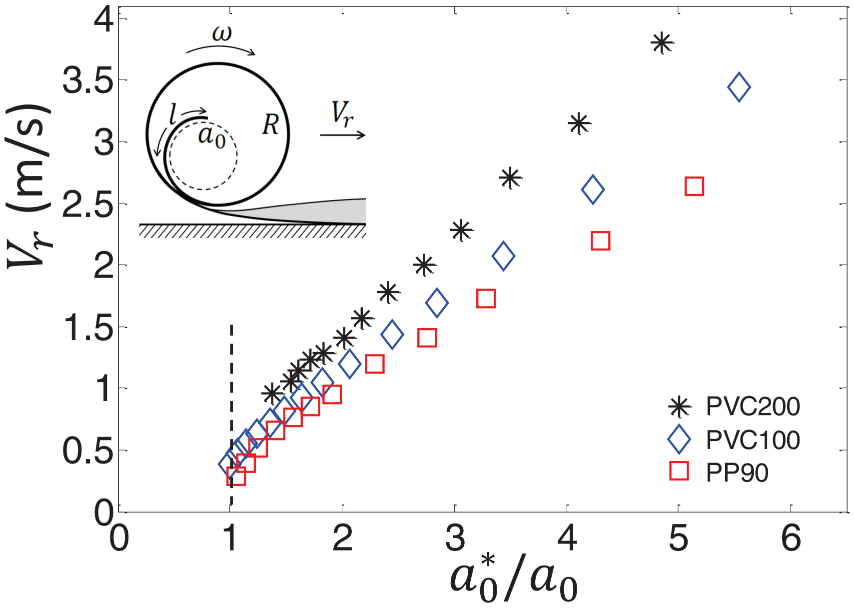

Figure 4.4: Experimental measurements of rolling speed for three different materials with TSN $\approx$ 300. The speed $V_r$ corresponds to the slope of the kinematics trend $a_0 x_\alpha$ versus time for $x_\alpha \geq 20$. Each experimental point represents the average of ten identical experiments (the observed standart deviation is smaller than 0.04 m/s and the maximum deviation is always in the order of 0.1 m/s). The error bars are contained in the size of the symbols.

The usual parameter used to quantify the gravitational force acting on ribbons compared to the bending one is the elasto-gravitational length $L_g = (\frac{Eh^3}{g\sigma})^{1/3}$, $g$ being the gravitational acceleration [61] (the values of $L_g$ of the different materials in Table 3.1 are respectively: 13.6 cm for PVC100; 20.3 cm for PVC200; 12.5 cm for PP90 and 16.0 cm for SS100). When $a_0$ is comparable with $L_g$, the weight of the curled part prevents curling progression. Quickly after the initial release, the ribbon stops around a static configuration without self-contact. Using a heavy Elastica approach, we calculate the smallest natural radius compatible with such static equilibrium to be $0.28L_g$, consistent with the experimental values of $a_0^*$ (see Appendix B).

The critical natural radius $a_0^*$ varies slowly with $\nu$. In the range, $0.3 < \nu < 0.5$, $a_0^*$ varies less than 1%. Thus, curling occurs, in general, only when $a_0 \lesssim 0.28L_g = a_0^*$. For PVC and PP ribbons, we find $a_0^*$ equal to $3.9 \pm 0.1$ cm and $3.8 \pm 0.2$ cm respectively, in good agreement with our observations.

## 4.2 Energy variation during rolling

Based on the experimental evidence of the rolling regime, we rationalize in the following both the scaling laws we observe experimentally as well as the dimensionless curvature of rolling $e$ and the velocity $V_r$, using a balance of energy for the roll movement, coupled to a more refined analysis of the balance of forces and torques of the curled material.

In the following model, we consider that most part of the curling front is located, at any time, very close to a roll of constant dimensionless curvature $e$. Accordingly, the variation of elastic energy $dU_E/dx_\alpha$ is basically given by the energy density in the roll $F_f(\kappa = e)$ minus the energy density $F_s$ of the straightened state. Therefore,

$$U_E = -\frac{BW}{2}\left(\frac{\lambda}{a_0}\right)^2 x_\alpha \tag{4.1}$$

, where $\lambda^2 = 2e - e^2 - \nu^2$.

The kinetic energy can be expressed by the integral $U_{K_C} = \frac{1}{2}\sigma W a_0^3 \int_0^{x_\alpha} \left(\dot{\mathbf{r}}_c + \dot{\mathbf{r}}\right)^2 dS$, where "dot" denotes time derivative, $\mathbf{r}_c$ is the dimensionless position for the average of the curvature-center in the curling front and $\mathbf{r}$ is the dimensionless position of any point measured from $\mathbf{r}_c$ (Fig. 4.5). The vector $\mathbf{r}_c$ can be seen as the position of the center of rotation, then $\dot{\mathbf{r}} \approx \frac{\omega}{e}\hat{t}$, where $\omega$ is the angular speed and $\hat{t} = \frac{d\mathbf{r}}{dS}$ is the tangential direction of any point of the ribbon. Also the time variation of the center of rotation can be approximated with the rolling criterium $\dot{\mathbf{r}}_c = \hat{x}\dot{x}_\alpha$, where $\hat{x}$ is the horizontal unitary vector. The non-sliding condition leads to $\omega = e\dot{x}_\alpha$, then $U_{K_C} = \sigma W a_0^3 \dot{x}_\alpha^2 \left[x_\alpha + \int_0^{x_\alpha}(\hat{x}\cdot\hat{t})dS\right]$. Consistent with our approximations, the dimensionless vertical position of the center of mass with respect to the center of rotation is: $-\frac{1}{x_\alpha}\int_0^{x_\alpha}(\hat{y}\cdot\mathbf{r})dS = -\frac{1}{ex_\alpha}\int_0^{x_\alpha}(\hat{y}\cdot\hat{n})dS \approx -\frac{1}{ex_\alpha}\int_0^{ex_\alpha}(\cos\theta)\frac{d\theta}{e} = \frac{-\sin(ex_\alpha)}{e^2x_\alpha}$ (see Fig. 4.5 for a visualization of the normal unitary vector $\hat{n}$ and the vertical unitary vector $\hat{y}$). Therefore, since $\hat{y}\cdot\hat{n} = \hat{x}\cdot\hat{t}$, the kinetic energy can be written in the simplified way $U_{K_C} = H_e(x_\alpha)ea_0^3\sigma W x_\alpha \dot{x}_\alpha^2$, where $H_e(x_\alpha) = \frac{1}{e} - \frac{\sin(ex_\alpha)}{e^2x_\alpha}$ is the dimensionless height of the center of mass relative to the level of the boundary point $\alpha$.

Finally, the gravitational energy $U_g$ corresponds to the total weight of the curled ribbon multiplied by the height of the center of mass, therefore $U_g = H_e(x_\alpha)a_0^2\sigma W x_\alpha g$.

### 4.2.1 Supplementary kinetic energy of the Γ-region

To these energies, one has to account for the inertial effect due to the presence of the Γ-region, which has to continuously unfold while the curling front propagates.

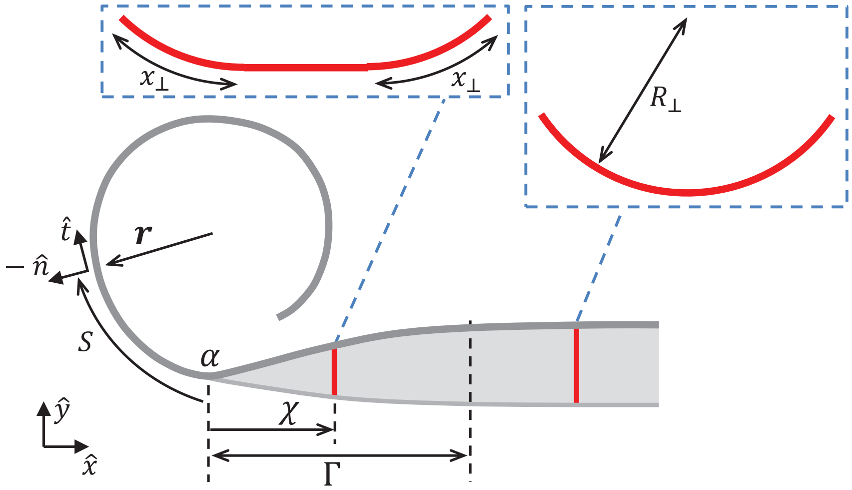

Figure 4.5: Sketch of the displacements in the cross-sections in the Γ-region and references for the description of the curling dynamics.

In order to approximate the kinetic energy of the transient displacement in the cross-sections, we define the horizontal distance $\chi$ from the boundary point $\alpha$ to an arbitrary position associated with a specific cross-section in the Γ-region (see Fig. 4.3); the cross-sections are characterized by two circular pieces of dimensionless length $x_\perp$ which increases until it reaches a maximum $\frac{1}{2}\frac{W}{a_0}$ when $\chi \to \Gamma$. Considering the linear dependence $x_\perp \approx \frac{1}{2}\frac{W}{a_0}\frac{\chi}{\Gamma}$ and approximating the curved pieces with arcs of radius $R_\perp = a_0/\nu$, the infinitesimal contribution to the kinetic energy $\delta U_{K_\Gamma}$ of an arbitrary cross-section can be written by analogy to the previous result for the kinetic energy of the curled material:

$$\delta U_{K_\Gamma} = 2H_\nu(x_\perp)\nu a_0^3 \sigma x_\perp \dot{x}_\perp^2 \delta\chi.$$

The characteristic time of the transient deformation in the cross-section is $W/(a_0 \dot{x}_\perp)$, but this quantity is equivalent to the time during which the curling front advances a distance $2\Gamma$, so $\dot{x}_\perp = \frac{1}{2}\frac{W}{\Gamma}\dot{x}_\alpha$. Writing the energy in terms of $\chi$ and $\dot{x}_\alpha$, we get the total energy $U_{K_\Gamma}$ by simple integration:

$$\begin{aligned} U_{K_\Gamma} &= \frac{\sigma a_0^2}{4}\left(\frac{W}{\Gamma}\right)^3 \dot{x}_\alpha^2 \int_0^\Gamma \left(1 - \frac{\sin\left(\frac{\nu W \chi}{2a_0\Gamma}\right)}{\left(\frac{\nu W \chi}{2a_0\Gamma}\right)}\right)\chi d\chi \\ &= C a_0^2 \sigma W \Gamma \dot{x}_\alpha^2 \end{aligned}$$

, where

$$C = \frac{1}{8}\left(\frac{W}{\Gamma}\right)^2\left[1 - \frac{16a_0^2}{W^2\nu^2}\sin^2\left(\frac{W\nu}{4a_0}\right)\right]$$

### 4.2.2 Asymptotic behaviors and experiments

Without dissipation, the sum of the kinetic energies and the variation of the potential energies of the problem must be zero at any moment in time, which implies a differential equation for $x_\alpha$ that can be integrated numerically. Three asymptotic behaviors can be deduced in agreement with the experimental data shown in Fig. 4.4. For short time scales, $x_\alpha \ll 1$, $H_e(x_\alpha) \sim x_\alpha^2$ and $U_{K_C} \sim x_\alpha^3 \dot{x}_\alpha^2$, the gravitational potential $U_g \sim x_\alpha^3$ is negligible compared to the elastic energy $U_E \sim x_\alpha$; so, when $\Gamma = 0$, the balance of energies can be written $U_{K_C} \sim U_E$ and, therefore, $\dot{x}_\alpha \sim 1/x_\alpha \Leftrightarrow x_\alpha \sim \sqrt{t}$. When $x_\alpha \ll 1$ and $\Gamma \gg a_0$, $U_{K_\Gamma} \sim \dot{x}_\alpha^2$ is dominant and the energy balance is expressed by $U_{K_\Gamma} \sim U_E$, which leads to $\dot{x}_\alpha \sim \sqrt{x_\alpha} \Leftrightarrow x_\alpha \sim t^2$. These results highlight the important role played by the initial inertia of the system.

### 4.2.3 Rolling Speed and Λ-Function

For long time scales, since $x_\alpha \gg 1$ and $H_e(x_\alpha) = 1/e$, then $U_{K_\Gamma} \ll U_{K_C} \sim x_\alpha \dot{x}_\alpha^2$, $U_g \sim U_E \sim x_\alpha$ and the speed $\dot{x}_\alpha$ becomes constant with a value equal to

$$V_r/a_0 = \Lambda/t_0 \tag{4.2}$$

, where $\Lambda^2 = \frac{1}{2}\lambda^2 - \frac{(1-\nu^2)}{4e}(a_0^*/a_0)^{-3}$ and $a_0^* = 0.28L_g$. When inertia dominates $\Lambda^2 \to \lambda^2/2$, the ratio $e = a_0/R$ tends to a constant value and the scaling $V_r \sim 1/a_0$ prevails (in agreement with the experimental measurements of Fig. 4.4); on the other hand, for $a_0^*/a_0 \approx 1$, $V_r$ deviates from a power law. In Fig. 4.6 we present the experimental rolling velocity $V_r$ (for PVC100), normalized by the theoretical prediction $\Lambda a_0/t_0$, as a function of $a_0^*/a_0$ (the experimental values of $e$ shown in Fig. 4.3 are used). We observe that the model overestimates the magnitude of the speed of at least 15% for high $a_0^*/a_0$ and almost 40% for $a_0^*/a_0 \approx 1$. We interpreted this discrepancy as an evidence of dissipative processes. The most plausible sources of dissipation in the system should be related with the inner viscosity of the material (viscoelasticity) and the viscosity of the outer environment (air drag), in the following, we will discuss the implications of both effects.

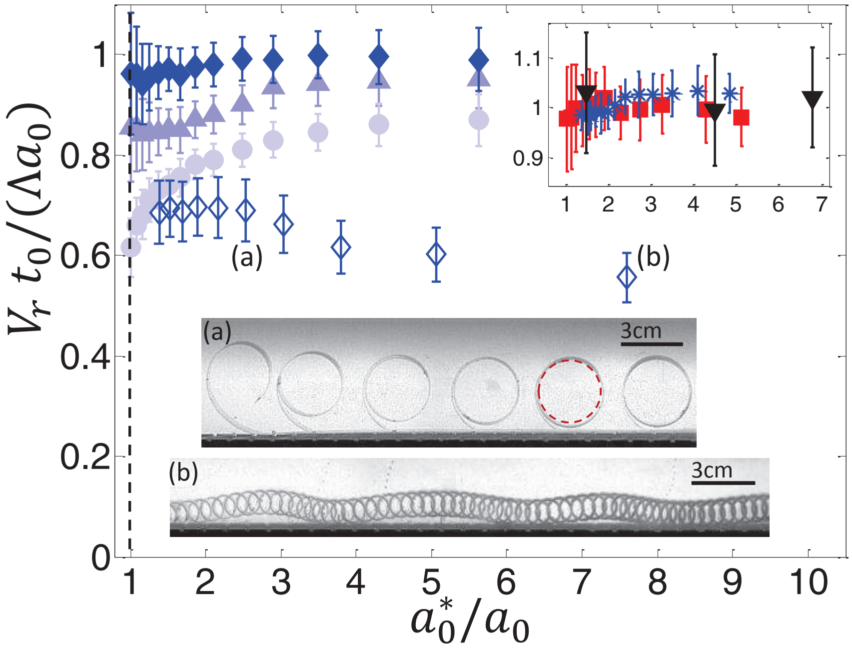

Figure 4.6: $V_r t_0/a_0\Lambda$ as a function of $a_0^*/a_0$ for PVC100 ribbons. $Vr$ correspond to experimental values of rolling speed in air (●, ▲, ♦ ) and water (◊). The function $\Lambda$ is computed for different situations: (●) without dissipative processes ($\phi = 0$ and $D = 0$),(▲) with only viscoelastic dissipation ($\phi = 0.11 \pm 0.03$ and $D = 0$), (♦) with both air drag and viscoelastic interaction ($\phi = 0.11 \pm 0.03$ and $D \lesssim 0.32$), (◊) rolling in water with viscoelastic and viscous dissipation ($\phi = 0.11 \pm 0.03$ and $D \lesssim 356$). Upper inset: rolling in air, of three different materials considering air drag and viscoelasticity; (■) PP90, ($*$) PVC200 and (▼) SS100. Lower insets: Curling sequences in water for (a) (time lapse=0.35s) and (b) (time lapse=0.01s).

## 4.3 Dissipation sources

In order to estimate qualitatively the rolling speed, we consider in the following the two different sources of dissipation in the experiment induced by drag forces and disco-elastic effects.

### 4.3.1 Effective torque

In the section 3.4.1 has been shown, by means of a cantilever experiment, that the flexural torque of PP and PVC ribbons can be written in the the following visco-elastic manner (Eq.3.26):

$$|\mathbf{M}| = \frac{B}{a_0}(1-\phi-\kappa) - \frac{\eta_s h^3}{12a_0}\dot{\kappa}$$

, where $\eta_s \sim 10^6$ Pa.s and $\phi = 0.20 \pm 0.03$ or $\phi = 0.11 \pm 0.03$ for PP and PVC ribbons respectively.

During curling, since $\dot{\kappa} \sim 1/t_0$, the pure viscous torque $\frac{\eta h^3}{12a_0}\dot{\kappa} \sim \frac{1}{12}\frac{\eta h^3}{a_0 t_0}$ can be neglected compared to the residual one $\sim \frac{B\phi}{a_0}$. Therefore, viscoelasticity produces an effective elastic torque but a negligible viscous dissipation. Including this effect by means of an effective natural curvature $(1-\phi)/a_0$, we rewrite $\lambda^2 = \lambda_0^2 - \lambda_\phi^2$ in $U_E$, where $\lambda_0^2 = 2e - e^2 - \nu^2$ represents the pure elastic part of the energy and $\lambda_\phi^2 = 2\phi e - 2\phi\nu^2 e^2 + \phi^2\nu^2$ the residual one. The viscoelastic correction for $V_r$ is obtained by replacing $\lambda$ in Eq.4.2.

This viscoelastic correction improves the prediction of the rolling speed significantly as shown in Fig. 4.6 (for PVC100) especially for values of $a_0^*/a_0 > 4$. However, this correction is not satisfactory: there is still a small difference on the speed for high values of $a_0^*/a_0$ and more than 10% of difference for the larger radii. In order to find the origin of this deviation, we proceed with the analysis of the air drag during rolling.

### 4.3.2 Effect of air drag: vanishing Cauchy numbers

We consider, as a first approximation, that the resultant drag force is roughly associated with the one of the flow passing around a solid cylinder: $F_D = C_D \rho_f W R \dot{x}_\alpha^2$, where $C_D \approx 1.1$ is the drag coefficient [80] and $\rho_f$ is the fluid density. We modify the energy balance writing the dissipated power as $F_D \dot{x}_\alpha = D\sigma W \dot{x}_\alpha^3$, where $D = \frac{C_D \rho_f a_0}{e\sigma}$, leading to:

$$D\sigma W \dot{x}_\alpha^3 = \frac{d}{dt}(U_E + U_{K_C} + U_{K_\Gamma} + U_g) \tag{4.3}$$

At long time scales, using $\ddot{x}_\alpha = 0$, this equation leads to the rewriting of the rolling speed with a new function $\Lambda$, which satisfies $2(1+D)\Lambda^2 = \lambda_0^2 - \lambda_\phi^2 - \frac{(1-\nu^2)}{2e}(a_0^*/a_0)^{-3}$. Noteworthy, the Cauchy number $C_Y$ appears in $\Lambda$ since it is the ratio between the characteristic drag force $\sim D\sigma V_r^2 \sim \frac{D}{1+D}\frac{B}{a_0^2}$ and the characteristic elastic force $\sim \frac{B}{a_0^2}$ and therefore $C_Y = \frac{D}{1+D}$.

This energy balance predicts quantitatively $V_r$ in air when $C_Y \ll 1$ without any adjustable parameters for the four materials used (see Fig. 4.6). Also, exploiting the fact that the product $x_\alpha \dot{x}_\alpha \ddot{x}_\alpha$ is always a small quantity independent of TSN, we can use the aproximation $\dot{x}_\alpha^3 \approx \frac{d}{dt}(x_\alpha \dot{x}_\alpha^2)$ and solve the Eq.4.3 with a simple numerical integration (after the respective separation of variables). In Fig. 4.2, three of these solutions have been plotted for three different situations of curling and they are in good quantitative agreement with the experiments.

### 4.3.3 Effect of drag in water: Cauchy numbers close to unity

In water however, where $C_Y \approx 1$, the model fails to predict $\Lambda$ accurately (see Fig. 4.6). In the range $1 < a_0^*/a_0 \lesssim 2.5$, while we observe a rolling regime with $e \approx 1$ due to a reduced rolling velocity, $V_r$ is 30% overestimated, despite the fact that the expression of the drag force remains the same in the range of Reynolds numbers we are considering ($10^3 - 10^4$) [80]. Another source of dissipation could be missing such as inertial corner flow in the self-contacting propagating region, whose consideration is out of the scope of the paper. Moreover, when $a_0^*/a_0 > 2.5$, the discrepancy worsen for increasing values of $a_0^*/a_0$ (Fig. 4.6). In this case, we observe orthogonal oscillations (inset Fig. 4.6) of frequency $f \approx 0.13\frac{V_r}{2a_0}$ or equivalently a Strouhal number $St_{curling} \approx 0.13$, close to the value found in the literature of 0.2 for static cylinders in this range of Reynolds numbers, where vortex shedding induced oscillations dissipate energy in a more complex manner [83].

### 4.3.4 Force and torque balance: rolling as a solitary curvature wave

While the energy balance predicts a first relationship between the speed $V_r$ and $e$, what fixes the value of $e$ in the inertial case remains to be elucidated. To solve the problem, we use the equilibrium of forces and torques in the curled length during rolling, not considering for simplicity gravity nor drag but taking into account the residual stress.

The balance of forces and torques is expressed with the two coupled differential equations:

$$\mathbf{F}'/a_0 + \mathbf{P} = 0 \tag{4.4}$$

$$\mathbf{M}'/a_0 + \hat{t} \times \mathbf{F} = 0 \tag{4.5}$$

, $\mathbf{F}$ is then the resultant elastic force in the cross-section. $\mathbf{P} = (e\Lambda/t_0)^2\,\sigma a_0 \mathbf{r}$ is the centrifugal density force, where $\mathbf{r}$ is again the dimensionless position vector measured from the center of rotation of the roll. Moreover, $\mathbf{M} = \frac{B}{a_0}(1-\phi-\kappa)(\hat{n}\times\hat{t})$ is the local elastic torque in the material, $(\hat{n},\hat{t})$ are the normal and tangent unitary vectors and prime denotes differentiation with respect to the dimensionless arc-length $S$. Writing $\mathbf{F} = \hat{n}\cdot F_n + \hat{t}\cdot F_t$, Eq.4.4 can be expressed by the two scalar equations $\kappa F_t + F_n' = -a_0(\hat{n}\cdot\mathbf{P})$ and $-\kappa F_n + F_t' = -a_0(\hat{t}\cdot\mathbf{P})$. After eliminating $F_t'$ in the second equation using the derivative of the first one and combining with Eq. 4.5, we get:

$$-\frac{1}{(e\Lambda)^2}\frac{\partial}{\partial s}\left(\frac{1}{2}\kappa^2 + \frac{\kappa''}{\kappa}\right) = 2(\hat{t}\cdot\mathbf{r}) + \frac{\kappa'}{\kappa^2}(\hat{n}\cdot\mathbf{r}) \qquad (4.6)$$

The rolling regime can be described by a solitary curvature wave: both the curvature profile and the speed of propagation are independent of the position $x_\alpha$. For negligible self-contact forces, the curvature must change continuously from the initial value $\nu$ to the rolling curvature $e$. We are interested in solutions compatible with the experimental observation: spirals with slow spatial variation of curvature and with a small dispersion of the curvature center positions, i.e., solutions in which the approximation $\mathbf{r} \approx -\hat{n}/\kappa$ is valid. Using this idea, we neglect the first term of the right hand side of Eq.4.6. After two integrations, we can express the problem as a first order flow $\kappa'^2 = G(\kappa, e)$, with $G = \frac{1}{2}(e^2+\Lambda^2)(\kappa^2-e^2) - \frac{1}{4}(\kappa^4-e^4) - \Lambda^2 e^2 \ln(\kappa/e)$ (physical solutions are restricted for $G \geq 0$ and integration constants are obtained from the roll geometry: $(\kappa')\mid_{\kappa=e} = (\kappa'')\mid_{\kappa=e} = 0$). In a phase diagram representation, the coordinate $\kappa = e$ acts as a fixed point [73] whose stability depends on its magnitude. More precisely, the system has two fixed points, when $e$ is large enough, one fixed point is stable but the principal one, in $\kappa = e$, is not connected with a physical solution (see Fig. 4.7). When $e$ is small, the fixed points become stable and half-stable (in $\kappa = e$) respectively. The solution we are looking for has only one stable roll region and appears under the condition $(\frac{\partial G}{\partial \kappa})\mid_{\kappa=e} = (\frac{\partial^2 G}{\partial \kappa^2})\mid_{\kappa=e} = 0$, when the fixed points coalesce into a single stable point. In this case, the rolling curvature is given by

$$e = \frac{1}{3}(1-\phi)\left(1+\sqrt{1-3\nu^2}\right) \qquad (4.7)$$

which also corresponds to the bifurcation point of this first order system. The formula above predicts $e = 0.52$ for PVC and $e = 0.49$ for PP ribbons in agreement with the experimental limiting value measured from $a_0^*/a_0 \gtrsim 4$ in Fig. 4.2 (where the air drag and the weight are not the dominant interactions). The subsequent curvature solutions $\kappa(s)$

and shape profiles can be easily obtained by numerical integration of $\sqrt{G}$ (in Fig. 4.1C we plot the solution associated with PVC ribbons using a Runge-Kutta method).

Noteworthy, a recent numerical approach of naturally curved Elastica [10] finds a self-similar spiral shape which reaches a constant curling velocity at an infinite time. The associated infinite spiral, concentrates a compact region close to the free end, reminiscent to a roll, tough a closer look to the figure shows many self-intersecting points not taken into accounts in the numerics (see Fig. 3c of [10]). Using the same equations for the equilibrium of forces and torques (Eq. 4.4-4.5), the authors predicted numerically that the dimensionless curvature of such long time scale roll must be 0.564244 in contrast with the value $e = 2/3$ we obtain from our model in Eq. 4.7 for $\phi = 0$ and $\nu = 0$ (without fold localization). This apparent conflict comes from the different ingredients of these two approaches. In the numerical approach of the Elastica, the authors solve the equations with a shooting algorithm using the mentioned “conservation of the angular momentum flux" $\mathbf{M}/a_0 + \mathbf{r} \times \mathbf{F} = 0$ as a constraint, but this formula is a simple combination between Eq. 4.4, Eq. 4.5 and the boundary conditions at the free end. Thus, this constraint by itself, cannot ensure the unicity of the roll solution. On the other hand, in our analytical approach, the local value of the solitary curvature wave cannot be larger than $e$ and the free boundary is irrelevant at infinity. This idea is sustained in the experimentally observed self-contacting solutions, where the bending waves can not travel beyond the solid contact area, shielding the eventual effect of the free end and leading to a different solution than the one proposed in [10].

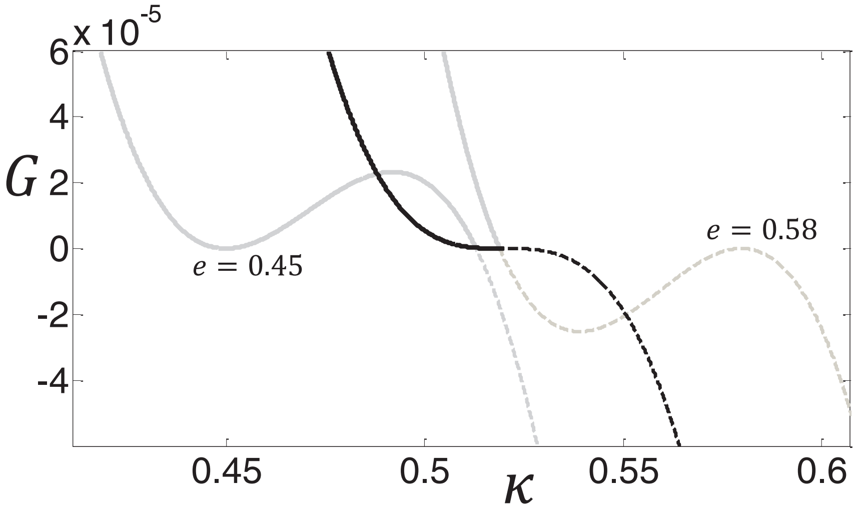

Figure 4.7: Phase diagram ($G = \kappa'^2$ and $\nu = 0.38$) close to the roll region for three different rolling solutions of Eq. 4.6. Each curve has a different roll curvature $e = 0.45$; 0.52 and 0.58 respectively.

## 4.4 Conclusions

In conclusion, for sufficiently high values of the TSN, curling deformation leads to a rolling regime. This behavior originates from the strain localization due to the lateral extension of ribbons. The relationship we observe experimentally between the rolling speed and its radius is well predicted by a balance of energies. By solving the Elastica on the curling piece, considering the centrifugal force due to rotation, we obtain a solution which represents a solitary traveling curvature wave reminiscent to propagating instabilities in mechanics.

An extension of this work, in progress in our laboratory, is to investigate the role of another source of dissipation such as local lubrication forces at low Reynolds numbers, which are important for the behavior of some of the microscopic systems cited in the introduction. Finally, the effect of non developable geometries like spherical surfaces presenting a local natural curvature could be explored in the future. In this case, large stretching deformations should generate several localized elastic defects such as d-cones and ridges which should interact and dominate curling dynamics. For large enough natural curvatures, cracks could be coupled to the curling front [79].

Beyond the fundamental aspects of this study, we think our work will contribute to a better understanding of curling, which currently provides a simple but powerful mean to build complex artificial nanotubes and microhelices for new applications in nanotechnologies [60, 14].

# Chapter 5

# Curling of naturally curved ribbons at low Reynolds number

In this chapter, we extend the study of curling ribbons to the low Reynolds number regime using Silicone oils as the outer fluid. This regime of movement mimics the same elasto-viscous conditions happening at the scale of iRBCs or polymersomes, helping to discriminate in the former model we developed in chapter 2 the effect of the geometry change of the pore size from that of viscous dissipation.

## 5.1 Some remarks on the experimental method

For the experiments described here, all the ribbons considered were made with PVC 100 $\mu$m thick and produced with $a_0 \approx 0.85$ cm ($a_0$ can not be much smaller if we still want to work with the approximation of constant natural curvature along the stripe). The outer medium corresponds to silicone oil of kinematic viscosity 12500 cSt (or dynamic viscosity $\eta_0 = 12.125$ Kg/s m). Because of the buoyancy force, the gravitational interactions are notoriously reduced. Actually, the effective elasto-gravitational length of the problem is $L_g = \left[\frac{Eh^3}{g(\sigma-\rho_0 h)}\right]^{1/3} \approx 21$ cm $\gg a_0$. In addition, we have performed curling experiments both, horizontally and vertically, without getting appreciable differences in the curling dynamics (see Fig.5.1). Because of simplicity in the manipulation, the rest of the experiments have been done only in a vertical version of the setup described in Fig.3.8 (see inset Fig.5.1).

For low Reynolds number, the speed of curling drops to the order of mm/s; then, depending on the viscosity of the outer medium and the natural radius, the complete curling of the ribbon can take more than 30 min. However, as has been mentioned in the chapter 3, a stressed ribbon (made with PP and PVC), due to creeping, starts to accumulate a considerable plastic deformation after 5 min. Therefore, in order to make

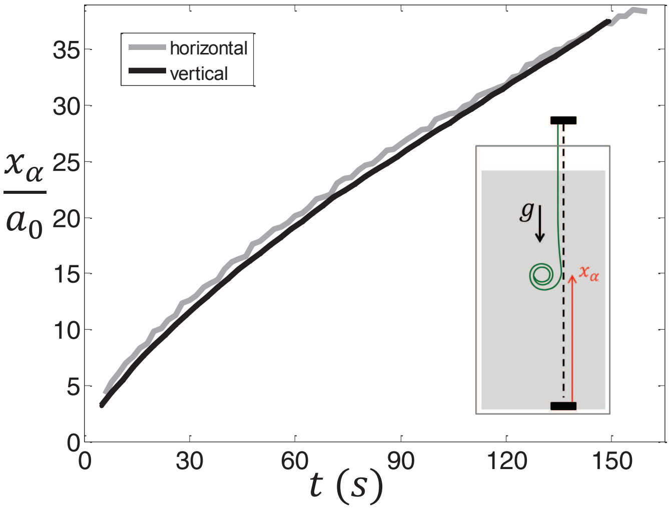

Figure 5.1: Position v/s time of curling experiments performed vertically and horizontally (the used ribbon was made with PVC100, $a_0 = 0.85$ cm and $W = 4$ cm). Inset: Schematic of the setup for vertical curling (the curling progresses against gravity).

experiments without relevant plastic effects, the values of $a_0$ and $\eta_0$ have been selected to have a full curling movement in less than 3 min but with a Reynolds number no larger than $10^{-2}$.

## 5.2 Experimental results

In Fig.5.2, the principal experimental results obtained from the observation of curling at low Reynolds number are presented. We have described the dynamics of curling by means of the frontal diameter, $D$ (see Fig.5.2A), the maximum height, $H$, and the curled position $x_\alpha$.

The first important experimental result is that the geometry of the curled material cannot be described with a compact cylinder as in the inertial case of chapter 4, and instead, the curling progresses forming a spiral whose size depends on time and on the width $W$ of the ribbon. Since, at short time scale, the time associated with the position has large uncertainty (due mainly to fluid disturbances during the release of the ribbon), the dynamical evolution has been shown as a function of the position, $x_\alpha$, instead of time. This allows to compare the implications of the width with better resolution.

From Fig.5.2B, we see that, before one turn ($x_\alpha/a_0 \lesssim 10$), the dynamics does not depend on $W$; however, when the curling propagates further, the size of the spiral starts to be sensitive to the width. $D$ reaches higher values for larger $W$ and the respective rates of growing decrease with $x_\alpha$. Moreover, the distance $H - D$ does not depend on $W$ and remains approximately constant ($H - D \approx 0.8a_0$).

In Fig.5.2C, the instantaneous speed of curling, $v = \dot{x}_\alpha$, associated with the positions $x_\alpha$ of the curves in Fig.5.2B, are presented as a ratio of the characteristic speed, $v_0 = \frac{B}{\eta_0 a_0^2} \approx 0.42$ m/s (which expresses the scaling of the balance between the stokes force, $\sim vW\eta_0$, and the driven force, $\sim \frac{BW}{a_0^2}$). The speed decreases with the position with a well defined width dependent power law. The movement is faster for smaller $W$. The observed power law for the speed, varies from $v \sim x_\alpha^{-0.40}$ (when $W \approx 2$ cm) to $v \sim x_\alpha^{-0.70}$ (when $W \approx 6$ cm). That means that the positions can be expressed as a power law in time: $x_\alpha \sim t^{0.71}$ (when $W \approx 2$ cm) and $x_\alpha \sim t^{0.59}$ (when $W \approx 6$ cm).

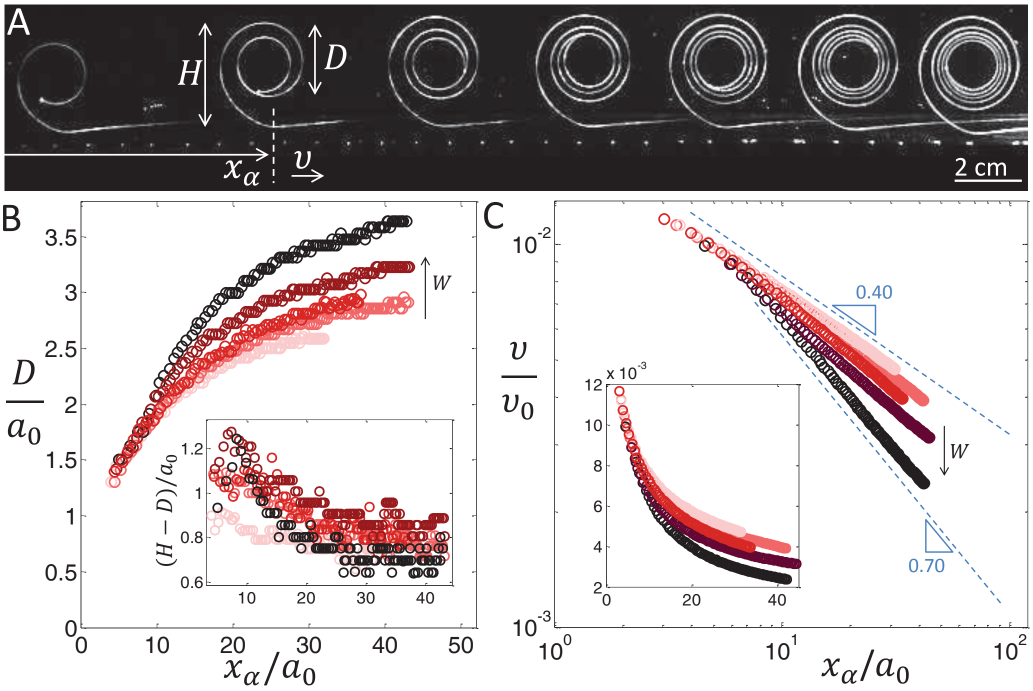

Figure 5.2: A.- Curling sequence (time lapse= 30s) for a ribbon (PVC100, $a_0 = 0.85$cm, $W = 6$ cm) in Silicone oil ($\eta_0 = 12500$ cSt). The curled position, $x_\alpha$, the frontal diameter, $D$, the height, $H$ and the speed of propagation, $v$, have been schematized. The experiment has been performed vertically (for simplicity, the picture is shown horizontally). B.- Normalized frontal diameter versus the normalized curling position for ribbons (PVC100 and $a_0 \approx 0.85$cm) with different $W$ (the arrow indicates the direction of increasing $W$, from up to down: $W = 2$cm; $W = 3$cm; $W = 4$cm; $W = 5$cm; $W = 6$cm) in Silicone oil ($\eta_0 = 12500$ cSt). The inset shows the respective values of the distance $(H - D)/a_0$. C.- Normalized curling speed versus the normalized curling position in Log plot for for the experiments of (B). Inset: Same data in linear representation.

## 5.3 Analysis of the viscous Dynamics

### 5.3.1 Stokes Drag

The set of experimental results described in the previous section give place to a curling process that is notoriously different than the winding process observed in bilayer ribbons in a viscous fluid [76]. In the bilayer winding, the speed of propagation decreases in very long distances because of the continuous growing of size of the roll. This corresponds to a geometrical effect of having a finite solid thickness, $h$, in the material: Since self-intersection is forbidden, the rate of released elastic energy in a compact winding changes slowly with the number of turns, $n$; therefore, the effects on the speed appear when the distance, $nh$, starts to be comparable with the spontaneous radius of the problem. In our case, the experiments has been performed always in a regime where $nh \ll a_0$, however, the hydrodynamic interaction generates an interlayer film of liquid which prevents the compact curling, and induces a premature fast growing of the spiral. One could think that, in analogy to the speed variation of the bilayer ribbon, the variation of the curling speed observed in our experiments, can be explained with a balance between the Stokes drag dissipation of the movement and the rate of elastic energy released (which is decreasing because the spiral is growing); however this approach underestimates the total power dissipated. In order to understand how this remark arises, first we take $2/D$ as the dominant curvature for the elastic energy variation, $\frac{\partial U_E}{\partial x_\alpha}$; then, similar to the Eq. 4.1, we have

$$\frac{\partial U_E}{\partial x_\alpha} = -\frac{BW\lambda^2}{2a_0^2}$$

, where $\lambda^2 = 4\frac{a_0}{D} - 4\left(\frac{a_0}{D}\right)^2 - \nu^2$. Now we approximate the drag force using the flow generated by a cylinder (of diameter $D$) rolling on a wall located to a distance $H - D$. The drag force is then [52].

$$F_d = 2\pi W\eta_0 v\sqrt{\frac{D}{H-D}}$$

Therefore, through the balance of powers, $vF_d + \frac{\partial U_E}{\partial x_\alpha}\dot{x}_\alpha = 0$, we get

$$\frac{v}{v_0} = \frac{\lambda^2}{4\pi}\sqrt{\frac{H-D}{D}} \tag{5.1}$$

In the inset of Fig.5.4, the quantity $\frac{\lambda^2}{4\pi}\sqrt{\frac{H-D}{D}}$ has been plotted using the experimental data of the ribbon with $W = 6$cm of the Fig.5.2. The average of the trend is approximately one order of magnitude larger than the experimental ratios of the speed, $v/v_0$, and it shows a clear underestimation of the viscous dissipation.

In Eq.5.1, the dissipation generated by the interlayer fluid film dynamics is missing. Actually, the local interlayer thickness decreases in time, giving a clear evidence of squeezing of liquid that has not been taken into account in this first approach. Since the spiral is smooth, the elastic pressure does not change strongly along the arc-length coordinate (the characteristic length of variation is $2\pi a_0$). Also, because $W \ll x_\alpha$, the natural hydrodynamic resistance for the flow of liquid in the $\hat{e}_2$ direction (see inset in Fig.5.3) is much smaller than in any other direction; thus, the squeezing must be interpreted as a side flow leaving the ribbon from its side.

### 5.3.2 Dissipation due to interlayer liquid flow

We describe the interlayer liquid dynamics using the intrinsic frame ($\hat{e}_1$, $\hat{e}_2$, $\hat{e}_3$), which has been sketched in the inset of Fig.5.3. The coordinates in the intrinsic frame are denoted respectively by ($r_1$, $r_2$, $r_3$), where $r_1 = s$ is the arc-length and $r_2$ is the position along the width measured from the center. In principle, for planar deformation we have $\frac{\partial h_c}{\partial r_2} = 0$ and, therefore, the elastic bending pressure depend only on $r_1$. In this context, one could think that the derivative of the fluid pressure, $\frac{\partial P}{\partial r_2}$, is zero; but this is correct only when a planar deformation takes place in a ribbon with no resistance to Gaussian curvature modifications (which can be interpreted as resistance to shear). Thanks to this Gaussian curvature stiffness, during curling, a solid ribbon is able to resist big gradients of pressure (along the width) without perpendicular bending modes developing. As mentioned before, the squeezing dynamics of smooth spirals must be reflected by a side flow of liquid, so the $r_2$-derivatives terms of the lubrication equation (Eq.3.20) are the dominant one, and the temporal derivative $\dot{h}_c$ gives

$$\dot{h}_c = \frac{1}{12\eta_0}\left[\frac{\partial}{\partial r_2}\left(h_c^3\frac{\partial P}{\partial r_2}\right)\right]$$

Then,

$$\frac{\partial P}{\partial r_2} = 12\eta_0\frac{\dot{h}_c}{h_c^3}r_2 \gg \frac{\partial P}{\partial r_1}$$

Combining Eq.3.17 and Eq.3.19 we express the density of power dissipated in terms of the gradient of pressure and, after integration in the thickness and the width, we have

$$d\Phi_S = 2\eta_0 W^3\frac{\dot{h}_c^2}{h_c^3}ds \tag{5.2}$$

, which is the local squeezing power dissipated in the infinitesimal arc-length $ds$. Thus, the total power dissipated corresponds to the integral of this relation along the liquid film, which has a length close to $x_\alpha - 2\pi a_0$. Since the derivative $\dot{h}_c$ can be written $\dot{x}_\alpha h'_c$ (the apostrophe denotes a derivative respectively to $s$), the total power dissipated is

$$\Phi_S = 2\pi\eta_0 W v^2 I \tag{5.3}$$

, where

$$I = \frac{W^2}{\pi}\int_0^{(x_\alpha - 2\pi a_0)} \frac{h_c'^2}{h_c^3} ds$$

, is a dimensionless function which contains the geometry of the spiral.

The new balance of powers is then given by $F_d v + \Phi_S + v\frac{\partial U_E}{\partial x_\alpha} = 0$, and the curling speed becomes

$$\frac{v}{v_0} = \frac{1}{4\pi}\frac{\lambda^2}{\sqrt{\frac{D}{H-D}} + I} \tag{5.4}$$

### 5.3.3 Phenomenological prediction of the speed

In order to compute the Eq.5.4 we must know some informations about how $h_c$ changes with $s$ and in time. We have extracted this information from image analysis of the thickness of the film layer in a typical movie of the experiments.

In Fig.5.3, experimental values of $h_c$ as a function of $s/a_0$ have been plotted for different positions, $x_\alpha$, during curling. For large $x_\alpha$, $h_c$ evolves from $H - D$ at $s = 0$ (in the point $\alpha$) to a value $\approx 0.2(H - D)$ when $s \approx x_\alpha - 2\pi a_0$ (we neglect the final part of the liquid film where $h_c$ goes rapidly to zero due to the self-contact produced in the point $\beta$). Surprisingly, the different curves of the plot can be described approximately with the same trend. Based in this observation, $h_c$ can be represented as an *ad hoc* function of $s$ and $x_\alpha$ (the problem is therefore not intrinsically dependent on time).

In order to estimate the contribution of the squeezing dissipation, we have fitted the data of Fig.5.3 with a unique Gaussian curve, $y = \frac{h_c}{H-D} = a + be^{-\gamma(s-s_0)^2}$ (dashed line in Fig.5.3), which is supposed to be compatible with the boundary conditions of the problem: $y = 1$ when $s = 0$ and $y \to a \neq 0$ when $s$ goes to infinity. Because the expression for the dissipation (Eq.5.2) diverges when $h_c \to 0$, the last condition ($y \to a \neq 0$) is indispensable to guarantee the curling movement at very long time scale. Noteworthy, the Gaussian curve, $y$, is not able to feet the data for small values of $x_\alpha$; on the other hand, the lubrication theory starts to be more suitable only when the spiral has, at least, two turns. Thus, we should not expect a good prediction of our model (Eq.5.4) when $x_\alpha \lesssim 13a_0$.

Using the fitted function, $y$, we have computed numerically the values of $I$ associated with the experimental data ($x_\alpha$, $D$, $H$). The results indicate that $I$ is dominant in front of the drag term, $\frac{D}{H-D}$, in the denominator of Eq.5.4. Actually, in Fig.5.4, the expected speed ratios (given by Eq.5.4) has been plotted together with the respective experimental curve of the curling speed and we see that the asymptotic value of the speed is well predicted by the model, while if $I = 0$, we recover the result of Eq.5.1, where the speed ratio appears overestimated by a factor 10 (see inset Fig.5.4).

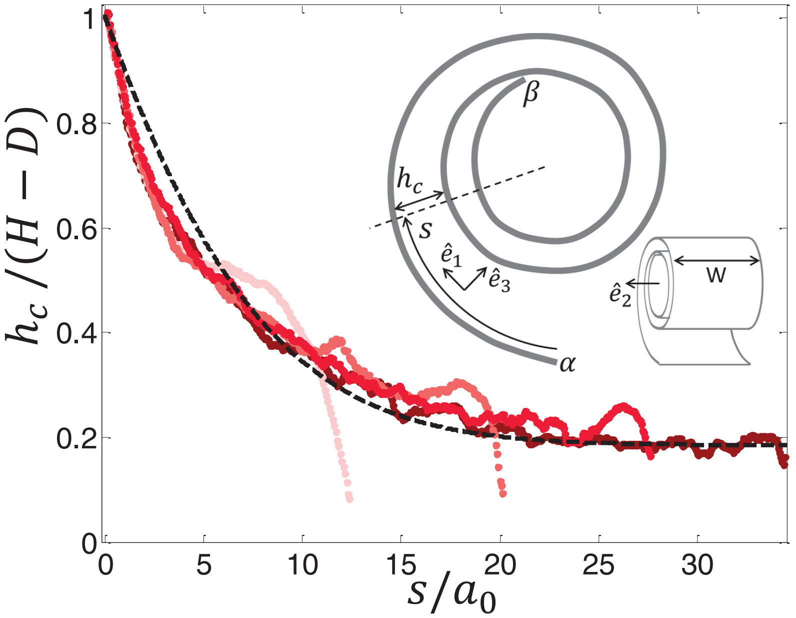

Figure 5.3: Normalized interlayer thickness $h_c/(H-D)$ as function of the arc-length coordinate for differents curling positions $x_\alpha$ (the different curves correspond to $x_\alpha/a_0 \approx$ 18; 26; 34; 42). The data come from the analysis of an experiment made with a ribbon of PVC100, $a_0 = 0.85$cm and $W = 6$ cm. The dashed line represents the curve: $h_c/(H-D) = 0.185 + 3.15\exp\{-0.0032(s/a_0 + 20.05)^2\}$.

## 5.4 Discussion

The good agreement between the asymptotic value of the experimental measurement of the speed and the one predicted by the phenomenological model, is a clear evidence that the interlayer lubrication forces are the dominant non conservative interactions during curling at low Reynolds number.

This result has a very important implications in the axisymmetric curling studied in chapter 2, where, using a model without interlayer viscous friction, the surface viscosity, $\eta_s$, has been established with a high value. In the axisymmetric case, although an interlayer liquid can not escape from the rim (spiral of revolution) with a lateral flow, the progressing of the curling, itself, forces a lateral redistribution of liquid (otherwise the conservation of interlayer volume can not be satisfied). Therefore, the same principles used in the

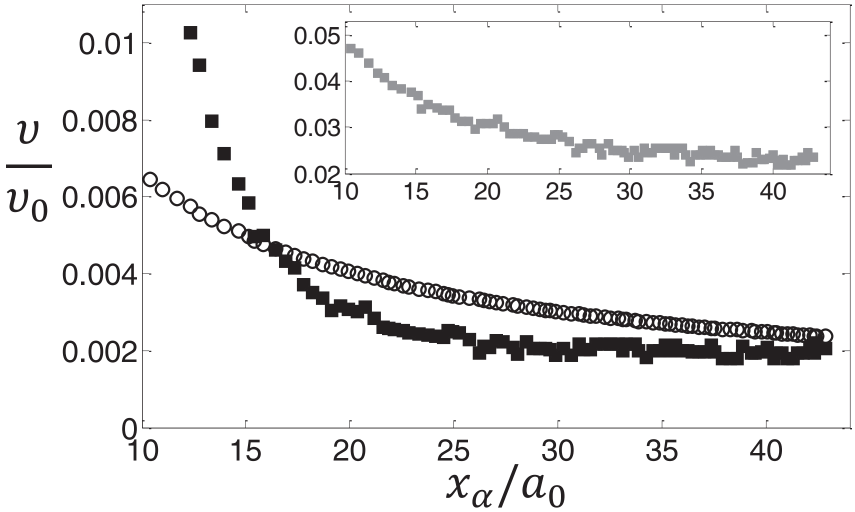

Figure 5.4: Curling speed ratio vs $x_\alpha/a_0$: (○) reproduction of the experimental data in Fig.5.2C for $W = 6$ cm and (■) numerical estimation of Eq.5.4. Inset: numerical estimation of Eq.5.1.

approach for the squeezing in ribbons could be applied in the model for axisymmetric curling. The consequences of such argument are currently under investigation.

Compared to models of the cylindrical curling of straight ribbons as the one developed in [48, 1], the temporal slowing down deduced from their model can be attributed to the linear increase in size of the curled ribbon due to the finite thickness of the material and the assumption of compact curling. However, in our observations, the spiral size $D$ of the curling ribbon increases in time in a non linear fashion, because of the continuous draining of fluids laterally, due to the elastic strangulation of the ribbon, and which dominates the dynamics over large scale friction.

## 5.5 Conclusions

In conclusions, in this chapter, we showed that, curling at low Reynolds number is controlled by two viscous dissipations in the case of ribbons: the large scale drag, due to the displacement of the fluid when the ribbon curls on itself and the local viscous friction generated by the bending forces that squeeze out laterally the interstitial fluid, by an elastic "strangulation".

While our basic approach gives the good approximation of the curling speed, several points still remain unclear and worth development. For instance, what determines the longitudinal variation of $h_c(s)$ along the spiral ? Why the law is independent in time and most intriguingly, what controls the final power laws we observe for $v/v_0$ as a function of $W$? In order to answer these questions, a more complete treatment of the elasto-viscous interaction is necessary but which could not be treated during the time course of the thesis.

# Chapter 6

# Conclusions and Perspectives

## 6.1 Conclusions

In this thesis, theoretical approaches and macroscopic experiments on elastic ribbons have been coupled to decipher the dynamics of curling associated to opened bio-membranes. The principal conclusions are separated in 3 different points:

### 6.1.1 Geometric implications of axisymmetric curling in biomembranes

When a spontaneous curvature is present in the membrane, the stability of a pore depends strongly on its size. In particular, the line tension $\gamma$ of the free edge always dominates when the opening angle is sufficiently small. The critical spontaneous curvature for curling is not well defined through a mechanical equilibrium in the initial configuration of the pore (after nucleation): because of the cycloidal nature of curling deformation, an energy barrier could appear in an early stage of the dynamics, and then, block the curling progressing. The existence of an energy barrier for curling, allows the possibility of a static equilibrium of the pore. A critical spontaneous curvature must be defined as the curvature at which the energy barrier associated to the intrinsic cycloidal motion of the curling is crossed.

Since a biomembrane is essentially a two-dimensional fluid, when an axisymmetric curling propagates down the spherical body, it involves an important redistribution of surface. This redistribution (or in plane flow) represents an important source of dissipation that had not been considered in previous works. Also, under the approximation of very high spontaneous curvature, any shear resistance $G$ of the membrane becomes dominant only when the curling dynamics occurs on a spherical object (vesicle or cell) with radius

$R_0$ much bigger than the length $\gamma/G$.

### 6.1.2 Geometric implications of curling in naturally curved ribbons

The Poisson's ratio of a naturally curved ribbon generates a tendency to localize the planar bending deformations. This has a strong effect in the selection of the bending modes during curling. The localization phenomenon is out of the Euler Elastica description, therefore, by definition, it can not be defined for a pure unidimensional rod. Actually, the mechanical conditions of such localizations have been used to find a rod-ribbon transition: ribbons behave like perfect rods only when $\frac{W^2}{ha_0} \lesssim 1$ ($W$ is the width of the ribbon, $h$ is the thickness and $a_0$ the natural radius). For high Reynolds number and small Cauchy number, curling deformation for $\frac{W^2}{ha_0} \gtrsim 200$, leads to a rolling regime, where the speed of propagation is constant. The relationship we observe experimentally between the rolling speed and its radius is well predicted by a balance of energies. By solving the Elastica on the curling piece, considering the centrifugal force due to rotation, we obtain a solution which represents a solitary traveling curvature wave reminiscent to propagating instabilities in mechanics.

### 6.1.3 Drag and interlayer fluid friction coupled to curling

From experiments on naturally curved ribbons in viscous oil and at low Reynolds number, we showed that the interlayer fluid friction dominates the shape of the observed spiral and the power dissipated during curling. This counterintuitive result, should have very significant implications in the modeling of curling in axisymmetric membranes ignored up to now.

## 6.2 Perspectives

Since the interlayer fluid interactions can not be neglected during curling at low Reynolds number, the models of curling in biomembranes must be revised in the future. In axisymmetric geometry, although an interlayer liquid can not escape from the rim (spiral of revolution) with a lateral flow as observed for ribbons, curling propagation should force a lateral redistribution of liquid due to the conservation of interlayer volume. Therefore, the same principles used for ribbons could be applied in the model for axisymmetric curling. Also the dynamic solution of axisymmetric curling can be improved by using the numerical computations of the potential energies instead of the analytical approximations.

In all the works of curling dynamics of biomembranes (including this thesis), the driven potential energy has been written using a pure *spontaneous curvature model*, where the spontaneous curvature is supposed to reflect the asymmetry in the membrane. However, a coupling between curvature and density of the leaflets of the membranes could generate an extra elastic term. Actually, the so-called Area-difference-Elasticity model has been used to explain successfully typical phenomena observed in shapes transformations of vesicles and RBC [53, 75]. A further study about the consequences on the application of this model to the curling dynamics is pending.

Finally, in the context of the curling of naturally curved ribbons at low Reynolds number, the performed approach gives the good approximation of the curling speed, but several points still remain unclear and worth development.

For instance, how can we predict the general geometry of the spiral? Why the experimental law of the spiral shape is independent in time and what controls the final power laws we observed for $v/v_0$ as a function of $W$? In order to answer these questions, a more complete treatment of the elasto-viscous interaction is necessary.

# Appendix A

# Geometry and elasticity

## A.1 Infinitesimal variation of volume and surface

The local relative variation of volume due to an arbitrary small deformation is

$$\frac{dr_1' dr_2' dr_3' - dr_1 dr_2 dr_3}{dr_1 dr_2 dr_3} = \varepsilon_2 + \varepsilon_1 + \varepsilon_3$$

Furthermore,

$$\varepsilon_1 \varepsilon_2 = \left( \frac{dr_1' - dr_1}{dr_1} \right) \left( \frac{dr_2' - dr_2}{dr_2} \right) = -\varepsilon_1 - \varepsilon_2 + \mathcal{E}_{A_3} \tag{A.1}$$

Where $\mathcal{E}_{A_3} = \frac{dr_1' dr_2'}{dr_1 dr_2} - 1$ is the relative surface expansion of the infinitesimal planes that are perpendicular to the axis $\hat{e}_3$. Then, generalizing the notation of equation A.1, the relative variation of the total surface area $dA$ of the infinitesimal enclosed volume is

$$\mathcal{E}_A = \frac{dr_1' dr_2' + dr_1' dr_3' + dr_2' dr_3'}{dr_1 dr_2 + dr_1 dr_3 + dr_2 dr_3} - 1 = \frac{\mathcal{E}_{A_1} dr_2 dr_3 + \mathcal{E}_{A_2} dr_1 dr_3 + \mathcal{E}_{A_3} dr_1 dr_2}{dr_1 dr_2 + dr_1 dr_3 + dr_2 dr_3}$$

, however, each infinitesimal surface $dr_1 dr_2$, $dr_1 dr_3$ and $dr_2 dr_3$, represents 1/6 of the total surface $dA$ of the enclosed volume, therefore $\mathcal{E}_A(\varepsilon) = \frac{1}{3}(\mathcal{E}_{A_1} + \mathcal{E}_{A_2} + \mathcal{E}_{A_3})$. Finally,

$$\mathcal{E}_A = \frac{1}{6} \left[ (\varepsilon_1 + \varepsilon_2 + \varepsilon_3)^2 - (\varepsilon_1^2 + \varepsilon_2^2 + \varepsilon_3^2) + 4(\varepsilon_1 + \varepsilon_2 + \varepsilon_3) \right] \tag{A.2}$$

The relative variation of surface area of a pure compression (where $\varepsilon_1 = \varepsilon_2 = \varepsilon_3$) is $\mathcal{E}_A = \frac{1}{6} \left[ \frac{2}{3}(\varepsilon_1 + \varepsilon_2 + \varepsilon_3)^2 + 4(\varepsilon_1 + \varepsilon_2 + \varepsilon_3) \right]$. Therefore the contribution, of an inhomogeneous dilation, in the increment of enclosed surface area, is obtained by substracting the previous expression, with Eq.A.2. The result is

$$-\frac{1}{6} \left[ \varepsilon_1^2 + \varepsilon_2^2 + \varepsilon_3^2 - \frac{1}{3}(\varepsilon_1 + \varepsilon_2 + \varepsilon_3)^2 \right]$$

## A.2 Kirchhoff Equation for small deflections

In absence of external forces the Eq.3.7 gives

$$\frac{\partial \mathbf{F}}{\partial s} \approx \varrho(\ddot{\mathbf{r}} \cdot \hat{n})\hat{n}$$

Also,

$$\frac{\partial}{\partial s}(\hat{t} \times \mathbf{F}) \approx \hat{t} \times \frac{\partial \mathbf{F}}{\partial s} = \varrho(\ddot{\mathbf{r}} \cdot \hat{n})(\hat{t} \times \hat{n})$$

, and the derivative of Eq.3.8 leads to

$$BW\frac{\partial^2 \kappa}{\partial s^2} - \varrho(\ddot{\mathbf{r}} \cdot \hat{n}) = \frac{\varrho h}{12}\ddot{\kappa}$$

, but from Eq.3.9 and Eq.3.10

$$\frac{\partial^2}{\partial s^2}(\ddot{\mathbf{r}} \cdot \hat{n}) \approx \hat{n}\frac{\partial^2 \ddot{\mathbf{r}}}{\partial s^2} \approx -\ddot{\kappa}$$

Therefore,

$$BW\frac{\partial^4 \kappa}{\partial s^4} - \varrho\ddot{\kappa} = \frac{\varrho h}{12}\frac{\partial^2 \ddot{\kappa}}{\partial s^2}$$

## A.3 Planar Bending Pressure for small deflections

Considering an external pressure $P$ on the surface of a beam, the external force per unit length is $\mathbf{K} = PW\hat{n}$, where $W$ is the width of the beam and $\hat{n}$ is the unitary normal vector. In absence of inertia the Eq.3.7 gives

$$\frac{\partial \mathbf{F}}{\partial s} = PW\hat{n}$$

Also, for small deflections

$$\frac{\partial}{\partial s}(\hat{t} \times \mathbf{F}) \approx \hat{t} \times \frac{\partial \mathbf{F}}{\partial s} = (\hat{t} \times \hat{n})PW$$

, and the derivative of Eq.3.8 leads to

$$B\frac{\partial^2 \kappa}{\partial s^2} = P$$

, but for small deflections the curvature is approximately the second derivative of the height $Z$ of the deflection respect to the horizontal coordinate $r_1$, therefore,

$$B\frac{\partial^4 Z}{\partial r_1^4} = P$$

# Appendix B

# Static equilibrium in curling and calculus of the critical $a_0^*$

## B.1 The critical natural radius $a_0^*$

### B.1.1 The Heavy Elastica Equation

We are interested to find the differential equation that describes the shape of a ribbon that bends with planar deformations under its own weight. In Fig.B.1, a schematic of the problem is presented: one end of the ribbon is immobilized by fixing its local tangential vector and the other extremity is left free. We define the natural radius of curvature $a_0$, the tangential angle $\theta$ and the arc length position $S$, which runs from zero to the full length $S_\beta$ of the material.

For static equilibrium, the equations of force and torque are given by:

$$\partial_S \mathbf{F} + \mathbf{K} = 0 \tag{B.1}$$

and

$$\partial_S \mathbf{M} + \mathbf{t} \times \mathbf{F} = 0 \tag{B.2}$$

where $\mathbf{K}$ is the external force per unit of area; $\mathbf{F}$ is the internal force resultant on the cross-section and $\mathbf{M}$ is the torque resultant per unit length. For planar deformations, the torques are connected with the curvature by: $\mathbf{M} = -B\left(\kappa_0 - \kappa\right)\mathbf{e}_3$, where $B$ is the bending stiffness, $\kappa_0 = 1/a_0$ is the natural curvature and $\kappa = \partial_S \theta = \theta'$ is the local curvature.

Solving Eq.B.1 for the gravitational interaction $\mathbf{K} = -g\sigma\mathbf{e}_2$ ($g$ is the gravitational aceleration and $\sigma$ the surface density) we get $\mathbf{F} = g\sigma\left(S - S_\beta\right)\mathbf{e}_2$, and then, by Eq.B.2, the general equation for static equilibrium is found:

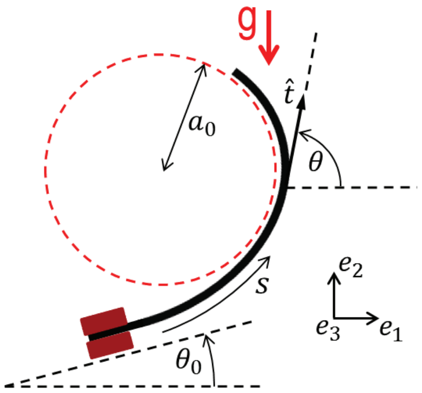

Figure B.1: Scheme of the static configuration of a ribbon of natural radius $a_0$ that is deformed by its own weight.

$$\theta'' + \frac{g\sigma}{B}\left(S - S_\beta\right)\cos\theta = 0 \tag{B.3}$$

To non dimensionalize, we introduce the parameter $\chi = S/S_\beta$, then eq.B.3 becomes

$$\frac{d^2\theta\left(\chi\right)}{d\chi^2} - \frac{\left(1-\chi\right)}{b}\cos\theta\left(\chi\right) = 0 \tag{B.4}$$

where $b = \frac{B}{\sigma g S_\beta^3}$. Because of the origin of the problem, this equation must be subjected to the boundary conditions: $\theta\left(0\right) = \theta_0$ and $\frac{d\theta}{d\chi}\left(1\right) = \frac{S_\beta}{a_0}$.

### B.1.2 Numerical solution

When the angle $\theta\left(\chi\right)$ and its derivative $\frac{d\theta(\chi)}{d\chi}$ in $\chi = 0$ are imposed, using finite differences method we can easily solve the Eq.B.4 numerically. First we aproximate the second derivative,

$$\frac{d^2\theta}{d\chi^2} \approx \frac{\theta\left(\chi+\Delta\chi\right) - 2\theta\left(\chi\right) + \theta\left(\chi-\Delta\chi\right)}{\Delta\chi^2}$$

and discretize the domain of the solution: $\chi \to \chi_n = n\Delta\chi$. Now, considering $\theta\left(\chi\right) \to \theta_n = \theta\left(\chi_n\right)$ and $\Delta\chi = 1/N$ (where $N$ is the number of intervals of the domain), we get the following recursive formula

$$\theta_{n+1} = \frac{1}{b}\left(\frac{1}{N^2} - \frac{n}{N^3}\right)\cos\theta_n + 2\theta_n - \theta_{n-1} \tag{B.5}$$

where $n = 1, 2, 3, ..., N-1$. In order to find the complete numerical solution, we start with the initial values, $\theta_0$ and $\theta_1$, that are given by the boundary conditions of the problem.

For the problem of the equilibrium shape of the frustrated curling, the boundary conditions for rods are $\theta\left(0\right) = \theta_0 = 0$ and $\frac{d\theta(0)}{d\chi} = 0 \Rightarrow \theta_1 = 0$. Thus, with the recursive formula, for each number $b$, we have access to the entire angular variation of the rod, especially at the free boundary, the curvature is $\frac{d\theta(1)}{d\chi} = \frac{S_\beta}{a_0}$ (which is also the dimensionless natural curvature). In Fig.B.2 we have plotted the numerical solutions for the parameter $1/b$ associated with the normalized curvature $S_\beta/a_0$, the graph shows that $1/b$ can not be higher than 45.63, otherwise $S_\beta/a_0$ becomes negative and the solution is not more compatible with the conditions of the problem.

For ribbons, the problem is more subtle because the curvature at $\chi = 0$ is given by $\frac{d\theta(0)}{d\chi} = \nu\frac{S_\beta}{a_0}$ that must be also compatible with the boundary condition at the free end, which implies that $\theta_1$, $\theta_{N-1}$ and $\theta_N$ are explicitly connected:

$$\theta_1 = (\theta_N - \theta_{N-1})\,\nu$$

Knowing $\nu$, we run the iterative formula of Eq.B.5, performing a searching loop where, for a specific $b$, the initial estimate of $\theta_1$ will be given by the dimensionless natural curvature of the associated rod solution. Then, writing the curvature at the free end as $\kappa_N(b, \theta_1)$, the first iterative solution will be written $\theta_1^{(1)} = \frac{\nu}{N}\kappa_N(b, \theta_1 = 0)$. Using this same idea we can produce a better estimate $\theta_1^{(2)} = \frac{\nu}{N}\kappa_N\left(b, \theta_1^{(1)}\right)$. Thus, $\theta_1^{(i)}$ can be improved for any required accuracy using the algorithm:

$$\theta_1^{(i+1)} = \frac{\nu}{N}\kappa_N\left(b, \theta_1^{(i)}\right)$$

For a ribbon of $\nu = 0.38$, the Fig.B.3 also shows the relation between $1/b$ and $S_\beta/a_0$ obtained by means of the numerical solution.

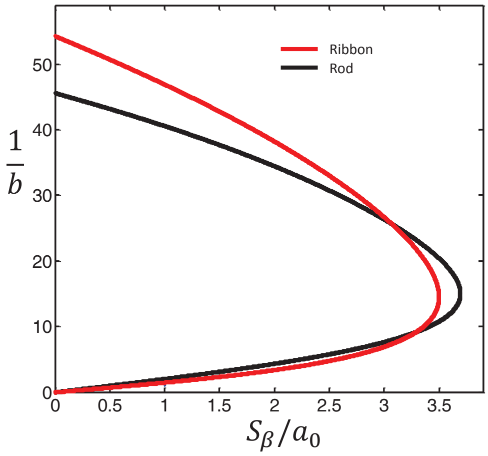

Figure B.2: Numerical Solution (with finite differences method) of the relation between the heavy-elastica constant $1/b$ and its associated boundary condition $S_\beta/a_0$ for the problem of the gravitational barrier for curling. The red line is associated with a ribbon with $\nu = 0.38$.

### B.1.3 The limit for static equilibrium

When $a_0$ is lower than the critical value $a_0^*$, the stored elastic energy of the ribbon is higher than its gravitational potential energy and curling starts. However, when $a_0 \gtrsim a_0^*$, the ribbon adopts a static configuration that we characterize by two variables: the height $Y_\beta$ of the free end $\beta$ of the ribbon, and the curvilinear length $S_\beta$ between the contact with the substrate, $\alpha$, and $\beta$ (see picture in Fig.B.3B).

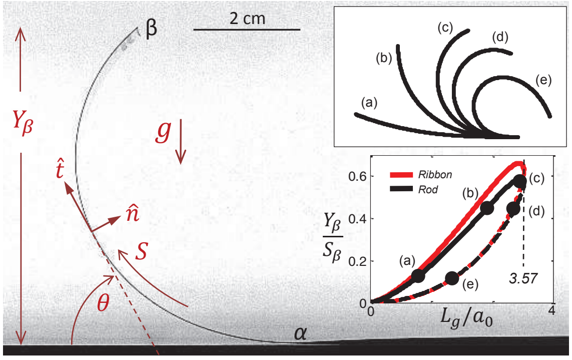

Figure B.3: (A) Image of an unwound ribbon of natural radius $a_0$. (B) Image of a ribbon in static equilibrium with gravity (PVC film 100 $\mu$m thick, $a_0 = 4.0 \pm 0.1$ cm and $W = 3.5$ cm). Upper inset: Numerical solutions for static equilibrium shapes obtained using Eq.B.4. Positions are normalized by $S_\beta$. Lower inset: Equilibrium diagram $Y_\beta/S_\beta$ versus $L_g/a_0$ ($a_0 > 0.28L_g$). Two solutions are represented one stable, one unstable (dashed line) for each $L_g/a_0$ (red line obtained for a ribbon with $\nu = 0.4$). On the plot, letters indicate the shape obtained by the numerical solution.

To deduce the value of $a_0^*$ from the parameters of the static problem, we used Eq.B.4.

For an initially horizontal ribbon, using $Y_\beta/S_\beta = \int_0^1 \sin(\theta) d\chi$, a first integration of Eq.B.4 leads to $Y_\beta/S_\beta = \frac{b}{2}[(S_\beta/a_0)^2 - \theta'(0)^2]$. Because of the $\Gamma$-region, the longitudinal curvature at the point $\alpha$ is given by $a_0/\nu$ and $\theta'(0) = \nu S_\beta/a_0$. The height of the free border is then given simply by $Y_\beta = L_g^3/24a_0^2$, where we define the elasto-gravitational length $L_g = (\frac{Eh^3}{g\sigma})^{1/3}$. $Y_\beta$ increases with the square of the natural curvature until the critical situation at which the curling proceeds.

We report in the upper inset of Fig.B.3, different shapes we obtain from the numerical solution of Eq.B.4. We report also in the lower inset of Fig.B.3, the stability diagram, where $Y_\beta/S_\beta = \frac{b}{2}(1-\nu^2)\theta'(1)^2$ and $\frac{L_g}{a_0} = [12b(1-\nu^2)]^{\frac{1}{3}}\theta'(1)$ are written in terms of the parameters $(b, S_\beta/a_0)$ plotted in Fig.B.3. For each value of $Y_\beta/S_\beta$, two solutions are found for two different $L_g/a_0$: one stable (upper solid line) and one unstable (lower dashed line). No more static solutions are found when $L_g/a_0^* \gtrsim 3.57$.

The critical natural radius $a_0^*$ varies slowly with $\nu$. In the range, $0.3 < \nu < 0.5$, $a_0^*$ varies less than 1%. Thus, curling occurs, in general, only when $a_0 \lesssim 0.28L_g = a_0^*$. For

PVC and PP ribbons, we find $a_0^*$ equal to $3.9 \pm 0.1$ cm and $3.8 \pm 0.2$ cm respectively, in good agreement with our observations.

# List of Figures

# Bibliography

[1] Abkarian, M., G. Massiera, L. Berry, M. Roques, and C. Braun-Breton, *A novel mechanism for egress of malarial parasites from red blood cells*, Blood **117**, 4118 (2011). 3, 4, 8, 9, 10, 11, 12, 13, 17, 19, 23, 24, 34, 35, 36, 38, 80

[2] Audoly, B. and S. Neukirch, *Fragmentation of Rods by Cascading Cracks: Why Spaghetti Does Not Break in Half*, Phys. Rev. Lett. **95**, 095505 (2005). 44, 61

[3] Blisnick, T., M. Betoulle, M. Barale, J. Uzureau, P. Berry, L. Desroses, S. Fujioka, H. Mattei, and C. Braun-Breton, *Pfsbp1, a Maurer's cleft Plasmodium falciparum protein, is associated with the erythrocyte skeleton*, Mol. Biochem. Parasitol. **111**, 107 (2000). 12, 24

[4] Blisnick, T., B. Morales, E. Maria, J.-C. Barale, P. Uzureau, L. Berry, S. Desroses, H. Fujioka, D. Mattei, and C. Braun-Breton, *Pfsbp 1, a Maurer's cleft Plasmodium falciparum protein, is associated with the erythrocyte skeleton*, Molecular and biochemical parasitology **111**, 107 (2000). 17

[5] Boal, D. and D. Boal, *Mechanics of the Cell* (Cambridge University Press, ADDRESS, 2012). 14

[6] Boussinesq, J., *Application des potentiels à l'étude de l'équilibre et du mouvement des solides élastiques* (Gauthier-Villars, Paris, 1885). 44, 61

[7] Brochard-Wyart, F., P. de Gennes, and O. Sandre, *Transient pores in stretched membranes: role of the leak-out*, Physica A **278**, 32 (2000). 13

[8] Buchak, P., C. Eloy, and P. Reis, *The Clapping Book: wind-driven oscillations in a stack of elastic sheets*, Phys. Rev. Lett. **105**, 194301 (2010). 45

[9] Callan-Jones, A., P.-T. Brun, and B. Audoly, *Self-similar curling of a naturally curved elastica*, Phys. Rev. Lett. **108**, 174302 (2012). 5

[10] Callan-Jones, A., P.-T. Brun, and B. Audoly, *Self-similar curling of a naturally curved elastica*, Phys. Rev. Lett. **108**, 174302 (2012). 13, 57, 58, 70

[11] Chandramohanadas, R., P. Davis, D. Beiting, M. Harbut, C. Darling, G. Velmourougane, M. Lee, P. Greer, D. Roos, and D. Greenbaum, *Apicomplexan parasites co-opt host calpains to facilitate their escape from infected cells*, Science **324**, 794 (2009). 17

[12] Chandramohanadas, R., Y. Park, L. Lui, A. Li, D. Quinn, K. Liew, M. Diez-Silva, Y. Sung, M. Dao, C. Lim, P. Greer, D. Roos, and D. Greenbaum, *Biophysics of malarial parasite exit from infected erythrocytes*, PloS one **6**, e20869 (2011). 17

[13] Chater, E. and J. Hutchinson, *On the Propagation of Bulges and Buckles*, J. Appl. Mech. **51**, 269 (1984). 61

[14] Cho, A., *Nanotechnology - Pretty as you please, curling films turn themselves into nanodevices*, Science **313**, 164 (2006). 71

[15] Cicuta, P., S. Keller, and S. Veatch, *Diffusion of liquid domains in lipid bilayer membranes*, J. Phys. Chem. B **111**, 3328 (2007). 13

[16] Cooke, B., N. Mohandas, and R. Coppel, *Malaria and the red blood cell membrane*, Semin. Hematol. **41**, 173 (2004). 12, 24

[17] Dhawan, S., M. Dua, A. Chishti, and M. Hanspal, *Ankyrin peptide blocks falcipain-2-mediated malaria parasite release from red blood cells*, J. Biol. Chem. **278**, 30180 (2003). 17

[18] Dimova, R., S. Aranda, N. Bezlyepkina, V. Nikolov, K. Riske, and R. Lipowsky, *A practical guide to giant vesicles. Probing the membrane nano regime via optical microscopy*, J. Phys.: Condens. Matter **18**, S1151 (2006). 7, 13

[19] Dimova, R., C. Dietrich, A. Hadjiisky, K. Danov, and B. Pouligny, *Falling ball viscosimetry of giant vesicle membranes: finite-size effects*, Eur. Phys. J. B **12**, 589 (1999). 13

[20] Dimova, R., C. Dietrich, A. Hadjiisky, K. Danov, and B. Pouligny, *Falling ball viscosimetry of giant vesicle membranes: finite-size effects*, Euro. Phys. J. B **12**, 589 (1999). 36

[21] Discher, D. and A. Eisenberg, *Polymer vesicles*, Science **297**, 967 (2002). 7

[22] Dvorak, J., L. Miller, W. Whitehouse, and T. Shiroishi, *Invasion of erythrocytes by malaria merozoites*, Science **187**, 748 (1975). 8

[23] Evans, E. and W. Rawicz, *Elasticity of "fuzzy" biomembranes*, Phys. Rev. Lett. **79**, 2379 (1997). 17

[24] Evans, E. and R. Skalak, *Mechanics and thermodynamics of biomembranes*, (1980). 16

[25] Forterre, Y., J. Skotheim, J. Dumais, and L. Mahadevan, *How the Venus flytrap snaps*, Nature **433**, 421 (2005). 2

[26] Gerbode, S., J. Puzey, A. McCormick, and L. Mahadevan, *How the cucumber tendril coils and overwinds*, Science **337**, 1087 (2012). 2

[27] Gilson, P. and B. Crabb, *Morphology and kinetics of the three distinct phases of red blood cell invasion by Plasmodium falciparum merozoites*, Int J. Parasitol. **39**, 91 (2009). 8

[28] Glushakova, S., G. Humphrey, E. Leikina, A. Balaban, J. Miller, and J. Zimmerberg, *New stages in the program of malaria parasite egress imaged in normal and sickle erythrocytes*, Curr. Biol. **20**, 1117 (2010). 8

[29] Glushakova, S., D. Yin, T. Li, and J. Zimmerberg, *Membrane transformation during malaria parasite release from human red blood cells*, Curr. Biol. **15**, 1645 (2005). 8, 19

[30] Gupta, G. and G. Mishra, *Transbilayer phospholipid asymmetry in Plasmodium knowlesi-infected host cell membrane*, Science **212**, 1047 (1981). 17

[31] Heinrich, V., K. Ritchie, N. Mohandas, and E. Evans, *Elastic thickness compressibility of the red cell membrane*, Biophys. J. **81**, 1452 (2001). 11, 14

[32] Heinrich, V., K. Ritchie, N. Mohandas, and E. Evans, *Elastic thickness compressibilty of the red cell membrane*, Biophys. J. **81**, 1452 (2001). 34

[33] Henon, S., G. Lenormand, A. Richert, and F. Gallet, *A new determination of the shear modulus of the human erythrocyte membrane using optical tweezers*, Biophys. J. **76**, 1145 (1999). 16

[34] Hochmuth, R., P. Worthy, and E. Evans, *Red cell extensional recovery and the determination of membrane viscosity*, Biophys. J. **26**, 101 (1979). 36

[35] Hu, M., D. deJong, S. Marrink, and M. Deserno, *Gaussian curvature elasticity determined from global shape transformations and local stress distributions: a comparative study using the MARTINI model*, Faraday Discuss. **161**, 365 (2013). 16

[36] Hutchinson, J. and K. Neale, *Neck propagation*, J. Mech. Phys. Solids **31**, 405 (1983). 61

[37] H.W. Krenn, H. W., *Feeding mechanisms of adult Lepidoptera: structure, function, and evolution of the mouthparts*, Ann. Rev. Entomol. **55**, 307 (2010). 2

[38] Hwang, W. and R. Waugh, *Energy of dissociation of lipid bilayer from the membrane skeleton of red blood cells*, Biophys. J. **72**, 2669 (1997). 16

[39] Kabaso, D., R. Shlomovitz, T. Auth, V. Lew, and N. Gov, *Curling and local shape changes of red blood cell membranes driven by cytoskeletal reorganization*, Biophys. J. **99**, 808 (2010). 5

[40] Karatekin, E., O. Sandre, H. Guitouni, N. Borghi, P.-H. Puech, and F. Brochard-Wyart, *Cascades of transient pores in giant vesicles: line tension and transport*, Biophys. J. **84**, 1734 (2003). 19

[41] Kyriakides, S., *Propagating instabilities in structures*, Adv. Appl. Mech. **30**, 67 (1994). 61

[42] Landau and Lifshitz, *Theory of elasticity* (Elsevier Ltd, Oxford, UK, 1886). 51, 52

[43] Landau, L. and E. Lifshitz, *Fluid Mechanics: Vol. 6 of Course Of Theoretical Physics* (Butterworth-Heinemann, ADDRESS, 1987). 31, 47

[44] Landau, L. and E. Lifshitz, *Theory of Elasticity: Vol. 7 of Course of Theoretical Physics* (Butterworth-Heinemann, ADDRESS, 1987). 40

[45] Lanzer, M., H. Wickert, G. Krohne, L. Vincensini, and C. Braun-Breton, *Maurer's clefts: A novel multi-functional organelle in the cytoplasm of Plasmodium falciparum-infected erythrocytes*, Int. J. Parasitol. **36**, 23 (2006). 17

[46] Lanzer, M., H. Wickert, G. Krohne, L. Vincensini, and C. Breton, *Maurer's clefts: a novel multifunctional organelle in the cytoplasm of Plasmodium falciparum-infected erythrocytes*, Int. J. Parasitol. **36**, 23 (2006). 12, 24

[47] Love, A., *A treatise on the mathematical theory of elasticity* (Cambridge University Press, ADDRESS, 2013). 40

[48] Mabrouk, E., D. Cuvelier, F. Brochard-Wyart, P. Nassoy, and M. Li, *Bursting of sensitive polymersomes induced by curling*, Proc. Natl. Acad. Sci. USA **106**, 7294 (2009). 3, 7, 8, 9, 11, 12, 23, 80

[49] Mabrouk, E., D. Cuvelier, F. Brochard-Wyart, P. Nassoy, and M. Li, *Bursting of sensitive polymersomes induced by curling*, Proc. Natl. Acad. Sci. USA **106**, 7294 (2009). 3, 19, 22, 35

[50] Maier, A. G., B. Cooke, A. Cowman, and L. Tilley, *Malaria parasite proteins that remodel the host erythrocyte*, Nature Rev. Microbiol. **7**, 341 (2009). 16, 18

[51] Mandelkow, E.-M., E. Mandelkow, and R. Milligan, *Microtubule dynamics and microtubule caps: a time-resolved cryo-electron microscopy study.*, J. Cell Biol. **114**, 977 (1991). 2, 3

[52] Merlen, A. and C. Frankiewicz, *Cylinder rolling on a wall at low Reynolds numbers*, J. Fluid Mech. **685**, 461–494 (2011). 76

[53] Miao, L., B. Fourcade, M. Rao, M. Wortis, and R. Zia, *Equilibrium budding and vesiculation in the curvature model of fluid lipid vesicles*, Phys. Rev. A **43**, 6843 (1991). 85

[54] Mills, J. P., M. Diez-Silva, D. J. Quinn, M. Dao, M. J. Lang, K. S. W. Tan, C. T. Lim, G. Milon, P. H. David, O. Mercereau-Puijalon, S. Bonnefoy, and S. Suresh, *Effect of plasmodial RESA protein on deformability of human red blood cells harboring Plasmodium falciparum*, P.N.A.S **104**, 9213 (2007). 18

[55] Mills, J., L. Qie, M. Dao, K. Tan, C. Lim, and S. Suresh, *Continuous force-displacement relationships for the human red blood cell at different erythrocytic developmental stages of Plasmodium falciparum malaria parasite*, in *MRS Proceedings* (Cambridge Univ Press, ADDRESS, 2004), Vol. 844, pp. Y7–8. 17, 18

[56] Mohandas, N. and E. Evans, *Mechanical properties of the red cell membrane in relation to molecular structure and genetic defects*, Annu. Rev. Biophys. Biomol. Struct. **23**, 787 (1994). 15, 16

[57] Oradd, G., G. Wikander, G. Lindblom, and B. Johansson, *Effect of glycerol on the translational and rotational motions in lipid bilayers studied by pulsed-field gradient 1H NMR, EPR and time-resolved fluorescence spectroscopy*, J. Chem. Soc. Faraday Trans. **90**, 305 (1994). 13

[58] Palmer, A. and J. Martin, *Buckle propagation in submarine pipelines*, Nature **254**, 46 (1975). 61

[59] Popescu, G., T. Ikeda, K. Goda, C. A. Best-Popescu, M. L. Laposata, S. Manley, R. R. Dasari, K. Badizadegan, , and M. S. Feld, *Optical measurement of cell membrane tension*, Phys. Rev. Lett. **97**, 218101 (2006). 12

[60] Prinz, V., V. Seleznev, A. Gutakovsky, A. Chehovskiy, V. Preobrazhenskii, M. Putyato, and T. Gavrilova, *Free-standing and overgrown InGaAs/GaAs nanotubes, nanohelices and their arrays*, Physica E **6**, 828 (2000). 71

[61] Raux, P., P. Reis, J. Bush, and C. Clanet, *Rolling ribbons*, Phys. Rev. Lett. **105**, 044301 (2010). 62

[62] Reyssat, E. and L. Mahadevan, *Hygromorphs: from pine cones to biomimetic bilayers*, J. Roy. Soc. Interface **6**, 951 (2009). 2

[63] Reyssat, E. and L. Mahadevan, *How wet paper curls*, Euro. Phys. Lett. **93**, 54001 (2011). 2, 3, 4

[64] Salmon, B., A. Oksman, and D. Goldberg, *Malaria parasite exit from the host erythrocyte: a two-step process requiring extraerythrocytic proteolysis*, Proc. Natl. Acad. Sci. USA **98**, 271 (2001). 17

[65] Sandre, O., L. Moreaux, and F. Brochard-Wyart, *Dynamics of transient pores in stretched vesicles*, Proc. Natl. Acad. Sci. USA **96**, 10591 (1999). 12, 19

[66] Seffen, K. and S. Pellegrino, *Deployment dynamics of tape springs*, Proc. R. Soc. Lond. A **455**, 1003 (1999). 48, 50, 61

[67] Seifert, U., *Configurations of fluid membranes and vesicles*, Adv. Phys. **46**, 13 (1997). 13, 14

[68] Siegel, D. P., *Determining the ratio of the Gaussian curvature and bending elastic moduli of phospholipids from Q(II) phase unit cell dimensions*, Biophys. J. **91**, 608–618 (2006). 16

[69] Siegel, D. P., *The Gaussian Curvature Elastic Energy of Intermediates in Membrane Fusion*, Biophys. J. **95**, 5200–5215 (2008). 16

[70] Siegel, D. P. and M. M. Kozlov, *The Gaussian curvature elastic modulus of N-monomethylated dioleoylphosphatidylethanolamine: Relevance to membrane fusion and lipid phase behavior*, Biophys. J. **87**, 366 (2004). 16

[71] Songmuang, R., C. Deneke, and O. Schmidt, *Rolled-up micro-and nanotubes from single-material thin films*, App. Phys. Lett. **89**, 223109 (2006). 2, 3

[72] Strogatz, S., *Nonlinear dynamics and chaos: with applications to physics, biology, chemistry and engineering*, (2001). 34

[73] Strogatz, S. H., *Nonlinear dynamics and chaos* (Perseus Books, Cambridge, 1885). 69

[74] Struik, D., *Lectures on classical differential geometry* (Dover, ADDRESS, 1961). 14, 19, 40

[75] Svetina, S. and B. Žekš, . 85

[76] Tadrist, L., F. Brochard-Wyart, and D. Cuvelier, *Bilayer curling and winding in a viscous fluid*, Soft Matter **8**, 8517 (2012). 76

[77] Umeda, T., Y. Suezaki, K. Takiguchi, and H. Hotani, *Theoretical analysis of opening-up vesicles with single and two holes*, Phys. Rev. E **71**, 011913 (2005). 29

[78] Verberg, R., I. DeSchepper, and E. Cohen, *Viscosity of colloidal suspensions*, Phys. Rev. E **55**, 3143 (1997). 32

[79] Vermorel, R., N. Vandenberghe, and E. Villermaux, *Radial cracks in perforated thin sheets*, Phys. Rev. Lett. **104**, 175502 (2010). 71

[80] Veysey, J. and N. Goldenfeld, *Simple viscous flows: From boundary layers to the renormalization group*, Rev. Mod. Phys. **79**, 883 (2007). 45, 67, 68

[81] Viamontes, G. and D. Kirk, *Cell-shape changes and mechanism of inversion in volvox*, J. Cell Biol. **75**, 719 (1977). 3

[82] White, F., *Fluid mechanics, 1979* (McGraw Hill, ADDRESS, YEAR). 45

[83] Williamson, C. and R. Govardhan, *Vortex-induced vibrations*, Annu. Rev. Fluid Mech. **36**, 413 (2004). 68

[84] Witten, T. and H. Li, *Asymptotic shape of a fullerene ball*, Europhys **Lett 23**, 51 (1993). 51

**Résumé :**

La déformation de matériaux élastiques dont l'une au moins des dimensions est petite apparaît dans un grand nombre de structures naturelles ou artificielles pour lesquelles une courbure spontanée est présente. Dans ces travaux de thèse, nous couplons plusieurs approches théoriques à des expériences macroscopiques sur des rubans élastiques afin de comprendre la dynamique d'enroulement de biomembranes ouvertes d'un trou. La motivation est issue d'observations récentes d'enroulements obtenues au cours de la sortie de parasites de la Malaria de globules rouges infectés (MIRBCs), et de l'explosion de polymersomes.

Dans une première partie, nous étudions théoriquement la stabilité d'un pore et la propagation de l'enroulement sur une biomembrane sphérique ouverte. Nous modélisons de façon géométrique l'enroulement toroïdal de la membrane par une spirale d'Archimède de révolution et décentrée. Avec cette hypothèse, nous montrons que la stabilité du pore vis-à-vis de l'enroulement dépend fortement de la tension de ligne et du cisaillement et nous discutons ces résultats dans le cadre de l'enroulement de membranes MIRBCs. De plus, en prenant en compte les différentes sources de dissipation, nous obtenons un très bon accord entre les données expérimentales obtenues pour les MIRBCs et la dynamique d'enroulement obtenue par le calcul. Notre approche montre en particulier que la dissipation dans la membrane due à la redistribution de la matière durant l'enroulement domine sur la dissipation visqueuse dans le milieu.

Cependant, la complexité de la géométrie sphérique, ainsi que le nombre limité d'observations microscopiques à l'échelle de la membrane sont une entrave au développement de modèles plus détaillés qui permettraient de décrire complètement le couplage entre écoulement et déformation. Nous avons donc étudié dans une seconde partie la déformation d'enroulement dans le cas de rubans élastiques ayant une courbure spontanée dans différents milieux visqueux et pour différentes conditions élastiques. A grands nombres de Reynolds, en raison de la localisation de la courbure pour les rubans au cours de la propagation du front d'enroulement le long du matériau, nous montrons que l'enroulement atteint rapidement une vitesse de propagation constante. Dans ce régime, le ruban s'enroule sur lui-même de façon compacte, sur un cylindre dont la taille est prévue à partir d'une solution d'onde solitaire pour l'Elastica. A faible nombre de Reynolds, cependant, se rapprochant des conditions d'enroulement d'une membrane microscopique, nous mettons en évidence l'influence des forces de lubrification sur la nature non-compacte de l'enroulement. La taille globale de la spirale de ruban augmente dans le temps conduisant à une diminution de la puissance élastique libérée et donc à une diminution de la vitesse. Nous discutons dans quelle mesure ces résultats peuvent faire avancer la modélisation de l'enroulement dans les MIRBCs et les polymersomes.

*Mots clés : enroulement, ruban, membrane, paludisme, courbure spontanée.*

---

**Abstract :**

Curling deformation of thin elastic surfaces appears in numerous natural and man-made structures where a spontaneous curvature is present. In this thesis, we couple theoretical approaches and macroscopic experiments on elastic ribbons to decipher the dynamics of curling associated to opened bio-membranes, motivated by recent microscopic observations of curling in membranes of Malaria infected red blood cells (MIRBC) and artificial polymersomes.

In a first part, we study theoretically pore opening and curling destabilization due to the presence of a uniform spontaneous curvature in a bio-membrane. We model axisymmetric curling with the revolution of a decentered Archimedean spiral leading to prescribed toroidal-like wrapping of the membrane. In this configuration, we show that the stability of an open pore depends strongly on both line-tension and shear elasticity. Moreover, because of the spherical geometry of the problem, we demonstrate that the inner dissipation resulting from the surface redistribution, dominates the dynamics over the outer fluid viscous dissipation, in quantitative agreement with experimental data obtained on MIRBC.

Subsequently, due to the lack of clear experimental images of microscopic curling, and the complexity of the spherical topology, we study in a second part the curling of macroscopic naturally curved elastic ribbons. In order to separate the respective roles of flow, elasticity and geometry, the experiments are performed in different viscous media and elastic conditions. We show that, because of the tendency of ribbons to localize bending deformations, when a curling front at high Reynolds numbers travels down the material, it reaches a constant velocity rapidly. In this regime, the ribbon wraps itself into a compact roll whose size is predicted through the solitary wave solution of the associated elastica. At low Reynolds numbers, however, due to strong lubrication forces, curling is no more compact. The overall size of the spiraling ribbon increases in time with a power law and leading to a temporal decrease of elastic power and to a consequent decrease in velocity. We discuss how such discovery sheds a new light on the modeling of curling in MIRBCs and polymersomes.

*Key words : curling, ribbon, membrane, malaria, spontaneous curvature.*